UNIVERSITY OF CALIFORNIA SAN DIEGO

Modeling of Neurons and Neural Networks in HVC of Zebra Finches

A dissertation submitted in partial satisfaction of the
requirements for the degree Doctor of Philosophy

in

Physics

by

Pan Xia

Committee in charge:

Professor Oleg Shpyrko, Chair
Professor Johnatan Aljadeff
Professor Michael Fogler
Professor Nigel Goldenfeld
Professor Elena Koslover

2023

The Dissertation of Pan Xia is approved, and it is acceptable in quality and form for publication on microfilm and electronically.

University of California San Diego

2023

DEDICATION

To my parents and my husband

TABLE OF CONTENTS

LIST OF FIGURES

LIST OF TABLES

ACKNOWLEDGEMENTS

First, I want to express my deepest gratitude to my advisor, Professor Henry Abarbanel, who has always been a role model and a brilliant mentor to me. His dedication and his wide knowledge in mathematics and physics keep inspiring me. Also, I would like to thank him for accepting me in my fourth year. His kindness and patience show me what an exceptional mentor is. Henry suddenly passed away before I finished this dissertation, but most work presented here was carried out under his guidance.

I am also very thankful to Prof. Elena Koslover and Prof. Nigel Goldenfeld, who offers tremendous guidance and feedback to my research and writing after Henry passed away. They generously offered to help me when I was lost without my advisor. I also would like to thank Prof. Michael Fogler and Prof. Johnatan Aljadeff for graciously agreeing to join my committee, and Prof Oleg Shpyrko, chair of the physics department, to serve as my new committee chair.

I am privileged to work with many brilliant people during my PhD in UCSD. Especially, I would like to acknowledge the suggestions and help from Dr. Fang Zheng, Prof. Richard Daniel Mooney and Prof. Arij Daou. I would also like to thank Dr. Jason Platt, Dr. Anna Miller, Mr. Dawei Li, Dr. Randall Clark, Mr. Lawson Fuller and Dr. Adrian Wong for being fantastic colleagues. Especially, Dr. Randall Clark, another PhD student from Henry's group, provided the current data used in Chapter 2.

I would like to thank Ms. Sharmila Poddar and Prof. Patrick H. Diamond for their support.

Finally, I want to express dedication to my parents, my husband and my two kittens for their unconditional support.

Chapter 3, in full, is currently being prepared for submission for publication of the material by P. Xia and H. D. I. Abarbanel. The dissertation author is the primary author of this paper.

VITA

2016 Bachelor of Science, University of Science and Technology of China

2023 Doctor of Philosophy, University of California San Diego

ABSTRACT OF THE DISSERTATION

Modeling of Neurons and Neural Networks in HVC of Zebra Finches

by

Pan Xia

Doctor of Philosophy in Physics

University of California San Diego, 2023

Professor Oleg Shpyrko, Chair

Vocalizations are an essential medium for sexual signaling in zebra finches. Male zebra finches produce highly stereotyped complex sequences of vocal gestures during courtship. The acquisition and production of their songs occur through the song system which consists of a series of forebrain nuclei. The telencephalic sensorimotor nucleus known as HVC plays a central role in this complex system by controlling the temporal structure of birdsong and the order of syllables. We combine physical and mathematical approaches to explore how HVC neurons form activities that contribute to the downstream song production pathway, and leverage electrophysiology and imaging data from this nucleus to develop single neuron and neuron network models and verify their performance.

In Chapter 2, we explore a data assimilation method to transfer electrophysiology observations to HVC neuron models. We employ conductance-based models of single HVC neurons describing experimentally-verified ion currents, and estimate the time-invariant parameter values and dynamics of model variables with data assimilation. The effectiveness of the method is tested by accuracy of estimations of unknown variables and prediction of future neuron voltage under a different stimulus during numerical simulations.

Synaptical interactions among various types of HVC neurons are essential for this nucleus to function normally, so Chapter 3 proposes a neuron network model containing two major types of neurons in the HVC. The model is based on recordings of individual neurons' membrane potentials and experimentally observed synaptical currents. Model predictions are supported by multiple observations of behavior of the two types of neurons, especially their firing patterns during birdsong.

This dissertation explores dynamics and functions of neurons in HVC via modeling and inference approaches rooted in physics principles.

Chapter 1

Introduction

Theoretical neuroscience is an important branch of neuroscience which uses models to characterize what nervous systems do, to determine how they function, and to understand the logic of their operations [1] [2]. It employs the methods of mathematics, physics, chemistry, biology and computer science to provide insights into neuron system functions. These methods in neuroscience have a long tradition dating back to early mathematical theories of perception and of current integration across a neuron's membrane [3] [4]. This dissertation aims to capture the essential features of neurons and their interactions with theoretical models that transfer experimental measurements to dynamical evolutions of neuron states.

Studying of the human brain is one of the most attractive topics in neuroscience, but our understanding of the neural basis of humans is limited by the complexity of this central nervous system and current techniques. The techniques for recording neural activities in the human brain is very limited compared to what are used in animals, especially thanks to the availability of invasive methods in animals [5]. Therefore, to gain insight into human neuronal circuits, neuroscientists conduct experiments and modeling on animals' neuron activities which exhibit human analogues. Vocal communication has fundamental importance to human behavior and interactions, but the underlying neural mechanisms remain a mystery. Fortunately, the brain and behavior of songbirds have provided an excellent model of human language learning and production [5] [17]. The complex form of vocal learning and generation for birdsong bears strong

parallels to human speech [16], and recent experimental advancements have led to delineation of neural circuits behind song productions, especially for zebra finches.

1.1 HVC in the song system

Many birds including male zebra finches (*Taeniopygia guttata*) can produce songs, a specific type of vocalization. The major difference between songs and other kinds of vocalizations is that the songs are accompanied by specific body postures, and they are a learned behavior [14]. For example, male zebra finches copy similar songs from their father. After the songs' acoustic structures are crystallized (i.e. stereotyped and much less dependent on auditory feedback), these birds do not change their singing even if they are deaf afterward [14]. Certain finches including the zebra finches sing primarily to attract and retain a mate. Male zebra finches' songs may increase their reproductive success by increasing female birds' receptivity [14].

Neuroscientists have identified a specialized neural circuit controlling singing and song learning which is different from the brains from non-singing birds [16] [34] [19]. This integrated forebrain and brain stem circuit is the song system, and it controls vocalization through the avian syrinx and the muscles of respiration [16].

Vocalizations in songbirds and humans share some major similarities. They have the same basic organizational features in the auditory periphery; birdsong and speech share similar precisely integrated vocal and respiratory muscle activities; both vocal learnings depend on early auditory experience and feedback [16]. Thus, the study and modeling of bird's song system will be very helpful to understand the mechanism of human audition and speech.

The song system receives input from the telencephalic song nucleus HVC (used as a proper name), an important region of the song production system. This system is distributed across the entire brain, both conveying descending auditory muscle signals and receiving up-stream auditory, proprioceptive and recurrent motor information. However, experiments still support the view that HVC sits at the top of this complex system anatomically and functionally

[16].

There are two major pathways in the song system: song motor pathway (SMP) and anterior forebrain pathway (AFP), and they both arise from projecting neurons (PN) in HVC (see Figure 1.1). There are two types of PN in HVC: HVC_{RA} and HVC_X. HVC_{RA} neurons give rise to the song motor pathway, and they project to the nucleus of the arcopallium(RA), which projects down into the syringeal motor neurons and respiratory premotor neurons in the brain stem [16]. On the other hand, the anterior forebrain pathway arises from HVC_X neurons which innervate area X, which in turn makes inhibitory connections to neurons in the dorsolateral thalamus (DLM). Next, excitatory synapses from DLM connect with the lateral portion of the magnocellular nucleus of the anterior nidopallium (LMAN), which innervates both area X and forms fast excitatory synapses in the song premotor neurons in RA [16].

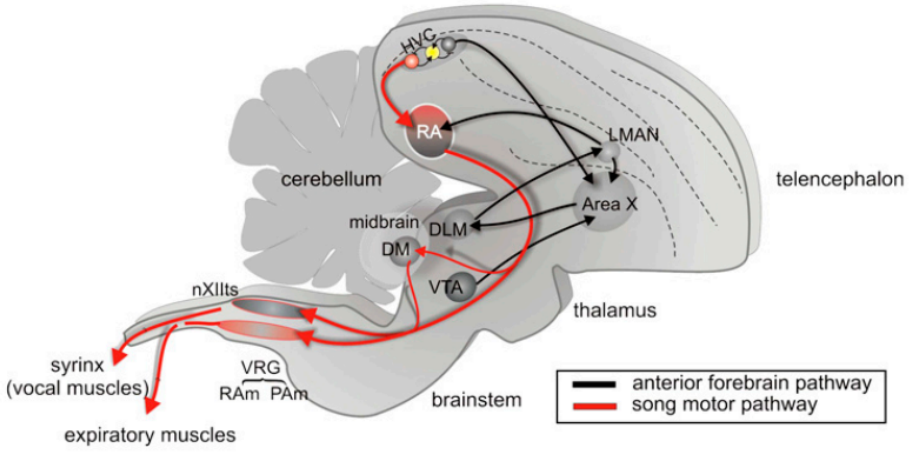

Figure 1.1. The song system in zebra finches. HVC sits at the top location in the song system. The HVC_{RA} neuron projects to RA and the HVC_X projects to area X. Reproduced from [16]

In addition to the fact that HVC sits at the pivotal location in the sensorimotor network, experiments clearly show that HVC neurons play a critical role in singing and song learning: lesions of HVC neurons have a destructive effect on singing behavior, and electrodes in the

HVC detect activities synchronized with individual syllables even in deafened birds [16]. This evidence motivates great interest in understanding and modeling the activity of HVC neurons during singing and vocal learning.

To study how HVC neurons encode song sequence and phonology, one approach is to characterize the cellular properties of each single neuron by transferring observed neuron dynamics to the underlying neuron models, which is the major goal of Chapter 2. Moreover, the synaptic transmission in HVC is extensive and has important behavior consequences [46]; thus, Chapter 3 connects different types of HVC neurons together with experimentally identified synaptic interactions to form a model of the HVC microcircuit.

1.2 Outline of the dissertation

We set the scope of this dissertation in this chapter. First, we present the importance of understanding the song system in zebra finches and the reason to focus on studying the HVC nucleus. Then we preview the motivations for the main part of this dissertation, Chapter 2 and Chapter 3. Now, we follow up with the outline of these two chapters. Chapter 4 is a review of important conclusions in the previous chapters.

The goal of Chapter 2 is to calibrate single neuron models to match electrophysiological recordings efficiently. Transferring information from lab data to theoretical models has always been a crucial problem to many science and engineering disciplines. In most cases, the experimental data from neurons is noisy and incomplete because of the limitation of available measurements, equipment and possible input from other neurons [6]. To describe the behavior of a single neuron, there will be many state variables related to the neuron (see Section 2.2 for details), while the current technique can only gather noisy voltage information through an electrode [6] [12]. For the theoretical model, we employ a set of dynamical equations that control the evolution of the neuron membrane potential. These dynamical equations are a generalized and simplified model of the real neuron under some basic assumptions, so that the time evolution

process of state variables is not too complicated to calculate. However, the time-independent parameters of the model may be different from neuron to neuron, and they need to be determined based on the neuron responses to input signals [28]. To complete the model and estimate the unknown state variables with observed membrane potential and applied external signal, we adopt a data assimilation method, Precision Annealing Hamilton Monte Carlo (PAHMC) published by Zheng et al. [9]. Chapter 2 uses this method to transfer voltage and external signal data into several models of single HVC neurons in numerical simulations, and predicts the neuron voltage forward in time based on the completed model.

Single neuron models are not sufficient to characterize the cellular mechanism in HVC responsible for zebra finches singing behavior. Therefore, Chapter 3 proposes a neural circuit model mediating the song production. Numerous *in vivo* and *in vitro* recordings of both single HVC neurons and their synaptic connections have been carried out [36] [28] [46] [14] [15]. These studies shed light on HVC neuron activity during both vocalizations and silence, responses of different types of HVC neurons to injected currents, ion channels that exist on the cell membrane, and local synaptic interactions between identified HVC neuron pairs. Further experiments have also revealed synaptic connections from other parts of the brain to the HVC region which enable the beginning of song production. In Chapter 3, we start from single neuron models for two types of HVC neurons, their synaptic current models, as well as a model of trigger current from another part of the brain. All the models are supported by experimental recordings with minimal modifications of parameter values. Then we will show that the constructed neural circuit model reproduces salient behavior patterns of the two types of HVC neurons, both during the silent time of zebra finches or when the male is singing to attract a female.

The overall goal of this dissertation is to build a comprehensive picture of HVC neurons and their interactions to understand the dynamics and functions of this important nucleus in the song system. Using cross-discipline techniques across physics and neuroscience, we have explored key inference tools to connect cellular dynamics with biological functions and key features of intercellular activities, providing a stepping stone towards the study of human speech

and its underlying neural mechanisms.

Chapter 2

Data assimilation on HVC neurons

2.1 Introduction

Understanding the properties of a single neuron has always been an interesting and fundamental problem in biophysics. Neurons are the basic working unit in the brain, but there is still no satisfactory way to measure all their interesting properties [22] [20]. Usually, the most accurate recording available is the membrane voltage inevitably accompanied by noise. Our goal is to use data assimilation methods to extract information from limited measurements. The information we are interested in extracting includes ion channel properties and dynamics, which enable the prediction of neuron voltages under new stimuli.

2.1.1 Dynamics of a single neuron

We start with an introduction of the electrophysiology properties of an isolated neuron and model the neuron as a dynamic system with multiple variables describing the system states and a set of time-independent parameters. A simple conductance-based model treats a neuron as a dimensionless point, surrounded by its semi-permeable membrane [12]. The difference between the inside potential and the outside potential separated by the membrane is referred to as the membrane potential. This potential difference arises from the difference between intracellular and extracellular concentrations of various charged ions such as sodium, potassium and chloride [12] [13].

The cell membrane consists of the lipid bilayer, which is not permeable to ions flows. All ions can only travel across the membrane through specific ion channels formed by proteins (see Figure 2.1). The ion channels can be divided into two categories: gated channels which have both open and closed states, and nongated channels which are always open [13]. For the gated channels, their transitions between open and closed states are often determined by the membrane potential (i.e., " voltage-gated channels"), but other variables may also affect gating states. The fraction of open gates for a specific type of neuron is referred to as the gating variable, an important state variable describing cross-membrane current dynamics. The membrane potential depends on the injected current applied to the neuron and all the ion currents, and therefore the gating variables. Conversely, the dynamics of gating variables can be determined by the voltage [12].

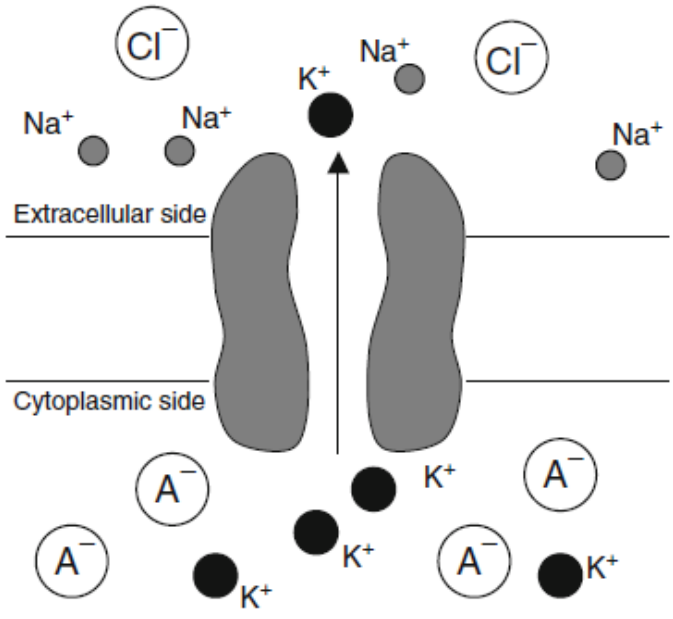

Figure 2.1. Potassium ions move across the membrane through the gated channel formed by proteins. The gated channels are mostly selective for a specific type of ions. Reproduced from [13].

In summary, the dynamics of a single neuron can be described by a group of time-dependent variables: cross-membrane voltage, stimulus current, and gating variables for various

types of gated ion channels. Typically, the only information available from experiments is the membrane potential and the input current. In certain experimental setups, it is possible to inject designated input currents to a neuron through an electrode, and then record the voltage response of the neuron [46] [36]. Due to the limitations of electronic equipment, the current and voltage data may contain small white noise [6]. The goal of this chapter is to estimate unmeasurable state variables (i.e. all gating variables), fit parameters of a single neuron model and predict neuron behavior under arbitrary stimulus current for HVC neurons in zebra finches. To accomplish this task, we will introduce a model that characterizes important ion channels in a single neuron in Section 2.2, and we will eventually use this dynamical system as a basis to predict the time evolution of state variables (i.e. membrane potential and gating variables) in the neuron.

2.1.2 Mathematical form of data assimilation

Data assimilation refers to the information transfer process from data to physical dynamical models [6] [7] [8]. In our case, we want to use data assimilation to transfer neuron voltage information to a dynamical model describing ion channels and the voltage response to outside stimulus. Most data assimilation problems can be expressed in the form of a set of first-order differential equations with respect to time, The most popular form can be generalized as:

$$\frac{dx_a(t)}{dt} = F_a(\boldsymbol{x}(t), \boldsymbol{\theta}), a = 1, 2, ..., D \tag{2.1}$$

where $\boldsymbol{x}(t)$ is a D-dimensional state variable changing with time. F_a represents the dynamical equation which determines the evolution in time for a-th state variable $x_a(t)$. $\boldsymbol{\theta}$ is a set of time-independent parameters which need to be fit to data in most cases.

In most experiments, only a sparse set of the entire state variable space $\boldsymbol{x}(t)$ is recorded. The observed data set is denoted by $\boldsymbol{y}(t_n)$, which is an L-dimensional variable measured at discrete times $t_n = [t_0, t_1, ..., t_f]$. Typically, the measured set is much smaller than $\boldsymbol{x}(t)$, so $L \ll D$ and t_n is also sparse in time. In addition to estimating the model parameters $\boldsymbol{\theta}$, another task of

data assimilation is to evaluate the values of those missing state variables [8] [7].

Eq 2.1 can be discretized by evaluating it at times $t_n = [t_0, t_1, ..., t_f]$. The new time evolution equation becomes:

$$x_a(n+1) = f_a(\boldsymbol{x}(n), \boldsymbol{\theta}), a = 1, 2, ..., D \tag{2.2}$$

where $x_a(n+1)$ is a simplified notation of $x_a(t_n+1)$. Usually, the one-step mapping function f_a does not depend on time, as long as the discretized time step is uniform and all time dependent variables are included in $\boldsymbol{x}(n)$.

Now, the explicit task of data assimilation is to use the measurements in the time window $[t_0, ..., t_f]$ to estimate N_p time-independent parameters $\boldsymbol{\theta} = [\theta_0, \theta_1, ..., \theta_{N_p}]$ and all unknown state variables $[x_{L+1}, x_{L+2}, ..., x_D]$. The estimated model can also be used to predict new observations $\boldsymbol{y}(t > t_f)$.

For a noisy measurement up to time t_n, we have a collection of data $\boldsymbol{Y}(n)$ = [$\boldsymbol{y}(\tau_0)$, $\boldsymbol{y}(\tau_1)$, ..., $\boldsymbol{y}(\tau_F)$] and an estimation of the parameters and state variables up to time t_m: $\boldsymbol{X}(m)$ = [$\boldsymbol{x}(t_0)$, $\boldsymbol{x}(t_1)$, ..., $\boldsymbol{x}(t_m)$, $\boldsymbol{\theta}$]. The time steps of observations $\boldsymbol{Y}(n)$ can be sparser than that in $\boldsymbol{X}(m)$. The goal of assimilation of information is to maximize the conditional distribution of states $P(\boldsymbol{X}(m)|\boldsymbol{Y}(n))$.

The most relevant output is not the value of $P(\boldsymbol{X}(m)|\boldsymbol{Y}(n))$, but the conditional expected value of a function $G(\boldsymbol{X}) \equiv G(\boldsymbol{X}(m))$. This function is used to find the conditional expectation values of quantities of physical or biological interest, even though most of the problems only focus on $G(\boldsymbol{X}) = \boldsymbol{X}$. $G(\boldsymbol{X})$ can be any functions of the path $\boldsymbol{X}(m) = [\boldsymbol{x}(t_0), \boldsymbol{x}(t_1), ..., \boldsymbol{x}(t_m), \boldsymbol{\theta}]$. The expected value of $G(\boldsymbol{X})$ can be expressed with respect to the conditional probability distribution $P(\boldsymbol{X}|\boldsymbol{Y})$:

$$< G(\boldsymbol{X}) >= E[G(\boldsymbol{X})|Y] = \frac{\int d\boldsymbol{X} G(\boldsymbol{X}) P(\boldsymbol{X}|\boldsymbol{Y})}{\int d\boldsymbol{X} P(\boldsymbol{X}|\boldsymbol{Y})} \tag{2.3}$$

where $d\boldsymbol{X} = \prod_{m=0}^{M} d^D\boldsymbol{x}(m) \prod_{j=1}^{N_p} d\theta_j$ is the path space. To solve for this expected value of $G(\boldsymbol{X})$,

the formulation of $P(\boldsymbol{X}|\boldsymbol{Y})$ must be derived first. For this purpose, we need to know the transition probability $P(\boldsymbol{x}(n)|\boldsymbol{x}(n-1))$ from time step t_{n-1} to t_n together with the transition probability from the state variable $\boldsymbol{x}(n)$ to the collected data $\boldsymbol{y}(n)$. The general assumption is that the mapping process from t_{n-1} to t_n is a Markov process as the conditional probability $P(\boldsymbol{x}(n)|\boldsymbol{x}(n-1))$ only depends on $\boldsymbol{x}(n-1))$ rather than any states before it. If the model from Eq (2.2) has no error, $P(\boldsymbol{x}(n)|\boldsymbol{x}(n-1))$ can be reduced to a delta function. However, the model typically exhibits an error ε, then Eq (2.2) will be:

$$x_a(n+1) = f_a(\boldsymbol{x}(n), \boldsymbol{\theta}) + \varepsilon \tag{2.4}$$

The transition probability from $\boldsymbol{x}(n)$ to $\boldsymbol{y}(n)$ can also be assumed to be a Markov process, and there is always a measurement error in the model η [6] [7]:

$$\boldsymbol{y}(n) = \boldsymbol{x}(n) + \eta \tag{2.5}$$

The two error terms ε and η may come from measurement noise and errors in the model such as incomplete description of the dynamical system. After applying the Markovian properties and the Bayesian law, the conditional probability can be written as:

$$P(\boldsymbol{X}|\boldsymbol{Y}) \propto [\prod_{k=0}^{F} P(\boldsymbol{y}(k)|\boldsymbol{x}(k))] \times [\prod_{m=1}^{M} P(x(m)|x(m-1))] \times P(x(0)) \tag{2.6}$$

where $k = 0, 1, ..., F$ denotes the observation time steps, and $m = 1, ..., M$ represents the time stamps at which the D-dimensional state variable $\boldsymbol{x}(m) = \boldsymbol{f}(\boldsymbol{x}(m-1), \boldsymbol{\theta})$ is used to move forward in time.

2.1.3 Action minimization

The action is defined as the negative log-likelihood of $P(\boldsymbol{X}|\boldsymbol{Y})$ with an unimportant normalizing constant C:

$$A(\boldsymbol{X}) = -\log[P(\boldsymbol{X}|\boldsymbol{Y})] - \log C \tag{2.7}$$

The action includes all the information about the observations and estimation of the state variables. Combing the definition of action in Eq (2.7) and the expected value expression of $G(\boldsymbol{X})$ from Eq (2.3), the probability distribution can be expressed as:

$$< G(\boldsymbol{X}) >= \frac{\int d\boldsymbol{X} G(\boldsymbol{X}) e^{-A(\boldsymbol{X})}}{\int d\boldsymbol{X} e^{-A(\boldsymbol{X})}} \tag{2.8}$$

where the constant part of $e^{-A(\boldsymbol{X})}$ in the numerator and denominator cancels each other. Eq.(2.8) does not have an analytical solution for most problems, so it is important to find an accurate and efficient numerical method to evaluate it [6] [7]. Starting from the definition of action and Eq (2.6), it is straightforward to show that:

$$A(\boldsymbol{X}) = -\sum_{k=0}^{F} \log[P(\boldsymbol{y}(k)|\boldsymbol{x}(k))] - \sum_{m=1}^{M} \log[P(x(m)|x(m-1))] - \log[P(x(0))] \tag{2.9}$$

The first term represents the information from each observation $\boldsymbol{y}(k)$, which is called measurement error. $k = 0, 1, ..., F$ denotes the observation time steps. The second part means the stochastic evolution of the state variable from time t_{m-1} to t_m where $m = 1, ..., M$ and we name it as model error [6] [7]. The last term is the initially estimated distribution of the state variable. To further simplify the action, we can make two other assumptions:

- In most cases, there is no measurement available about $P(x(0))$, so it is usually assumed to be uniform over the dynamical range of the model parameters and state variables [6] [7]. Therefore, $P(x(0))$ in the numerator and denominator cancels out in Eq.(2.8).

- The measurement error between $\boldsymbol{y}(k)$ and $\boldsymbol{x}(k)$ is assumed to follow a Gaussian distribution with zero mean and a diagonal precision matrix $R_m(l,t)\delta_{lk}$. Similarly, the model error

between $x(m)$ and $x(m-1)$ is also the same distribution with a different matrix $R_f(a,b)\delta_{ab}$.

With these assumptions, the action in discrete time steps can finally be written as:

$$A(\boldsymbol{X}) = \sum_{k=0}^{F}\sum_{l=1}^{L}\frac{R_m(l)}{2(F+1)}[x_l(k)-y_l(k)]^2 + \sum_{m=0}^{M-1}\sum_{a=1}^{D}\frac{R_f(a)}{2M}[x_a(m+1)-f_a(x(m),\boldsymbol{\theta})]^2 \quad (2.10)$$

Why is the action so important for data assimilation? Our ultimate goal is to evaluate the expected value of $G(\boldsymbol{X})$ from Eq (2.8). It is apparent that the dominant part of $< G(\boldsymbol{X}) >$ comes from where the action reaches its minimum in the path space. It is almost impossible to find it analytically. Thus, we need to develop some numerical methods to minimize the action.

2.1.4 Data assimilation method

Section 2.4 will transfer information from voltage and stimulus data into the dynamical model of neuron with Precision Annealing Hamiltonian Monte Carlo (PAHMC), a new data assimilation method established in 2020 by Zheng et al.[9]. Their work proposed a systematic way of efficiently sampling from the distribution $\pi(\mathbf{X}|\mathbf{Y}) \propto \exp[-A(\mathbf{X})]$ and locating the minimum of the action $A(\mathbf{X})$ in the path space (a path consists of all state variables and parameters). PAHMC samples in the high-dimensional space of state variables and time-independent model parameters with Hamiltonian Monte Carlo (HMC), and uses Precision Annealing (PA) to start the sample procedure near the global minimum and remain there [6]. Section 2.4 will present the results on estimating gating variables of neurons, finding unknown model parameters and predicting the voltage forward in time with this data assimilation method.

HMC was introduced as an innovative version of Monte Carlo sampling for high-dimensional probability distributions from the 1980s [10] [11]. The core idea is to achieve high efficiency by introducing additional degrees of freedom into the target distribution and avoid the random-walk behavior which has lower acceptance rates of proposed moves in path space as well as a markedly slower exploration of the target distribution $\pi(\mathbf{X}|\mathbf{Y})$ [9].

HMC proceeds by making proposals according to Hamilton's equations for the model state variables $\mathbf{X}$ and their canonical conjugates $\mathbf{P}$. The HMC samplings occur in the enlarged canonical phase space $(\mathbf{X},\mathbf{P})$ instead of the original space $\mathbf{X}$. Thus, the target distribution becomes $\pi(\mathbf{X},\mathbf{P}) \propto \exp[-H(\mathbf{X},\mathbf{P})]$ with $H(\mathbf{X},\mathbf{P}) = A(\mathbf{X}) + \frac{\mathbf{P}^2}{2}$. Because of the invariance properties of Hamiltonian dynamics, if the proposed moves from time 0 to s are made using integration of the following equation:

$$\frac{d}{ds}\begin{pmatrix}\mathbf{X}(s)\\ \mathbf{P}(s)\end{pmatrix} = \begin{pmatrix}\mathbf{P}(s)\\ -\nabla A(\mathbf{X}(s))\end{pmatrix} \tag{2.11}$$

then $H(\mathbf{X},\mathbf{P})$ is almost conserved when the integration is solved numerically. Thus, the overall acceptance rate is close, but not equal, to unity. This high acceptance rate ensures a more efficient exploration in the path space than traditional Monte Carlo [9].

For a non-convex, high-dimensional action $A(\mathbf{X})$, HMC itself does not guarantee to capture the maximum of the target distribution without a prior knowledge to find the minima in the action. In fact, for a random initialization in the path space, it is unlikely for an HMC sampler to travel for a long distance [9].

To address this issue and locate the global minimum in the action, precision annealing (PA) is implanted in the HMC procedure. It drives the sampling area to the neighborhood of the minimum in the cost function by gradually increasing the model precision parameter R_f. PA arises from the idea that if an initial path for a Monte Carlo method is chosen at the global minimum for small R_f, the sampling will stay in a region of the path space where the Monte Carlo search will arrive at the smallest minimum of the action. When R_f is zero, the path space is highly degenerated for the unobserved degrees of freedom, and the action apparently has its degenerate global minimum at $x_l(k) = y_l(k)$ for $k = 0,1,...,F$ and $l = 1,...,L$. As one increases R_f, HMC sampling begins at a position in the path space that is well-informed by the samples within previous R_f values. This enables the locating of the global minimum in $A(\mathbf{X})$ to be more

and more precise as R_f becomes larger. The following procedure is adopted during the increment of R_f:

$$R_f^a = R_{f0}^a \cdot \alpha^\beta \quad (\beta = 0, 1, ..., \beta_{\max}) \tag{2.12}$$

with a choice of small R_{f0} and $\alpha > 1$, the value of R_f will slowly increase as β increases from 0 to $\beta_{\max}$. This precision annealing method is similar in spirit to simulated annealing [24].

2.2 Single neuron model

2.2.1 The Hodgkin-Huxley model

The Hodgkin-Huxley model is a classical model of a single neuron established by Alan Hodgkin and Andrew Huxley in 1952 [20]. It provides a comprehensive and quantitative description of the three basic ion currents: sodium (Na), potassium (K), and the leak (L) current, which are collectively referred to as the NaKL model. The leak channel represents all the non-gated ion channels. These channels are always open and allow specific ions to freely diffuse [21] [8]. The NaKL channels form the most basic structures of a functional neuron [20], like the hydrogen atom is the most basic atom in physics. We will start with the NaKL model, and discuss the dynamics of some other ion currents in Section 2.2.2 and 2.2.3.

The Hodgkin-Huxley model approximates a single neuron as a nonlinear oscillator with feedback loops among the ion flows across the membrane and ignores the thickness of the membrane, the shape of the neuron or the interactions among ions (see Figure 2.2) [6] [21]. The Hodgkin-Huxley model captures two important facts about the neuron: (1) current conservation of the ions travelling through the membrane and (2) the voltage-dependent permeability of the neuron membrane to different ion currents [20]. The currents that flow through different ion channels across the membrane determine the dynamics of cross-membrane voltage. For example, sodium ions have a substantially higher concentration outside the membrane than inside. When the gates of sodium ion channels are open, the inflow of positively charged ions increases the cross-membrane potential [21]. When there is no outside signal to force the membrane voltage to change, a neuron is usually at a constant voltage called the "resting potential", which is around -65 mV for most neurons [6]. As the sodium current grows and the inner cell voltage increases, the membrane potential becomes "depolarized". On the other hand, potassium ions have a higher concentration inside the neuron, and they tend to flow outside when their ion gates are open. Therefore, the cross membrane voltage becomes more negative than the resting potential, and this phenomenon is defined as "hyper-polarization" [21] [8].

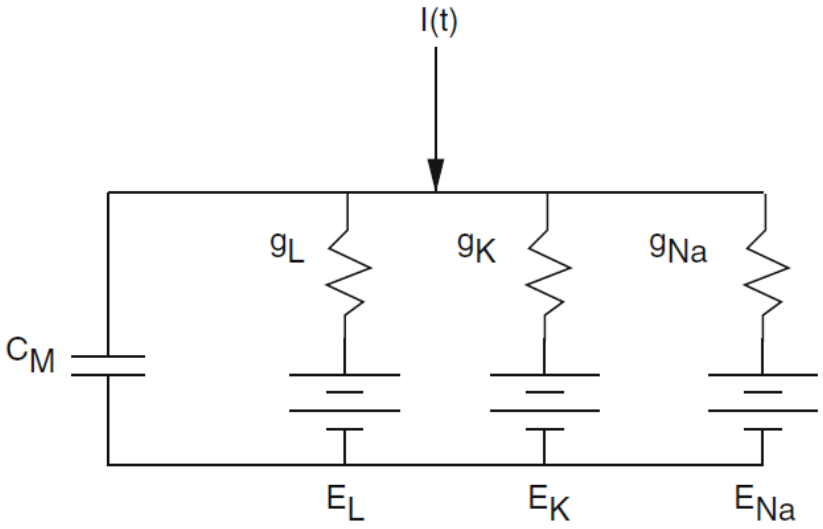

Figure 2.2. Equivalent circuit underlying the Hodgkin–Huxley equations. Reproduced from [13].

When there is an external current applied to the neuron, whether the signal comes from other neurons or artificial signal generators, the neuron may be depolarized to a potential that is high enough to make the neuron spike [36] [15]. For most membrane voltage data used in this chapter, the external current is an artificial signal designed to extract the most information from the cell. The outside current makes the single neuron a time-dependent system driven by a known dynamic stimulus. The only two quantities available from laboratory measurements are the cross-membrane voltage and the stimulus current driving the cell behavior. The dynamics of the most important state variable, the membrane potential $V(t)$, can be determined by the NaKL currents, the input stimulus and the membrane capacitance, according to the equivalent circuit in Figure 2.2 [6] [64]:

$$C\frac{dV(t)}{dt} = I_{\mathrm{Na}}(t) + I_{\mathrm{K}}(t) + I_{\mathrm{L}}(t) + I_{\mathrm{inj}}(t) \tag{2.13}$$

where $I_{\mathrm{inj}}(t)$ is the injected current from external equipment. C is the membrane capacitance which is set to a value of 1.0 μF [6][12]. Consider the equivalent circuit in Figure 2.2 and the fraction of open gates for different ion channels, the ion currents (I_{Na}, I_{K}, I_{L}) can be described

with the following set of equations in time [20]:

$$I_{\mathrm{Na}}(t) = g_{\mathrm{Na}} m(t)^3 h(t) (E_{\mathrm{Na}} - V(t)) \tag{2.14}$$

$$I_{\mathrm{K}}(t) = g_{\mathrm{K}} n(t)^4 (E_{\mathrm{K}} - V(t)) \tag{2.15}$$

$$I_{\mathrm{L}}(t) = g_{\mathrm{L}} (E_{\mathrm{L}} - V(t)) \tag{2.16}$$

In the above set of equations, all parameters denoted as "g" are the maximum conductance of corresponding ion channels. The parameters denoted by "E" are the respective reversal potentials, at which the corresponding ion current changes its sign. The three gating variables, $m(t)$, $h(t)$ and $n(t)$, are introduced in the model to describe the fraction of opening cross-membrane gates for sodium ($m(t)$ and $h(t)$) or potassium ion channels ($n(t)$), and their values vary between 0 and 1 without units since they denote fractional quantities[13] [12]. The leak current flows through nongated channels, so there is no gating variable in the I_{L} expression. In Eq (2.14), the term $n^4(t)$ represents the opening probability of the potassium channel since this channel consists of four identical components which act independently. The sodium channel is more complex: it contains two gates with probabilities of opening $m^3(t)$ and $h(t)$ respectively. Both gates must be open for Na^+ ions to travel across the membrane [13]. All these gating variables depend on the membrane potential, and they approach the steady-state values of $\eta_{\mathrm{m}}(V(t))/\eta_{\mathrm{h}}(V(t))/\eta_{\mathrm{n}}(V(t))$ at a rate determined by their respective time constants $\tau_{\mathrm{m}}(V(t))/\tau_{\mathrm{h}}(V(t))/\tau_{\mathrm{n}}(V(t))$:

$$\frac{dm(t)}{dt} = -\frac{m(t) - \eta_{\mathrm{m}}(V(t))}{\tau_{\mathrm{m}}(V(t))} \tag{2.17}$$

$$\frac{dh(t)}{dt} = -\frac{h(t) - \eta_{\mathrm{h}}(V(t))}{\tau_{\mathrm{h}}(V(t))} \tag{2.18}$$

$$\frac{dn(t)}{dt} = -\frac{n(t) - \eta_{\mathrm{n}}(V(t))}{\tau_{\mathrm{n}}(V(t))} \tag{2.19}$$

The values of the η's and τ's all depend on the voltage at the same time step. Their exact functions were derived by fitting the voltage clamp data and the idea that the rates of opening or closing a channel should depend on the potential exponentially [13] [64]:

$$\eta_{\mathrm{m}}(V(t)) = \frac{1}{2} + \frac{1}{2}\tanh\left(\frac{V(t) - V_{\mathrm{m}}}{\Delta V_{\mathrm{m}}}\right) \tag{2.20}$$

$$\tau_{\mathrm{m}}(V(t)) = \tau_{\mathrm{m0}} + \tau_{\mathrm{m1}}\left[1 - \tanh^2\left(\frac{V(t) - V_{\mathrm{m}}}{\Delta V_{\mathrm{m}}}\right)\right] \tag{2.21}$$

$$\eta_{\mathrm{h}}(V(t)) = \frac{1}{2} + \frac{1}{2}\tanh\left(\frac{V(t) - V_{\mathrm{h}}}{\Delta V_{\mathrm{h}}}\right) \tag{2.22}$$

$$\tau_{\mathrm{h}}(V(t)) = \tau_{\mathrm{h0}} + \tau_{\mathrm{h1}}\left[1 - \tanh^2\left(\frac{V(t) - V_{\mathrm{h}}}{\Delta V_{\mathrm{h}}}\right)\right] \tag{2.23}$$

$$\eta_{\mathrm{n}}(V(t)) = \frac{1}{2} + \frac{1}{2}\tanh\left(\frac{V(t) - V_{\mathrm{n}}}{\Delta V_{\mathrm{n}}}\right) \tag{2.24}$$

$$\tau_{\mathrm{n}}(V(t)) = \tau_{\mathrm{n0}} + \tau_{\mathrm{n1}}\left[1 - \tanh^2\left(\frac{V(t) - V_{\mathrm{n}}}{\Delta V_{\mathrm{n}}}\right)\right] \tag{2.25}$$

Here, V_x, ΔV_x, τ_{x0} and τ_{x1} are parameters for their corresponding gating variable $x(t)$. Collectively, there are four state variables and a set of 19 parameters (C, g_{Na}, E_{Na}, g_{K}, E_{K}, g_{L}, E_{L}, V_{m}, ΔV_{m}, τ_{m0}, τ_{m1}, V_{h}, ΔV_{h}, τ_{h0}, τ_{h1}, V_{n}, ΔV_{n}, τ_{n0}, τ_{n1}). These parameters can be treated as constants for each individual neuron, and their values determine the neuron's response to the injected stimulus. It has been an interesting and challenging problem for neuroscientists to discover these parameters for each individual neuron. Previous experiments show that even for the same type of neurons from the same brain, they can still show different behavior under the same external current [28].

2.2.2 Calcium channel

The calcium current is another type of current existing in HVC neurons [36] [28]. The circuit model of the sodium or potassium currents cannot fully describe the characteristics of the calcium channel [21]. Instead, The behavior of the calcium current is described by the Goldman–Hodgkin–Katz (GHK) equation to better reflect its current-voltage curve [62] [63]). Compared to the simple ohmic circuit describing the membrane potential (see Figure 2.2), the GHK equation adds extra nonlinearity to the current [13]. This is the general form of the GHK equation:

$$GHK(V(t)) = I_X = P_X Z_X F \frac{Z_X F V(t)}{RT} \left(\frac{X_{\text{in}} - X_{\text{out}} e^{-Z_X F V(t)/RT}}{1 - e^{-Z_X F V(t)/RT}} \right) \tag{2.26}$$

where I_X is the current density (flux) across the membrane carried by ion X; P_X is the permeability of the membrane for ion X; Z_X is the valence of X; F is the Faraday constant; R is the gas constant; T is the temperature measured in Kelvin; X_{in} is the intracellular concentration of ion X, while X_{out} is extracellular concentration.

Furthermore, we also need to consider the opening rate of channel gates for calcium ions. There are four broad classes of calcium currents that have been studied in neurons [21]. For neurons in the HVC region, the most important calcium current is CaT, the low threshold calcium current (T for Transient) [36] [53]. It is called a transient calcium current because of its strong voltage-dependent inactivation at rest potential. The CaT current is responsible for spontaneous bursts of neurons and also for their sub-threshold activity, thus it is an important part of the HVC neuron model [36] [53] [21].

This current can be reasonably represented by the GHK equation and a gating variable m_{CaT} [21]:

$$I(CaT(t)) = -m_{\text{CaT}}(t)^2 \cdot GHK(V(t)) \tag{2.27}$$

Combining the above formula and the GHK equation, the CaT current can finally be expressed as:

$$I(CaT(t)) = m_{\mathrm{CaT}}(t)^2 \cdot gV(t) \cdot \frac{1 - a\exp(-bV(t))}{1 - \exp(-bV(t))} \tag{2.28}$$

where

$$g = -P_X Z_X F \frac{Z_X F}{RT} \cdot X_{\mathrm{in}} \tag{2.29}$$

$$a = \frac{X_{\mathrm{out}}}{X_{\mathrm{in}}} \tag{2.30}$$

$$b = Z_X F / RT \tag{2.31}$$

The parameter b is just a combination of constants, which equals 0.078 mV^{-1}. To avoid division by zero error, we use the following formula when $V(t) = 0$:

$$I(CaT(t)) = m_{\mathrm{CaT}}(t)^2 \cdot g \cdot \frac{1 - a}{b} \tag{2.32}$$

2.2.3 NaP current

Another important ion channel in the HVC neurons is the NaP current (P represents "persistent"). It participates in the control of membrane excitability in the sub-threshold voltage region [23]. It is different from the regular sodium current since the NaP current is slowly inactivating and does not directly contribute to the transient action potential [23]. The behavior of the NaP current also differs from the sodium current in the NaKL model, but it can still be simulated with the reversal potential and the gating variable $hp(t)$. A well-suited equation describing its dynamics can be shown to be [36] [28]:

$$I(NaP(t)) = g_{\text{NaP}} \cdot \left(\frac{1}{1+\exp(\frac{V(t)-\theta_{\text{MP}}}{\sigma_{\text{MP}}})} \right) \cdot hp(t) \cdot (E_{\text{Na}} - V(t)) \tag{2.33}$$

with one state variable $hp(t)$:

$$\frac{dhp(t)}{dt} = \left(\frac{1}{1+\exp(\frac{V(t)-\theta_{\text{HP}}}{\sigma_{\text{HP}}})} - hp(t) \right) \cdot \left(\frac{\cosh(\frac{V(t)-\theta_{\text{HP}}}{2\cdot\sigma_{\text{HP}}})}{\overline{\tau_{\text{HP}}}} \right) \tag{2.34}$$

In the above two equations of the NaP current, the reversal potential E_{Na} is the same as that in the normal sodium current channel. Therefore, the NaP current introduces one state variable and six new parameters (g_{NaP}, θ_{MP}, σ_{MP}, θ_{HP}, σ_{HP}, $\overline{\tau_{\text{HP}}}$) to estimate.

2.3 Experiments on simulated data

2.3.1 Goal of experiments on simulated data

We are now ready to test the data assimilation method on the neuron model. Now the task is to estimate the state variables $m(t)$, $h(t)$, $n(t)$, $m_{\text{CaT}}(t)$ and $hp(t)$, along with a set of parameters $\boldsymbol{\theta}$. The only available data is a noisy version of the membrane voltage $V(t)$ and the injected current $I_{\text{inj}}(t)$. After transferring information from the voltage measurement to the multichannel neuron model, the completed model can be used to predict neuron behaviors under a new stimulus.

However, how can we verify that the estimation from our data assimilation method is approximately the true neuron behavior? So-called **twin experiments** are used to test how the data assimilation method works before it is applied to real lab data. The idea is that one can replace wet lab data with computer-generated data to perform tests or experiments.

To perform twin experiments, the first step is to generate voltage data from the HVC neuron model under a given stimulus, which is modeled here as a chaotic signal with added Gaussian white noise. The voltage data and the input current are treated as wet lab data. Then, the data assimilation method, PAHMC, was used to simulate the neuron behavior with the input

current, the output voltage and the neuron model, but all the parameters and other state variables are set as unknown. The statistical data assimilation process is supposed to estimate values of parameters, dynamics of unknown state variables, and a prediction of neuron behavior as if there is no available information about those parameters and state variables.

2.3.2 Stimulus current

During wet lab experiments, the only variable under control is the input current applied to the neuron by electrodes. This stimulus current needs to be designed to fully explore the dynamic range of the neuron so that the recorded voltage contains as much behavior information as possible. An example of a poor experimental stimulus would be a constant current. For a single neuron, it would either stay silent or show regular firing with a fixed frequency under constant currents. Not much information can be extracted from this simple behavior.

An ideal input current should be a current whose frequency spectrum mostly spans in the neurons' sensory range [6]. To achieve this, we use a chaotic signal as the input current. A cell membrane acts like a low-pass filter, so it will not be able to respond to any high frequency signals (approximately 150 Hz) [35]. The amplitude of the chaotic stimulus cannot be too high otherwise the neuron will be killed; it cannot be too low either or the neuron would never reach its action potential. The response to an ideal stimulus current should show both neuron spikes under depolarized voltage and neuron activities under hyper-polarized potential.

To be specific, our input data for the twin experiments arises from the x dimension of the Lorenz-63 system. In 1963, Edward Lorenz proposed a three-variable simplified model for atmospheric convection [25]. It was derived from the partial differential equations describing thermal convection in the lower atmosphere proposed by Barry Saltzman [26] [27]. This is a relatively simple but non-linear system which is a popular test bed for new statistical approaches. As a non-linear signal whose frequency spectrum mostly stays within neurons' sensory range, the x dimension of the Lorenz-63 system allows the neuron to show full dynamic range, both spiking and non-spiking. The simulated input current was generated by Randall Clark, my fellow

student, and is used in all the twin experiments in Section 2.4 (see Figure 2.3).

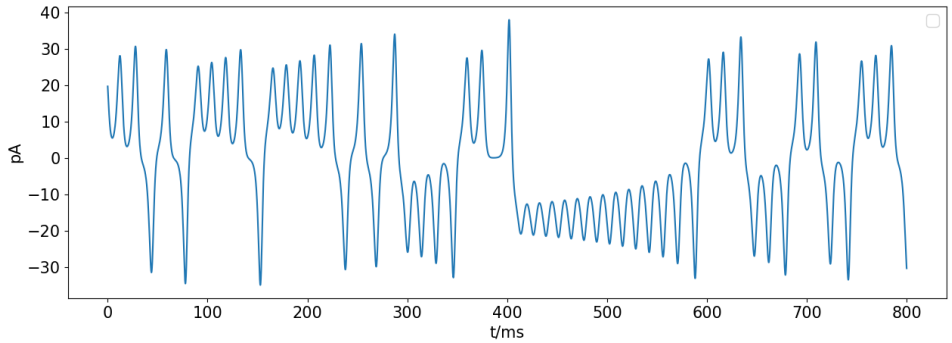

Figure 2.3. The simulated current. Used as the input stimulus in the twin experiments in Section 2.4. Courtesy of Randall Clark.

This univariate time series is the first dimension $x(t)$ of the solution to the Lorenz 63 dynamical system, described by the following equations (courtesy of Randall Clark):

$$\frac{dx}{dt} = 10(-x+y) \tag{2.35}$$

$$\frac{dy}{dt} = x(28-z)-y \tag{2.36}$$

$$\frac{dz}{dt} = -\frac{8}{3}z+xy \tag{2.37}$$

2.4 Data assimilation results

2.4.1 Twin experiment results on NaKL model

The twin experiment on NaKL model was repeated 5 times with the same input current from Section 2.3, each with different initial conditions and guessed values of parameters. All the twin experiments result in accurate estimations of parameters and predictions of future voltages. Next we will analyze those results.

In the calculations, the voltage data was generated using the trapezoidal rule with step size δt = 0.02 ms. A noise of $N(0,1)$ was then added to each $V(t)$ for t = 1,...,M, where M = 10,000 is the length of observation window. For precision annealing, we chose

$$R_f^a = R_{f0}^a \cdot \alpha^\beta \tag{2.38}$$

for a = (1,2,3,4), with $\alpha = 2.0$ and $\beta = 0,1,...,20$.

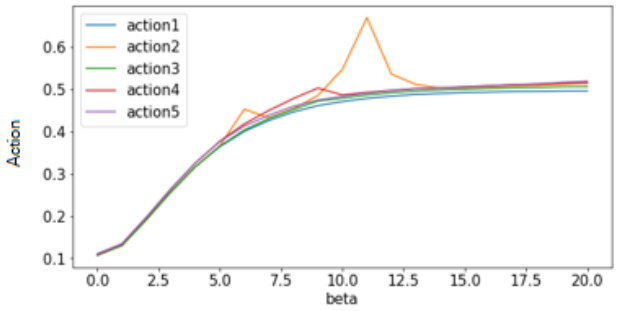

(a) Action

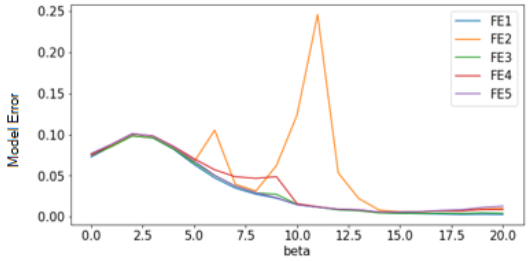

(b) Model Error

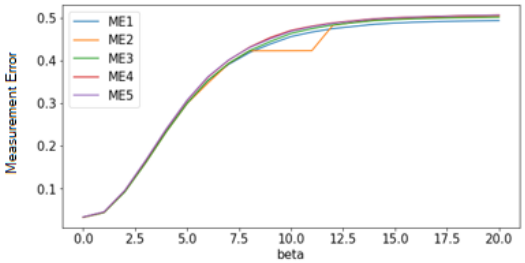

(c) Measurement Error

Figure 2.4. Action, model error and measurement error for PAHMC on the neuron model as a function of β for 5 trials, with $R_{f0}^V = 0.1$, $R_{f0}^m = 1200$, $R_{f0}^h = 1600$, $R_{f0}^n = 2100$, and $\alpha = 2.0$ (see Section 2.1). The value of R_f increases step by step in the precision annealing process. The action plateaus as R_f grows, implying the paths proposed by HMC start to agree with the neuron model.

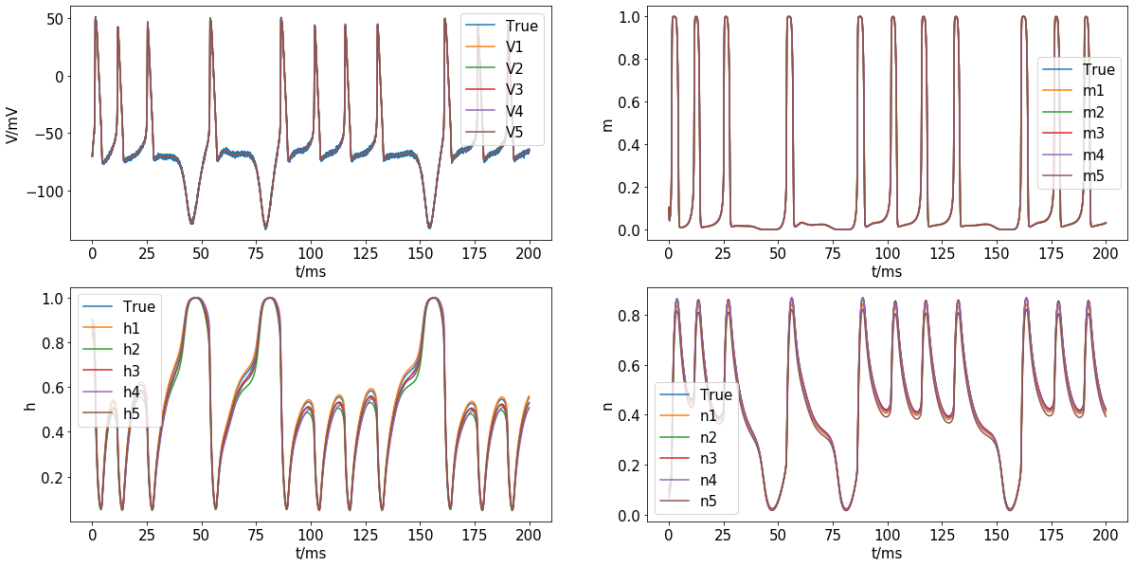

Figure 2.5. The estimated dynamics of state variables in a 200 ms time window (10,000 time steps). The estimated values for the membrane potential and the gating variables match well the true value.

The name and actual values of the model parameters are tabulated below. For their detailed meaning, please refer to Section 2.2.

Table 2.1. Actual values for parameters in the NaKL neuron model [64].

Index	par name	actual value	Unit	Index	par name	actual value	Unit
0	g_{Na}	120	mS	9	τ_{m1}	0.4	ms
1	E_{Na}	50	mV	10	V_h	-60	mV
2	g_{K}	20	mS	11	ΔV_h	-15	mV
3	E_{K}	-77	mV	12	τ_{h0}	1	ms
4	g_{L}	0.3	mS	13	τ_{h1}	7	ms
5	E_{L}	-54	mV	14	V_n	-55	mV
6	V_m	-40	mV	15	ΔV_n	30	mV
7	ΔV_m	15	mV	16	τ_{n0}	1	ms
8	τ_{m0}	0.1	ms	17	τ_{n1}	5	ms

For the five twin experiments, the initial guessed value of parameters are uniformly distributed in the range of $[0.75, 1.25]$ of their actual values. Since the initial conditions and guessed values of parameters are different random numbers for each trial, PAHMC may generate various predictions for the same group of parameters (see the result below).

Table 2.2. Predicted parameter values for NaKL model in the twin experiments in two significant figs. See Table 2.1 for the meaning of each parameter.

Index	True	Predict 1	Predict 2	Predict 3	Predict 4	Predict 5
0	1.2×10^2	1.2×10^2	1.5×10^2	1.3×10^2	1.4×10^2	1.4×10^2
1	50	50	50	50	50	50
2	20	24	20	20	21	27
3	-77	-77	-77	-77	-77	-77
4	0.30	0.30	0.30	0.30	0.30	0.30
5	-54	-54	-54	-54	-54	-54
6	-40	-40	-39	-40	-40	-40
7	15	15	15	15	15	15
8	0.10	0.10	0.11	0.10	0.12	0.11
9	0.40	0.41	0.36	0.38	0.40	0.39
10	-60	-60	-62	-61	-60	-62
11	-15	-14	-17	-16	-14	-16
12	1.0	1.0	0.9	1.0	0.9	1.0
13	7.0	7.6	5.4	6.8	10	5.6
14	-55	-54	-54	-54	-54	-52
15	30	32	32	31	32	34
16	1.0	1.1	0.9	1.0	0.9	1.1
17	5.0	4.8	5.2	5.1	5.0	4.8

From the predicted parameters given by PAHMC, the voltage can be calculated after the estimation window:

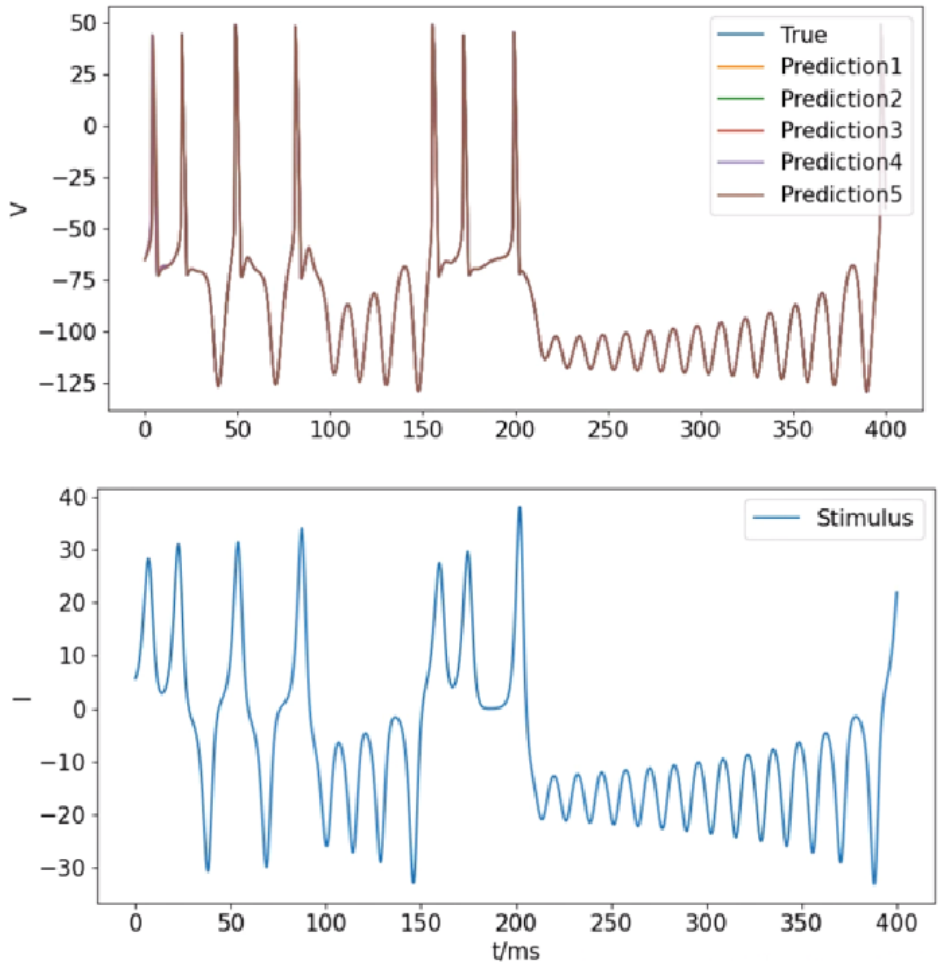

Figure 2.6. Predicted voltage and the stimulus current after the training window. The prediction of voltage for each twin experiment is very close to the true value.

2.4.2 Twin experiment results on NaKL+GHK

The twin experiment on NaKL+GHK model was repeated 10 times under the same stimulus current, each with different initial conditions and random guessed values of parameters. Seven out of these nine trials show that actions plateau at high values of R_f, which indicate that PAHMC gets satisfactory estimations of state variables. Please see Section 2.4.5 for discussion about unsuccessful twin experiments.

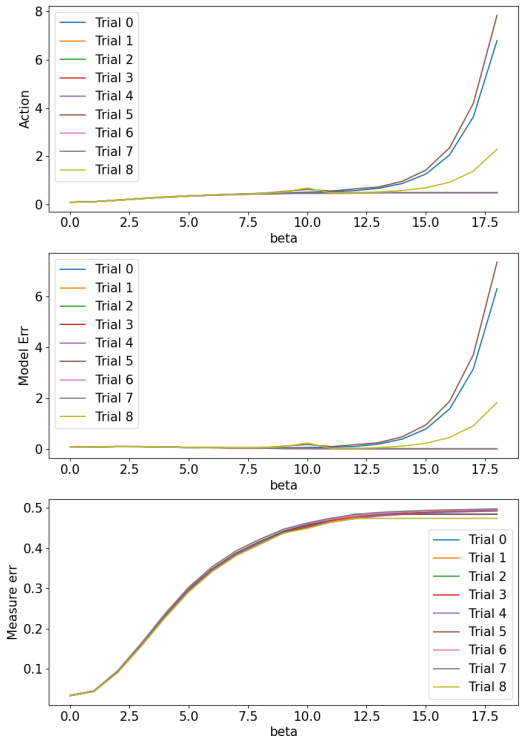

Figure 2.7. Action, model error and measurement error for PAHMC on the neuron model as a function of β for the nine trials, with $R^V_{f0} = 0.1$, $R^m_{f0} = 1200$, $R^h_{f0} = 1600$, $R^n_{f0} = 2100$, and $\alpha = 2.0$ (see Section 2.1). The value of R_f increases step by step in the precision annealing process. In seven out of nine twin experiments, the action plateaus as R_f grows, implying the paths proposed by HMC start to agree with the neuron model.

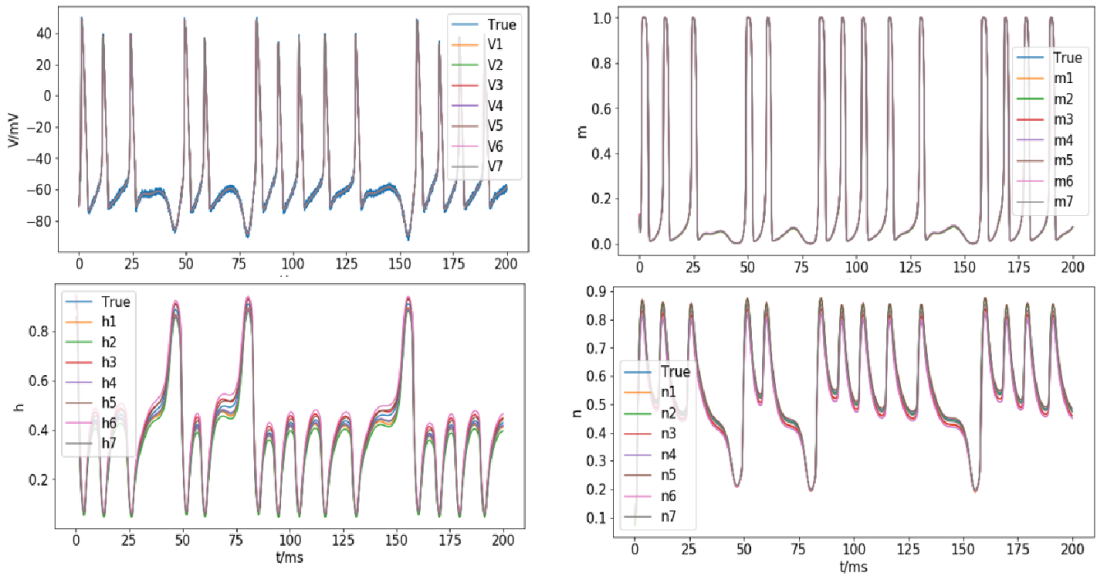

Figure 2.8. The estimated state variables in a 200 ms time window (10,000 time steps) of the 7 successful trials. The estimated values for the membrane potential and the gating variables are close to the true values.

The name and actual values of the model parameters are tabulated below. For their detailed meaning, please refer to Section 2.2.

Table 2.3. Actual values for parameters in the NaKL+GHK neuron model [64][21]

Index	par name	actual value	Unit	Index	par name	actual value	Unit
0	g_{Na}	120	mS	10	V_h	-60	mV
1	E_{Na}	50	mV	11	δV_h	-15	mV
2	g_{K}	20	mS	12	τ_{h0}	1	ms
3	E_{K}	-77	mV	13	τ_{h1}	7	ms
4	g_{L}	0.3	mS	14	V_n	-55	mV
5	E_{L}	-54	mV	15	δV_n	30	mV
6	V_m	-40	mV	16	τ_{n0}	1	ms
7	δV_m	15	mV	17	τ_{n1}	5	ms
8	τ_{m0}	0.1	ms	18	$\frac{g}{-e^{-5}}$	2	mS
9	τ_{m1}	0.4	ms	19	a	10000	

For the seven twin experiments, the initial guessed values of parameters are uniformly distributed in the range of $[0.75, 1.25]$ of their actual values. Since the initial conditions and guessed values of parameters are different random numbers for each trial, PAHMC may generate various predictions for the same group of parameters (see results below).

Table 2.4. Predicted parameter values for NaKL+GHK model in the twin experiments with two significant figures. See Table 2.3 for the meaning of each parameter.

Index	True	Pred 1	Pred 2	Pred 3	Pred 4	Pred 5	Pred 6	Pred 7
0	1.2e2	1.2e2	1.5e2	1.5e2	1.1e2	1.2e2	1.1e2	1.0e2
1	50	50	50	50	50	50	50	50
2	20	21	24	21	24	26	19	26
3	-77	-77	-76	-77	-77	-77	-77	-77
4	0.30	0.24	0.38	0.25	0.30	0.32	0.32	0.34
5	-54	-67	-41	-66	-48	-46	-50	-41
6	-40	-40	-40	-40	-40	-40	-40	-40
7	15	15	15	15	15	15	15	15
8	0.10	0.09	0.11	0.11	0.09	0.09	0.10	0.09
9	0.40	0.39	0.42	0.40	0.42	0.40	0.40	0.42
10	-60	-61	-62	-62	-60	-61	-59	-59
11	-15	-16	-15	-16	-14	-16	-14	-14
12	1.0	1.0	1.0	1.0	1.0	1.0	1.0	1.1
13	7.0	5.8	5.7	6.0	6.9	5.8	8.0	7.9
14	-55	-54	-54	-55	-54	-53	-55	-53
15	30	31	32	31	32	33	29	32
16	1.0	1.1	1.0	0.94	1.1	1.2	1.0	1.2
17	5.0	5.0	4.8	5.0	4.8	4.8	5.1	4.7
18	2.0	2.5	1.3	3.2	2.2	1.5	1.9	1.3
19	1.0e4	1.0e4	0.84e4	0.78e4	0.79e4	1.1e4	0.93e4	0.98e4

The predicted values are quite close to their true ones, except for the two parameters for the GHK equation. The reason may be that the calcium current is too small, so it has little impact

on the voltage. We will fix this problem in Section 2.4.3 by increasing the value of g.

From the estimated parameters given by PAHMC, the voltage can be predicted after the estimation window:

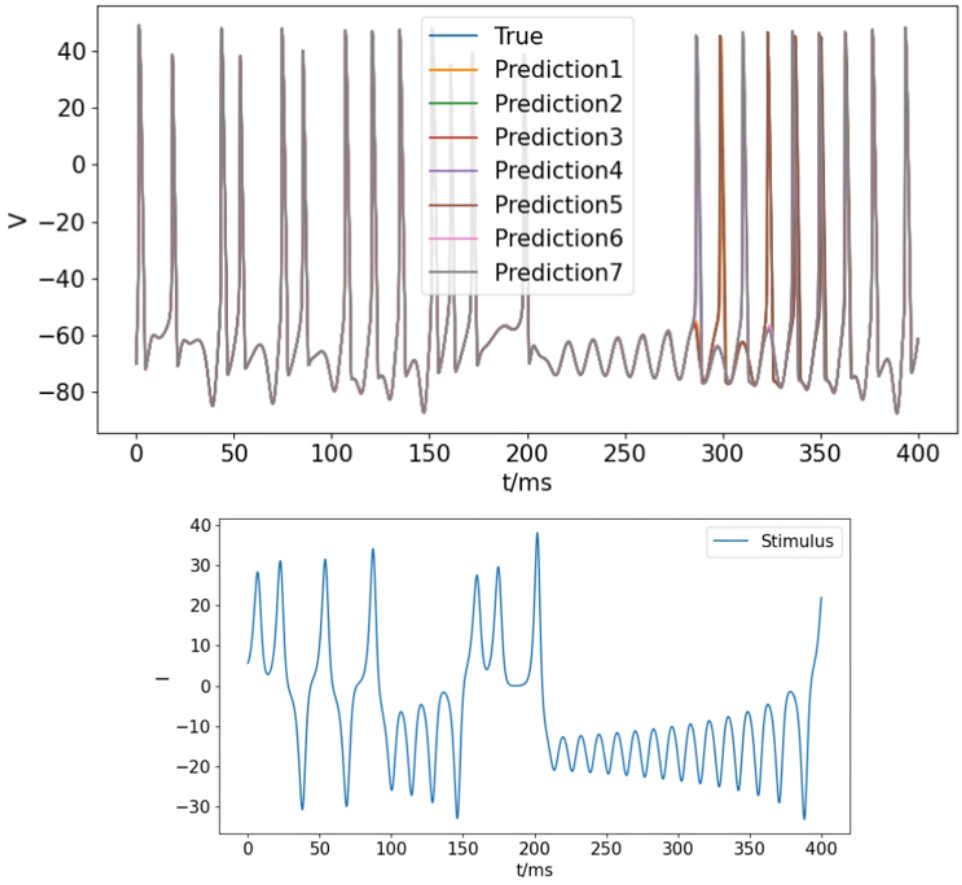

Figure 2.9. Predicted voltage and the stimulus current after the training window. The predictions of the voltage for the twin experiments is very close to the true value.

2.4.3 Twin experiment results on NaKL+CaT

The twin experiment on NaKL+CaT model was repeated 9 times under the same stimulus current, each with different initial conditions and random guessed values of parameters. Since this model is more complicated now, α is chosen to be 1.5 and M is 20,000 to allow more accurate estimations of state variables and parameters.

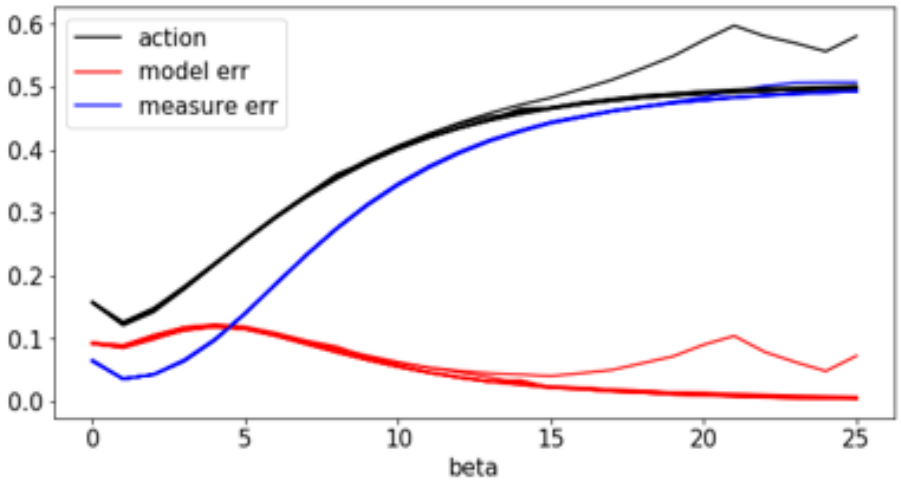

Figure 2.10. Action, model error and measurement error for PAHMC on the neuron model as a function of β for 9 trials, with $R^V_{f0} = 0.1$, $R^m_{f0} = 1200$, $R^h_{f0} = 1600$, $R^n_{f0} = 2100$, $R^{m(CaT)}_{f0} = 1500$ and $\alpha = 1.5$ (see Section 2.1). The value of R_f increases step by step in the precision annealing process. In four out of nine twin experiments, the model error decrease below 0.005 as R_f grows, implying the paths proposed by HMC agree well with the neuron model.

Among the 9 trials, 4 of them, i.e. trial 1,3,6,7, have a model error less than 0.005 at the maximum β, which imply that the estimated gating variables and parameters should be close to the actual values [6]. These four trials are considered as successful trials, and only they will be analyzed in the following part. Please see Section 2.4.5 for discussion about unsuccessful twin experiments.

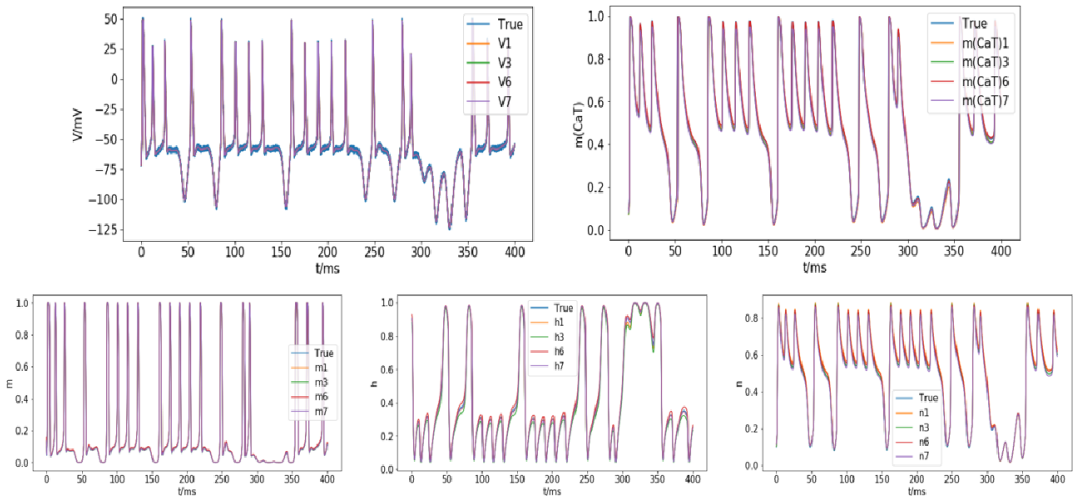

Figure 2.11. The estimated state variables in a 400 ms time window (20,000 time steps) of the 4 successful trials. The estimated values for the membrane potential and the gating variables are close to the true values.

The actual and estimated values of the model parameters are tabulated below. To improve the estimation of CaT current parameters, g of CaT is ten times as big as that in Section 2.4.2. For their detailed meaning, please refer to Section 2.2.

Table 2.5. Actual values for parameters in the NaKL+CaT neuron model [64] [21]

Index	par name	actual value	Unit	Index	par name	actual value	Unit
0	g_{Na}	120	mS	12	τ_{h0}	1	ms
1	E_{Na}	50	mV	13	τ_{h1}	7	ms
2	g_{K}	20	mS	14	V_n	-55	mV
3	E_{K}	-77	mV	15	δV_n	30	mV
4	g_{L}	0.3	mS	16	τ_{n0}	1	ms
5	E_{L}	-54	mV	17	τ_{n1}	5	ms
6	V_m	-40	mV	18	$\frac{g}{-e^{-5}}$	20	mS
7	δV_m	15	mV	19	$\frac{a}{e^4}$	1	
8	τ_{m0}	0.1	ms	20	$V_{m(CaT)}$	-50	mV
9	τ_{m1}	0.4	ms	21	$\delta V_{m(CaT)}$	30	mV
10	V_h	-60	mV	22	$\tau_{m(CaT)0}$	0.02	ms
11	δV_h	-15	mV	23	$\tau_{m(CaT)1}$	6	ms

For the four twin experiments, the initial guessed values of parameters are uniformly distributed in the range of $[0.75, 1.25]$ of their actual values. Since the initial conditions and guessed values of parameters are different random numbers for each trial, PAHMC may generate various predictions for the same group of parameters (see results below).

Table 2.6. Predicted parameter values for NaKL+CaT model in the twin experiments with two significant figures. See Table 2.5 for the meaning of each parameter.

Index	True	Pred 1	Pred 3	Pred 6	Pred 7
0	1.2×10^2	1.1×10^2	1.4×10^2	1.0×10^2	1.3×10^2
1	50	50	50	50	50
2	20	14	19	17	22
3	-77	-90	-80	-82	-80
4	0.30	0.30	0.30	0.30	0.30
5	-54	-54	-54	-54	-54
6	-40	-40	-40	-40	-40
7	15	15	15	15	15
8	0.10	0.09	0.10	0.08	0.10
9	0.40	0.38	0.39	0.39	0.41
10	-60	-61	-62	-59	-60
11	-15	-16	-16	-15	-15
12	1.0	1.0	1.0	1.0	1.0
13	7.0	6.5	6.3	7.8	6.6
14	-55	-56	-55	-56	-54
15	30	30	31	30	31
16	1.0	0.9	0.9	1.0	1.0
17	5.0	6.0	5.3	5.4	5.1
18	20	20	18	23	20
19	1.0	1.6	1.4	1.0	1.2
20	-50	-49	-49	-50	-49
21	30	28	29	28	29
22	0.02	0.20	0.16	0.10	0.16
23	6.0	6.8	6.2	6.3	6.2

From the predicted parameters given by PAHMC, the voltage can be calculated after the estimation window:

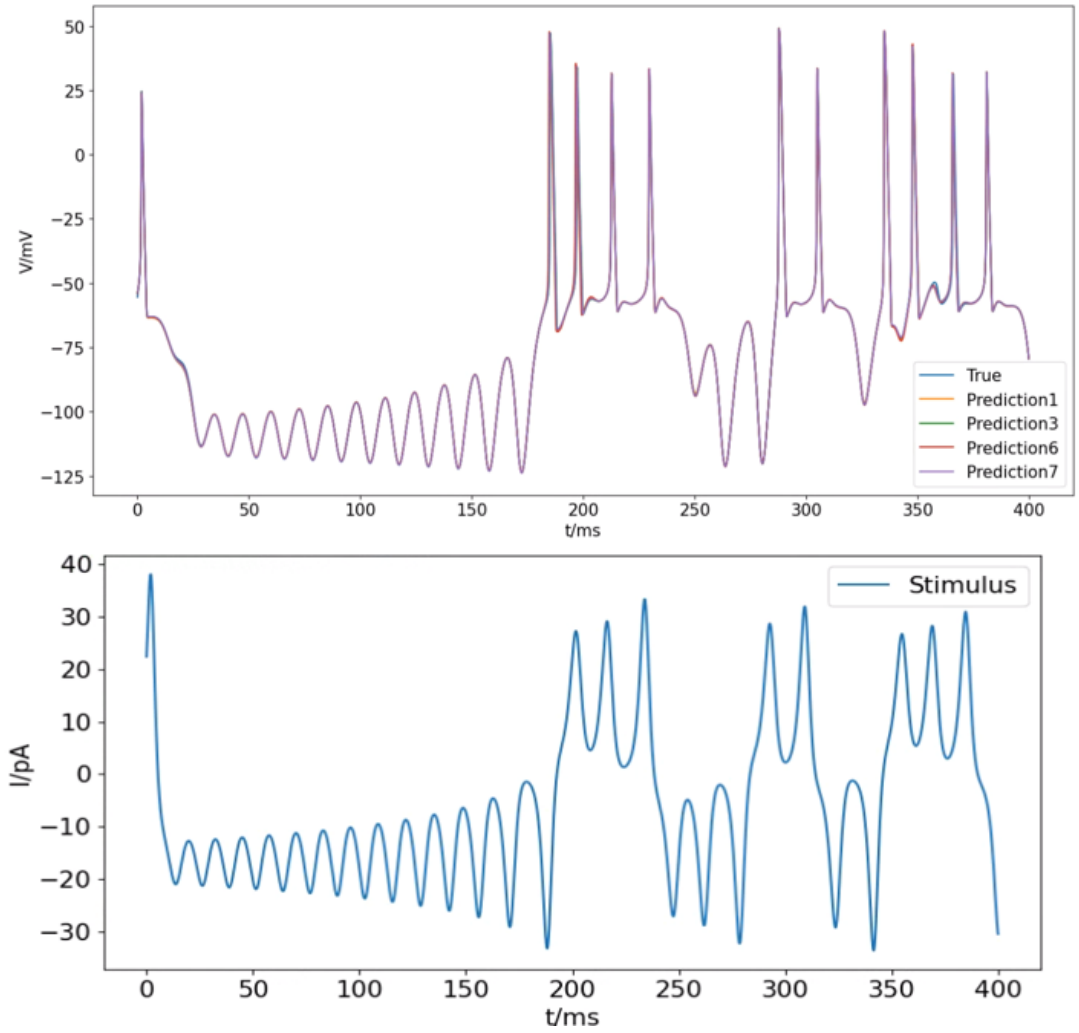

Figure 2.12. Predicted voltage and the stimulus current after the training window. The predictions of the voltage for the twin experiments is very close to the true value.

2.4.4 Twin experiment results on NaKL+CaT+NaP

The twin experiment on NaKL+CaT+NaP model was repeated 12 times under the same stimulus current, each with different initial conditions and random guessed values of parameters. Since the model is getting more complicated, α is chosen to be 1.5 and M is 20,000 for more accurate estimations of state variables and parameters.

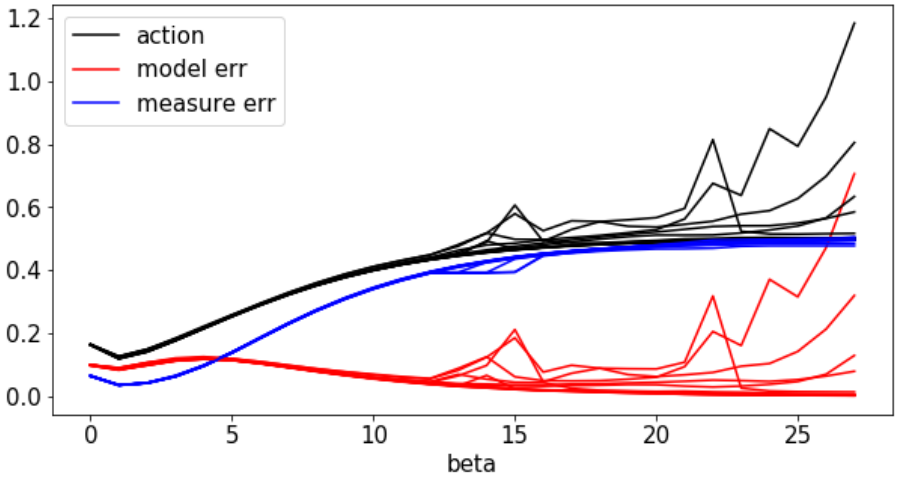

Figure 2.13. Action, model error and measurement error for PAHMC on the neuron model as a function of β for 12 trials, with $R^V_{f0} = 0.1$, $R^m_{f0} = 1200$, $R^h_{f0} = 1600$, $R^n_{f0} = 2100$, $R^{m(CaT)}_{f0} = 1500$, $R^{hp}_{f0} = 1100$ and $\alpha = 1.5$ (see Section 2.1). The value of R_f increases step by step in the precision annealing process. In five out of twelve twin experiments, the model error decrease below 0.005 as R_f grows, implying the paths proposed by HMC agree well with the neuron model.

Among the 12 trials, 5 of them, i.e. trial 1,2,3,4,8, have a model error less than 0.005 at maximum β, which implies that the estimated gating variables and parameters should be close to the actual values [6]. These five trials are likely to be successful trials because of their low model errors, and only they will be analyzed in the following part. Please see Section 2.4.5 for discussion about unsuccessful twin experiments.

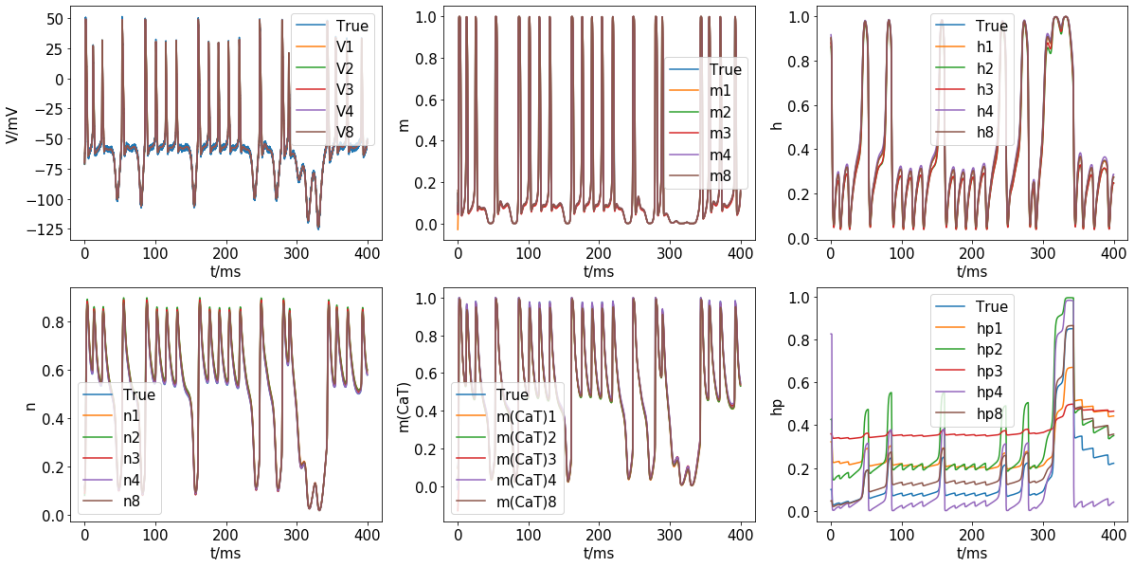

Figure 2.14. The estimated state variables in a 400 ms time window (20,000 time steps) of the 5 successful trials. The estimated values for the membrane potential and most gating variables are close to the true values. Estimations for $hp(t)$ do not perfectly match the real dynamics. See Section 2.5 for more discussion.

The actual and estimated values of the model parameters are tabulated below. For their detailed meaning, please refer to Section 2.2.

Table 2.7. Actual values for parameters in the NaKL+CaT+NaP neuron model [64] [21] [28]

Index	par name	actual value	Unit	Index	par name	actual value	Unit
0	g_{Na}	120	mS	15	δV_n	30	mV
1	E_{Na}	50	mV	16	τ_{n0}	1	ms
2	g_{K}	20	mS	17	τ_{n1}	5	ms
3	E_{K}	-77	mV	18	$\frac{g}{-e^{-5}}$	20	mS
4	g_{L}	0.3	mS	19	$\frac{a}{e^4}$	1	
5	E_{L}	-54	mV	20	$V_{m(CaT)}$	-50	mV
6	V_m	-40	mV	21	$\delta V_{m(CaT)}$	30	mV
7	δV_m	15	mV	22	$\tau_{m(CaT)0}$	0.02	ms
8	τ_{m0}	0.1	ms	23	$\tau_{m(CaT)1}$	6	mV
9	τ_{m1}	0.4	ms	24	g_{NaP}	0.2	mS
10	V_h	-60	mV	25	θ_{MP}	-40	mV
11	δV_h	-15	mV	26	σ_{MP}	-6	mV
12	τ_{h0}	1	ms	27	θ_{HP}	-48	mV
13	τ_{h1}	7	ms	28	σ_{HP}	6	mV
14	V_n	-55	mV	29	$\overline{\tau_{\mathrm{HP}}}/1000$	1	ms

For the five twin experiments, the initial guessed values of parameters are uniformly distributed in the range of $[0.75, 1.25]$ of their actual values. Since the initial conditions and guessed values of parameters are different random numbers for each trial, PAHMC may generate various predictions for the same group of parameters (see results below).

Table 2.8. Predicted parameter values for NaKL+CaT+NaP model in the twin experiments with two significant figures. See Table 2.7 for the meaning of each parameter.

Index	True	Pred 1	Pred 2	Pred 3	Pred 4	Pred 8
0	1.2×10^2	1.1×10^2	1.4×10^2	1.5×10^2	1.1×10^2	1.1×10^2
1	50	50	50	50	50	50
2	20	15	16	19	20	16
3	-77	-88	-83	-76	-77	-84
4	0.30	0.30	0.30	0.30	0.30	0.30
5	-54	-54	-55	-55	-54	-54
6	-40	-40	-40	-40	-40	-40
7	15	15	15	15	15	15
8	0.10	0.09	0.11	0.11	0.09	0.09
9	0.40	0.39	0.38	0.42	0.40	0.39
10	-60	-60	-62	-62	-59	-60
11	-15	-15	-16	-16	-15	-15
12	1.0	1.0	0.9	0.9	1.0	1.0
13	7.0	6.7	6.4	6.8	7.2	6.9
14	-55	-56	-56	-55	-55	-56
15	30	30	30	30	30	30
16	1.0	1.0	0.9	0.9	1.0	1.0
17	5.0	5.6	5.4	5.0	5.0	5.4
18	20	22	24	23	16	19
19	1.0	1.4	1.1	0.8	1.2	1.4
20	-50	-49	-49	-50	-51	-50
21	30	28	29	30	29	28
22	0.02	0.22	0.17	0.06	0.05	0.19
23	6.0	6.3	6.1	5.8	6.0	6.2
24	0.20	0.10	0.09	1.07	0.04	0.03
25	-40	-45	-43	-31	-51	-50
26	-6.0	-4.1	-4.7	-6.8	-5.3	-5.2
27	-48	-46	-41	-46	-52	-45
28	6.0	6.7	6.1	9.0	5.8	6.0
29	1.0	1.3	0.6	1.6	0.4	1.2

From the predicted parameters given by PAHMC, the voltage can be calculated after the estimation window:

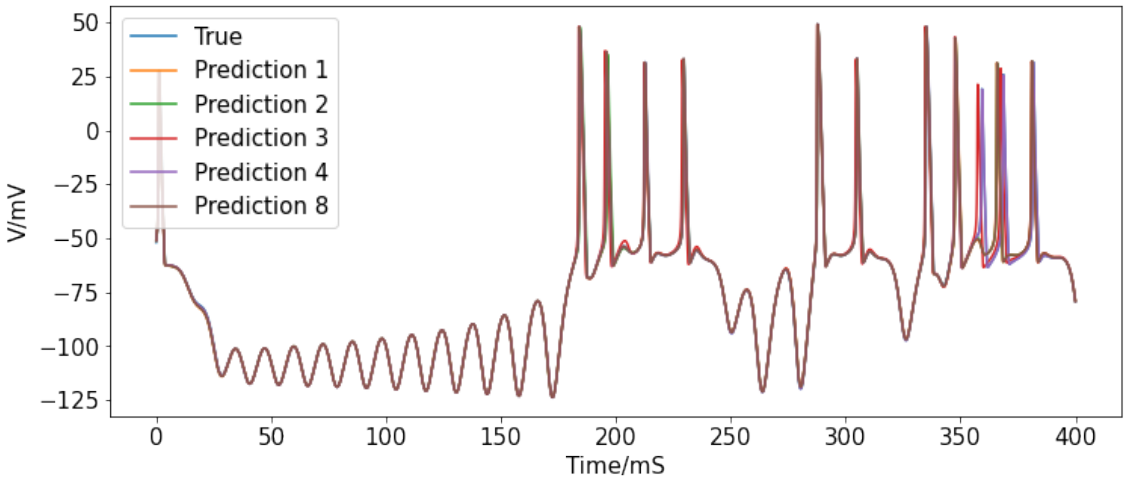

Figure 2.15. Predicted voltage after the training window. The predictions of the voltage for the twin experiments is very close to the true value.

2.4.5 Unsuccessful twin experiment

A small value of model error at the end of the precision annealing process usually implies that the data assimilation method has discovered the actual parameter values and thus the right model. Here we illustrate the results of the unsuccessful twin experiments on NaKL+CaT+NaP neuron model, which is the most complicated model proposed in this chapter. As stated in Section 2.4.4, 7 of the 12 trials have large model error at the end of the data assimilation process, i.e. trial 5,6,7,9,10,11,12, and the predicted parameter values given by these seven trials are shown below in Table 2.10. The differences between predicted values and actual values for some parameters, including No.2, No.3, and No.6, are much larger than that in Table 2.8.

Table 2.9. Actual values for parameters in the NaKL+CaT+NaP neuron model [64] [21] [28]

Index	par name	actual value	Unit	Index	par name	actual value	Unit
0	g_{Na}	120	mS	15	δV_n	30	mV
1	E_{Na}	50	mV	16	τ_{n0}	1	ms
2	g_{K}	20	mS	17	τ_{n1}	5	ms
3	E_{K}	-77	mV	18	$\frac{g}{-e^{-5}}$	20	mS
4	g_{L}	0.3	mS	19	$\frac{a}{e^4}$	1	
5	E_{L}	-54	mV	20	$V_{m(CaT)}$	-50	mV
6	V_m	-40	mV	21	$\delta V_{m(CaT)}$	30	mV
7	δV_m	15	mV	22	$\tau_{m(CaT)0}$	0.02	ms
8	τ_{m0}	0.1	ms	23	$\tau_{m(CaT)1}$	6	mV
9	τ_{m1}	0.4	ms	24	g_{NaP}	0.2	mS
10	V_h	-60	mV	25	θ_{MP}	-40	mV
11	δV_h	-15	mV	26	σ_{MP}	-6	mV
12	τ_{h0}	1	ms	27	θ_{HP}	-48	mV
13	τ_{h1}	7	ms	28	σ_{HP}	6	mV
14	V_n	-55	mV	29	$\overline{\tau_{\mathrm{HP}}}/1000$	1	ms

Table 2.10. Predicted parameter values for NaKL+CaT+NaP model in the unsuccessful twin experiments with two significant figures. See Table 2.9 for the meaning of each parameter.

Index	True	Pred 5	Pred 6	Pred 7	Pred 9	Pred 10	Pred 11	Pred 12
0	1.2×10^2	1.1×10^2	1.5×10^2	1.4×10^2	1.5×10^2	1.2×10^2	1.1×10^2	1.6×10^2
1	50	49.2	49.6	50.3	50	49.7	49.2	49.1
2	20	46.5	22.4	46.8	48	15.7	51.7	24
3	-77	-107	-86.9	-10.6	-1.9	-97.4	-104	-111
4	0.3	-7.83	0.302	0.297	0.29	0.3	-12.2	0.303
5	-54.4	-47.9	-54.9	-53.3	-52	-54.5	-54.1	-55.3
6	-40	-48.7	-39.9	-49.9	-51	-40.2	-45.9	-40.2
7	15	9.95	15	13.7	12	15.1	11.8	14.4
8	0.1	0.0884	0.112	0.0901	0.11	0.0931	0.0843	0.107
9	0.4	4.67	0.385	4.59	4.4	0.37	2.12	0.408
10	-60	-56.3	-62.6	-56.3	-56	-62.2	-50.7	-66.3
11	-15	-19.6	-16.3	-14.9	-13	-16.8	-14.3	-18
12	1	0.0781	0.97	0.644	0.56	0.981	0.095	0.938
13	7	33.8	6.58	25.5	31	6.19	45.9	5.98
14	-55	-64	-53.1	-56.2	-55	-54.5	-74.8	-49
15	30	51.7	34.2	30	31	33.1	64	37.9
16	1	41.2	1.01	1.34	1.4	0.993	48.2	1.08
17	5	19.6	5.13	1.83	2.3	5.72	26.9	6.13
18	20	26.1	21.5	26.2	22	15.9	29.8	21.7
19	1	12	1.74	-12.6	-16	2.6	18.7	3.21
20	-50	-48.9	-47.2	-51.7	-51	-48.3	-49.8	-43.8
21	30	40.2	28.8	14.1	15	27.4	23.2	28.6
22	0.02	-51.2	0.339	1.13	1.4	0.369	-235	0.594
23	6	-7.82	5.97	2.48	2.4	6.43	4.8	6.98
24	0.2	17.8	-0.429	3.16	1.6	-0.126	5.85	1.24
25	-40	-38.1	-39.9	-33.6	-40	-35.7	-30.7	-28.1
26	-6	-7.3	-4.04	-6.44	-5.6	-7.96	-11.3	-5.92
27	-48	-61.7	-52.5	-40.1	-34	-59	-37	-43.9
28	6	6.96	5.59	13.1	4.3	7.38	6.63	11.2
29	1	2.39	0.377	0.0217	1.5	0.279	0.303	3.45

One possible reason for unsuccessful twin experiments is that when randomly initiating the path space, the state variables and the parameter values start at a position far from the global minimum, so it is too hard to walk back to the right point. We finally exclude this hypothesis since the distance between initial parameter guess and their true values are similar for all twin experiments (see following graph):

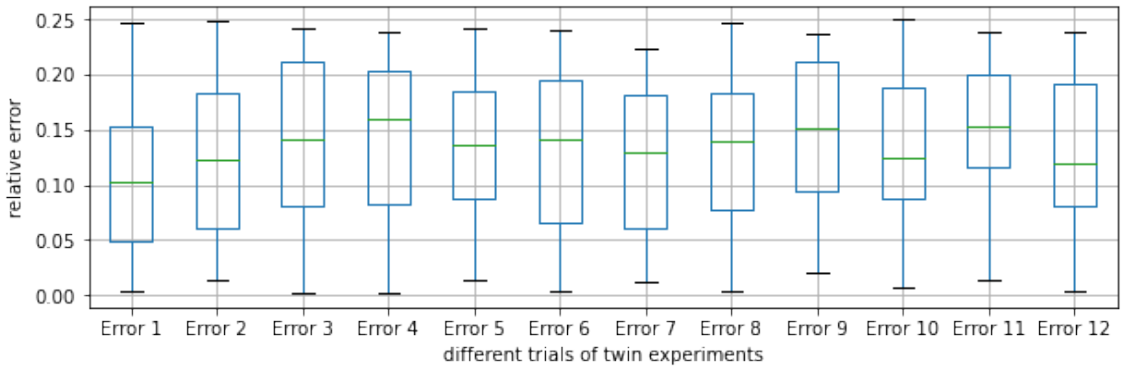

Figure 2.16. Distribution of relative error between initial parameter guess and their true values for all twin experiments. The distributions are similar for all trials.

2.5 Discussion

In this chapter, we introduce HVC neuron models and twin experiments. In Section 2.4, several twin experiments are accomplished with different neuron models from the simplest Hodgkin-Huxley model to the complex NaKL+CaT+NaP channels. The first step of twin experiments is to generate membrane potentials while a chaotic stimulus current is applied to the HVC neuron model. Then, the voltage with a Gaussian noise and the neuron formulas without parameter values are treated as known information. The goal of data assimilation is to estimate other unknown state variables (m, h, n, etc.) and parameter values controlling neuron dynamics. Even if different sets of parameters can sometimes lead to similar neuron dynamics, the data assimilation results still provide a perspective to understand the mechanism behind different neuron dynamics.

Actions, estimations of state variables and parameter values, and prediction of future

voltages are key elements to evaluate the performance of data assimilation during twin experiments. From the above twin experiment results, some actions reach a steady value at large β, meaning that the model error is approaching 0 and our approach has reached a reasonable estimation of underlying state variables [6] [8]. The measurement error should go to a value of around 1 due to the injected noise on top of the voltage in the training window. This means the action should also be around 1 as the model error decreases towards zero. However, there are several times when actions and model errors keep increasing. The reason may be that (1) when randomly exploring the path space, the sampling is trapped in a local minimum; (2) when exploring the path space, the step size is too large, so the minimum position is missed in the precision annealing procedure. Exploring the reason for every failed twin experiments is out of the scope for this paper. We did not address this problem because when fitting a neuron model, one can always conduct multiple data assimilation experiments in parallel, abandon those with large model errors, and only verify the data assimilation results with low action values. Existence of failed data assimilation experiments does not stop us from estimation and prediction as long as some experimental results describe the neuron dynamics accurately. If someone is interested in increasing the successful rate of PAHMC, they can try to limit the range of initial path space, or increase the amount of data in the estimation window, or apply Precision Annealing with smaller increment steps.

We explore the HVC neuron model from basic channels (NaKL) to complicated ones step by step. When it finally comes to the NaKL+CaT+NaP model, for those experiments which successfully reach a steady action value, most estimations of state variables ($V, m, h, n, m(CaT)$ and hp) and parameter values are close to their true numbers. The undesirable estimations mostly happen on the NaP ion channel including the state variable hp and its parameters. It is possibly because that the NaP channel has little influence on the voltage compared to other ion currents. Data assimilation finds the correct answer as exemplified by its action, measurement error, and model error graphs. The error comes from the fact that the NaP channel is implemented in a way that does not have significant bearing on the voltage of the neuron, which is what data assimilation

has to train on; as a result, the training process fails to pick up on the key features of the NaP channel. The fact that the prediction of membrane voltage is nearly perfect regardless of bad estimations of NaP current supports this interpretation (see Figure 2.17). Future studies can be carried out to explore the sensitivity of single neuron voltage to each parameter and ion channels. Quantification of changes in dynamics of state variables induced by different parameter values and ion current strength will help to understand the significance of those currents and parameters to neuron behavior. Different parts of the neuron model may contribute to different aspects of neuron dynamics such as spike frequency, action potential or hyperpolarization behavior, etc.

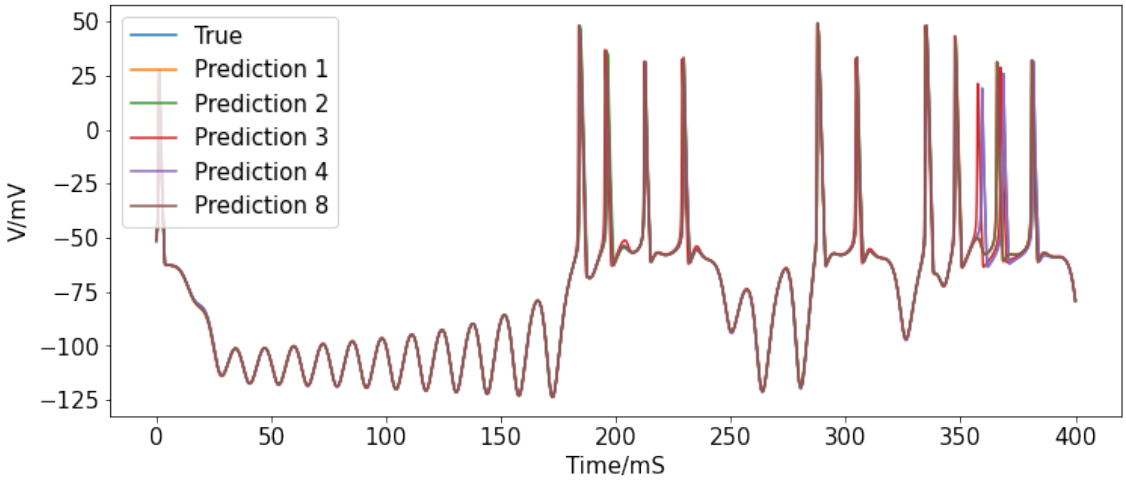

Figure 2.17. Predicted voltage after the training window for NaKL+CaT+NaP neuron model. The predictions of the voltage for the twin experiments is very close to the true value even if the estimations of the state variable and parameters for NaP channel are not ideal.

Unfortunately, PAHMC failed in fitting the voltage of real HVC neurons to the NaKL + CaT + NaP model. Dan Margolish's lab in Chicago University applied a chaotic stimulus current to HVC neurons *in vitro* and recorded their voltage responses. After applying PAHMC to a single neuron's data, the model errors remained large at the end of the searching process, which implied that the estimated neuron model did not describe the time-course of the training data accurately. The data assimilation results offered different estimations of the value of parameters and the dynamics of unknown state variables, but none of them correctly predicted the future voltage traces of the neuron outside the training window. Possible reasons for this failure may be that:

- some ion channels which may exist in some HVC neurons were not included in the proposed neuron model, such as the calcium-activated potassium current or the A-type potassium current whose dynamics is different from the existing ion current equations [36].
- the equations for some ion channels did not match the dynamics of the actual ion currents [37] [53].
- the initial estimations of parameters were so far away from the actual values that it was too hard for PAHMC to jump to the global minimum.

Possible solutions to overcome these limitations could be (1). adding additional ion channels to the neuron model and playing with various dynamic equations for ion currents, or (2). exploring data assimilation methods with higher successful rate in locating the global minimum.

Chapter 3

HVC neuron network

3.1 HVC microcircuits

3.1.1 Background

Bird song is a specific type of vocalization which is unique to passerine (perching) birds [14]. The specialized neural circuit which controls the song is the song motor pathway. The song circuit is stereotyped, so it is promising that the song motor pathway can be understood on a cellular level. One important scientific interest in birdsong systems is to study the behavior, interactions and functions of this specialized group of neurons governing song production in the central nervous system [36] [47] [41].

Among various song birds, adult zebra finches are one of the most interesting and well-studied models [28]. Male zebra finches are extraordinary singers that learn to produce a highly crystallized (i.e. stereotyped and much less dependent on auditory feedback) and complex sequence of syllables during courtship [16] [47] [36] [46]. Female birds show more copulation in response to songs from male zebra finches, than to songs from different species [29]. The songs of male zebra finches can increase their reproductive success by attracting females' attention and heightening their receptivity [14]. Their courtship songs are precise and relatively insensitive to short time feedback perturbations, unlike some other species such as Bengalese finches [79] [30].

The song motor pathway consists of a motor pathway which ultimately projects to

syringeal and respiratory muscles to sing, and a basal ganglia pathway which forms a feedback loop for mediating song learning and maintenance (Figure 3.1). Both pathways originate from the telencephalic sensorimotor nucleus HVC (a proper name), which makes it an essential site for synaptic interactions important to song production [16] [33].

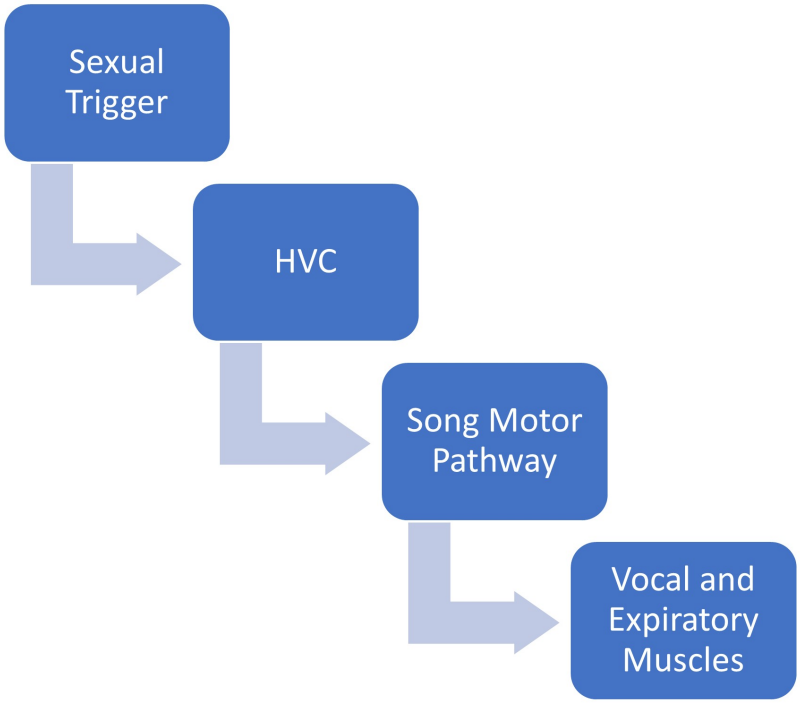

Figure 3.1. The signal pathway which enables song production in zebra finches

3.1.2 Motivation

Birdsong production is an interesting model for studying complex vocal behavior, especially for adult zebra finches when directed toward females. Their songs and human speech share similar precisely integrated vocal and respiratory muscle activity, and both vocal learning of birdsong and human speech depend on early auditory experience and feedback [16]. Moreover, birds and humans share the same basic organizational features in their auditory periphery [16]. Therefore, the modeling of the zebra finches' song system will be very helpful to understand the mechanisms behind human audition and speech. Studies of zebra finches have identified that the HVC sits at the pivotal location in the specialized forebrain pathway that ultimately controls

syringeal and respiratory muscles to produce songs. This nucleus plays a critical role in singing and song learning [36].

Numerous intracellular recordings of HVC neurons have unveiled a variety of physiological properties and circuit mechanisms within the HVC [36] [28] [46] [48], as well as the trigger input into HVC before the motif and neuron spikes during singing. There are also many HVC single neuron models focused on spike characteristics and different ion channels [37] [36] [28] [38] [49], but less work has been done to reproduce the observed interneuron interactions[32] [50] [51] [53]. Previous network models focused on generating the series of projection neuron firing patterns, but they either proposed chain models without biophysical mechanism behind the series propagation, or failed to include electrical-recording confirmed synaptic connections among various types of neurons in the network [53] [31] [32].

Here, we begin with conductance-based neuron models for two types of individual neuron in this region. Each type of neuron model consists of ion channel dynamic equations verified in the lab, and both of them reproduce the spontaneous firing behavior of their corresponding neuron types under a background input current. Next, a model microcircuit is constructed with these individual cells based on experimentally established neuron transmitter pulses [55] [56], as well as recorded bidirectional synaptic interactions between them [46]. This microcircuit exhibits the basic neuron behavior when zebra finches are silent, while it also reproduces expected voltage traces of both types of neurons after the onset of female-directed singing, which is induced by a simulated trigger input according to calcium signal from A11 cell group axons [54]. Finally, we add more projection neurons along with homotypic synaptic interactions, and demonstrate that this framework successfully reproduces the time-locked firing pattern of excitatory HVC neurons during repeated renditions of zebra finches' song.

3.1.3 Major types of neurons

Major neuron types in the HVC are (Figure 3.2):

- RA projecting neurons: project to the robustus archistriatalis nucleus (RA);

- X projecting neurons: project to area X of the lobus parolfactorius;
- Interneurons

Among those major types of neurons, HVC_{RA} neurons are those which directly control song production. Their axons innervate the nucleus RA, which gives rise to song production [16]. Two different experimental facts support this claim: First, birds with lesioned HVC or RA lose most or all syllables of their songs; Second, electrophysiological recordings prove that both HVC and RA show elevated patterned activity right before the onset of every syllable. Also, the time between the increased spikes in a given nucleus and the production of the corresponding sound was longer for HVC and shorter for RA, which is consistent with their location in the song motor pathway [14].

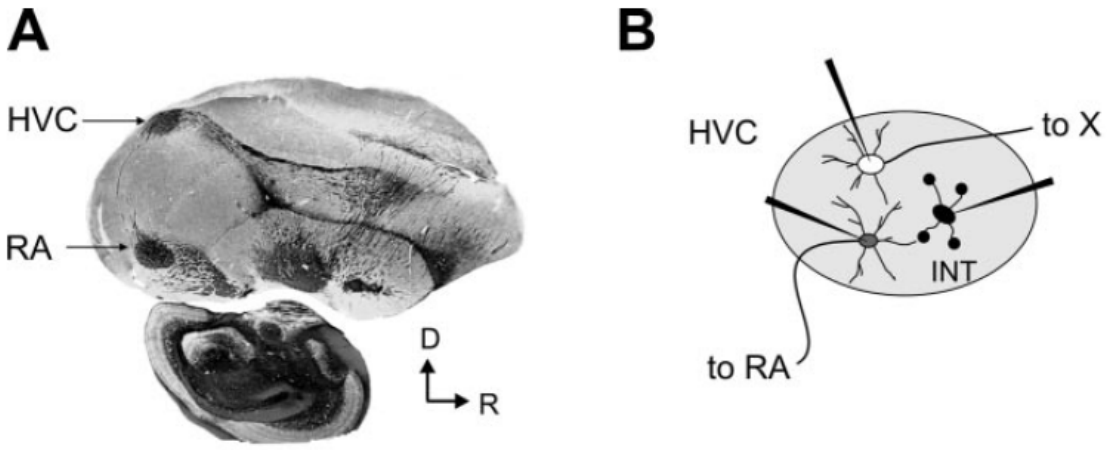

Figure 3.2. A: A sagittal section through the brain of an adult male zebra finch, stained for myelin, showing the song nucleus HVC and the song premotor nucleus RA. B: A schematic of the song nucleus HVC, showing the three neuron classes, including projection neurons that innervate RA (HVC_{RA}), projection neurons that innervate Area X (HVC_X), and interneurons. This figure is reproduced from [46].

HVC_{RA} neurons are also special because HVC and RA are important for convergence between the song motor pathway (the primary pathway for production of songs) and the anterior forebrain pathway (see Section 1.1 for details) [16]. Another interesting feature is that the nuclei in the song control system develop into a sexually dimorphic structure in adult songbirds'

brains[34] [14]. The sexual dimorphism of the song system is formed during a limited period in zebra finches' early life, and is controlled by steroid hormones. Experiments show that those steroid hormones affect the pattern of HVC_{RA} axonal projection in a sexually dimorphic fashion.

Therefore, this chapter will focus on simulating the activity and connections among HVC_{RA} projecting neurons and interneurons, since interneurons are necessary for HVC_{RA} neurons to work normally. There are many papers studying the behavior of single HVC_{RA} neuron [36] [37] [38], but little work has been done on building HVC networks based on knowledge of HVC_{RA} and interneuron properties and connection patterns [53] [32] [50] [51]. This chapter aims to create a model which describes the HVC neuron network consisting of multiple neurons and their synaptic interactions. It aims to describe the behavior of different types of neurons, how they interact with each other and jointly produce various zebra finches' songs. The nucleus HVC will be modeled as a pattern-generating network which reproduces many important observations of single neuron behavior, neuron connections and formation of syllables.

3.1.4 Neuron connections

To ensure that the neural network model matches the actual structures in zebra finches' HVC region, the first step is to learn how neurons interact with each other, regardless of whether the connections are for the same type of neurons or across different types. For the HVC_{RA} neurons and interneurons, both of them have axons extended within the HVC region, which allow them to perform local synaptic processing. We aim to include frequent (i.e., recorded multiple times [46]) connections between neuron types in the model microcircuit so that the proposed model is faithful to the observed synaptic interactions in this nucleus.

It is also well established that synaptic processing in the HVC region is frequent and important for singing behavior [57] [46]. HVC_{RA} neurons generate sparse and high-frequency spikes during singing (Figure 3.3). These action potential spikes form a sequence of burst, and the bursts propagate via local connections between HVC_{RA} neurons and are finally terminated

by inhibitory interneurons. Also, HVC neurons show highly selective action potential response during playback of BOS (bird's own song), and the temporal sparseness and sensitivity to specific syllables sequences of these responses are controlled by local neuron interactions in HVC [39] [40] [15] [42].

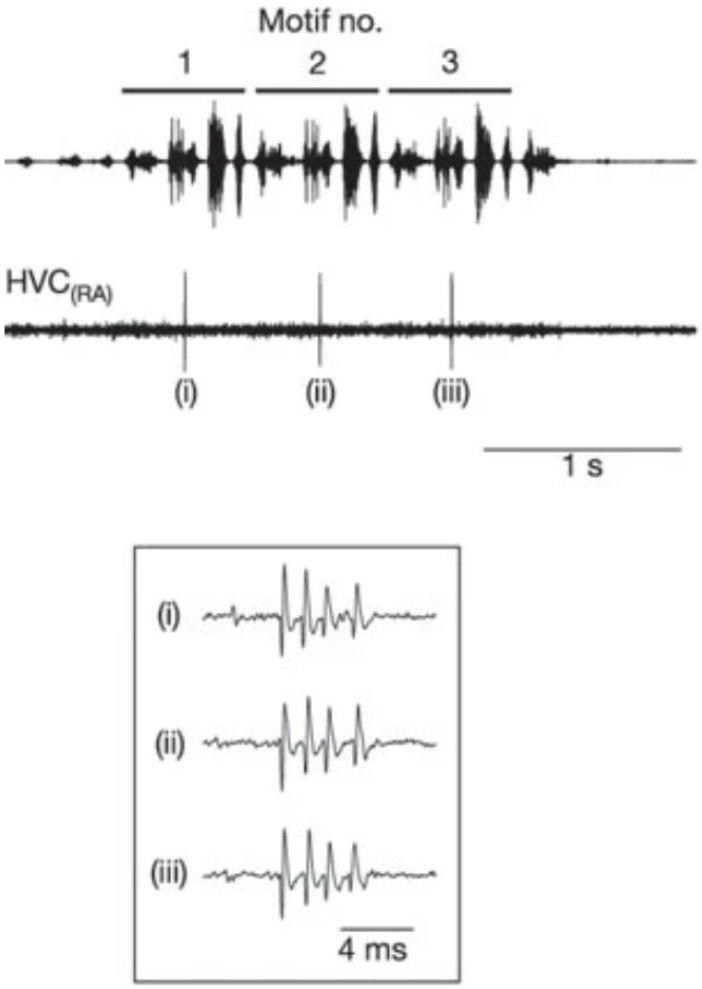

Figure 3.3. Extracellular recordings of spiking activity of identified RA neurons during singing (bottom), with the simultaneously recorded vocalization (top). The HVC_{RA} neuron generates a single burst during each of three motif renditions. This figure is reproduced from Hahnloser 2002 [57].

Since the axonal and dendritic processes from all major types of HVC neurons as well as axons from HVC afferents are interwoven with each other, it is extremely complicated to analyze

intrinsic connectivity and synaptic interactions [43] [15] [44]. However, the synaptic interactions between neuron pairs can be studied by recording intracellular voltages from pairs of identified neurons in slices of HVC and calculating spike-triggered averages (STAs) [45] [46]. By blind dual sharp microelectrode recordings from synaptically coupled pairs of neurons, one can see clearly the depolarizing or hyperpolarizing membrane voltage responses in one cell immediately after the spontaneous or stimulus-evoked spikes from the other cell in the recorded pair [46].

Compared to raw and averaged membrane voltage recordings, there are three main types of evoked responses in the post-synaptic cells: hyperpolarizing responses (IPSPs), depolarizing responses (dPSPs), and depolarizing responses which can evoke action potentials in the postsynaptic cells (EPSPs) [46].

Paired recordings between HVC_{RA} projecting neurons and interneurons indicate that HVC_{RA} axon collaterals make excitatory synaptic contacts onto interneurons. A single spike from the HVC_{RA} cells was often sufficient to evoke the interneuron to spike threshold, and spike doublets or triplets from the HVC_{RA} neuron could drive EPSPs in the interneuron. The synaptic inputs from HVC_{RA} neurons to interneurons are mostly short-latency, excitatory and strong [46].

The same experiments also provide direct evidence that interneurons have synaptic contacts on HVC_{RA} neurons. At the population level, the HVC_{RA}-interneuron coupling is robust and bidirectional, and synaptic transmission from the interneurons to HVC_{RA} neurons mostly evoke IPSPs in the HVC_{RA} neuron. HVC has reciprocally connected projecting neurons and interneurons, which is similar to the case of other pattern-generating networks [46]. Bidirectional connections between interneurons and projecting neurons can form bistable networks and generate low-frequency rhythms or no output according to the amount of excitatory input applied to the network [52].

There are also synaptic interactions between pairs of neurons of the same type. Paired recordings show that most HVC_{RA} cell pairs exhibit unidirectional EPSPs. For interneurons, only one group of interneuron pair was detected unidirectional IPSPs in 53 brain slices from 30 zebra finches[46]. Therefore, the most prevalent synaptic couplings in this nucleus are found

inside HVC_{RA}-HVC_I and HVC_{RA}-HVC_{RA} pairs (see Figure 3.4).

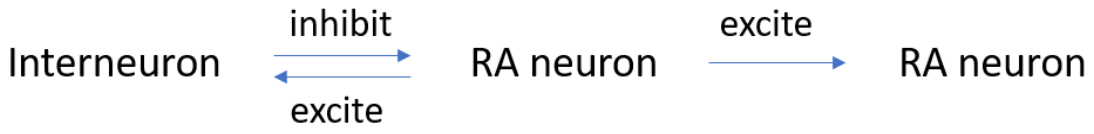

Figure 3.4. Neuron connections which are relatively prevalent within the HVC region

3.1.5 Trigger input into HVC

Male zebra finches sing towards females for courtship, and HVC activity is highly synchronized with song production. What triggers this learned courtship behavior? How does the HVC neuron network know when to start the sequence of stereotyped syllables? One idea is that a neural circuit receives and preprocesses stimulus from the environment, and conveys the information to HVC [54]. To simulate the neural network behavior during the song, which is the most interesting phenomenon in this region, we must understand how the network knows it is time to start.

The midbrain A11 cell group is a group of neurons that is implicated in motor control, motivation and reproduction [58] [59]. This group of neurons in songbirds receive sexual motivation input from the medial preoptic nucleus (POM) [60], and project axons into HVC. A11 neurons and their axons in HVC are crucial for female-directed singing. Male zebra finches with lesioned A11 cell bodies or A11 terminals in HVC failed to sing when presented with a female bird [54].

GCaMP imaging also reveals that the calcium signals in A11 terminals in HVC were elevated above the baseline before the first introductory note and peaked at motif onset [54]. For local HVC axons and some HVC cell bodies, similar experiments show that vocalization-related increase of GCaMP signals during female-directed singing was delayed compared to the activity in A11 neurons.

All these results suggest that the A11 cell group is crucial to courtship songs and its terminals in HVC is necessary for triggering female-directed singing.

3.2 Methodology

3.2.1 Single neuron

The basic units of our HVC neural network model are individual HVC_{RA} and HVC_{I} cells. HVC_{X} projecting neurons which connect with Area X and the anterior forebrain pathway (AFP) are not included since they are not directly involved in the song motor pathway [16]. The HVC_{RA} population projects to RA and then gives rise to the song motor pathway (SMP), and it plays a fundamental role in controlling syringeal motor neurons and respiratory premotor neurons in the brain stem. We also focus on the HVC_{I} neurons because the inhibitory current from the interneuron is central in modulating the projection neurons' activity [61] [53].

Our neuron model is developed from conductance-based Hodgkin-Huxley-type neurons with sodium, potassium, and leak channels (See Chapter 2.1.1 for details) [20]. In 1952, Hodgkin and Huxley proposed a gate model which describes the time dependence of both voltage and ion conductances in the squid axon. This classical model assumes that ions diffuse down towards their concentration gradients through aqueous pores formed by channel proteins on the membrane. These pores have gates which can be described by voltage-sensitive gating variables [63]. The specific HVC_{RA} projecting neuron model we use here is based on Kadakia et al. (2016), Armstrong (2016) and Toth (2011), as well as the electrophysiological recordings and simulations from Daou et al. (2013) [64] [36] [53] [37]. Among the HVC_{RA} neuron channels, sodium and potassium currents produce fast-response spikes in response to stimulating currents, and the lead current is a widely existing channel which is carried mainly by chloride and other ions. The inhibitory neuron model (HVC_{I}) is taken from Breen et al. (2016), Armstrong (2016) and Daou et al. (2013) [36] [53] [49]. Aside from the basic NaKL channels, the HVC_{I} cells are also shown to have a T-type low threshold calcium current (I_{CaT}) and a hyperpolarization activated current (I_{H}) [36] [53] [49]. The behavior of the calcium current is described by the Goldman–Hodgkin–Katz (GHK) equation to better reflect its current-voltage curve [62] [63]). Compared to the simple ohmic circuit describing the membrane potential (see Figure 2.2), the

GHK equation adds extra nonlinearity to the current [13].

The time evolution of the cross-membrane voltage of the HVC_{RA} and HVC_{I} neurons is determined by currents that flow across ion channels specific for certain types of neurons, as well as synaptic interactions and background stimulus current. All these components can be summarized in the following equations:

RA projection neuron:

$$C\frac{dV_{\mathrm{RA}}(t)}{dt} = I_{\mathrm{Na}}(t) + I_{\mathrm{K}}(t) + I_{\mathrm{L}}(t) + \sum I_{\mathrm{syn}}(t) + I_{\mathrm{background}} \tag{3.1}$$

Interneuron:

$$C\frac{dV_{\mathrm{I}}(t)}{dt} = I_{\mathrm{Na}}(t) + I_{\mathrm{K}}(t) + I_{\mathrm{L}}(t) + I_{\mathrm{CaT}}(t) + I_{\mathrm{H}}(t) + \sum I_{\mathrm{syn}}(t) + I_{\mathrm{background}} \tag{3.2}$$

Here, C is the membrane capacitance. $V_{\mathrm{RA}}(t)$ and $V_{\mathrm{I}}(t)$ are the membrane potentials of HVC_{RA} and HVC_{I} neuron respectively. A specific ion current (sodium, potassium, leak, low threshold calcium, and hyperpolarization activated current) is represented by I_{type}, i.e. I_{Na}, I_{K}, I_{L}, I_{CaT}, and I_{H}, respectively. The dynamical equations describing the NaKL channels are the same as that used in Chapter 2, while other currents are characterized by a different set of equations. The summation of the $I_{\mathrm{syn}}(t)$ terms represents all the synaptic input currents from both inside and outside the HVC region. $I_{\mathrm{background}}$ refers to the ambient background stimulus which is usually a DC current. Each ion channel current can be expressed as a function of voltage $V(t)$ and gating variables $G_i(t) = [m(t), h(t), n(t), a(t), b(t), H(t)]$ [63] [36] [37] [53]. A gating variable can be thought as the fraction of opened gates for the corresponding ion channel gates (see Section 2.1 for background). The dynamics of the ion currents can be approximated with the following equations:

$$I_{\mathrm{Na}}(t) = g_{\mathrm{Na}} m(t)^3 h(t) (E_{\mathrm{Na}} - V(t)) \tag{3.3}$$

$$I_{\mathrm{K}}(t) = g_{\mathrm{K}} n(t)^4 (E_{\mathrm{K}} - V(t)) \tag{3.4}$$

$$I_{\mathrm{L}}(t) = g_{\mathrm{L}} (E_{\mathrm{L}} - V(t)) \tag{3.5}$$

$$I_{\mathrm{CaT}}(t) = g_{\mathrm{CaT}} \cdot a(t)^3 b(t)^3 \cdot GHK(V(t), Ca(t)) \tag{3.6}$$

$$I_{\mathrm{H}}(t) = g_{\mathrm{H}} H(t)^2 (E_{\mathrm{H}} - V(t)) \tag{3.7}$$

With the definition of $GHK(V(t), Ca(t))$ written as [63]:

$$GHK(V(t)) = V(t) \cdot \left(\frac{[Ca]_{\mathrm{ext}} e^{-ZFV(t)/RT} - [Ca](t)}{1 - e^{-ZFV(t)/RT}} \right) \tag{3.8}$$

In the ion current equations, all parameters denoted as "g" are the maximum conductance of corresponding ion channels. The parameters named as "E" are the respective reversal potentials. In the GHK equation, $[Ca]_{\mathrm{ext}}$ is the constant extracellular concentration of calcium ions, and $[Ca]$ is the intracellular calcium concentration evolving with time. Z is the valence of calcium ions. F is the Faraday constant and R is the gas constant. T represents the temperature which is 298K in our case. All the gating variables $G_i(t) = [m(t), h(t), n(t), a(t), b(t), H(t)]$ obey a similar set of equations [63] [36] [37] [53]:

$$\frac{dG_i(t)}{dt} = \frac{\eta_{Gi}(V(t)) - G_i(t)}{\tau_{Gi}(V(t))} \tag{3.9}$$

$$\eta_{Gi}\left(V\left(t\right)\right)=\frac{1}{2}+\frac{1}{2}\tanh\left(\frac{V\left(t\right)-V_{Gi}}{\Delta V_{Gi}}\right) \tag{3.10}$$

$$\tau_{Gi}\left(V\left(t\right)\right)=\tau_{Gi0}+\tau_{Gi1}\left[1-\tanh^{2}\left(\frac{V\left(t\right)-V_{Gi}}{\Delta V_{Gi}}\right)\right] \tag{3.11}$$

Here, V_{Gi}, ΔV_{Gi}, τ_{Gi0} and τ_{Gi1} are parameters for their corresponding gating variable $G_i(t)$. The dynamics of $H\left(t\right)$ is the only exception here: $\eta_{\mathrm{H}}(V(t))$ and $\tau_{\mathrm{H}}\left(V\left(t\right)\right)$ use different values of ΔV_{H}. The calcium concentration is also a function of time:

$$\frac{d\left[Ca\right]\left(t\right)}{dt}=\phi I_{\mathrm{CaT}}+\frac{Ca_{0}-\left[Ca\right]\left(t\right)}{\tau_{\mathrm{Ca}}} \tag{3.12}$$

where the parameter Ca_0 is the intracellular calcium concentration during equilibrium state. ϕ and τ_{Ca} are specific parameters for calcium concentration dynamics. All the values for the $\mathrm{HVC_{RA}}$ neuron model parameters are listed in Table 3.1; numbers for the $\mathrm{HVC_{I}}$ cell can be found in Table 3.2. The parameters governing the dynamics of gating variables $\left[m\left(t\right),h\left(t\right),n\left(t\right)\right]$ obey the same group of values for both the $\mathrm{HVC_{RA}}$ neuron model and the interneuron model, which are only listed in Table 3.1.

Table 3.1. Parameter values for RA projecting neuron. Reference [37] proposed a HVC_{RA} model with a particular choice of parameter, which reproduce the neuron response with respect to pseudo-noisy dendritic currents. The RA neuron model described in this chapter is a simplified version of the one in Ref [37].

Index	Parameter	Value	Ref	Index	Parameter	Value	Ref
1	g_{Na}	1050 nS	[37]	11	V_h	-45 mV	[37]
2	E_{Na}	55 mV	[37]	12	ΔV_h	-7 mV	[37]
3	g_K	120 nS	[37]	13	τ_{h0}	0.1 ms	[37]
4	E_K	-90 mV	[37]	14	τ_{h1}	0.75 ms	[37]
5	g_L	3 nS	[37]	15	V_n	-35 mV	[37]
6	E_L	-80 mV	[37]	16	ΔV_n	10 mV	[37]
7	V_m	-30 mV	[37]	17	τ_{n0}	0.1 ms	[37]
8	ΔV_m	9.5 mV	[37]	18	τ_{n1}	0.5 ms	[37]
9	τ_{m0}	0.01 ms	[37]	19	C	10 pF	[53]
10	τ_{m1}	0 ms	[37]				

Table 3.2. Parameter values for interneuron. The parameter values for [V_m, ΔV_m, τ_{m0}, τ_{m1}, V_h, ΔV_h, τ_{h0}, τ_{h1}, V_n, ΔV_n, τ_{n0}, τ_{n1}] can be found in Table 3.1. Reference [49] estimates the parameter values using a voltage recording of a real interneuron *in vitro*.

Index	Parameter	Value	Ref	Index	Parameter	Value	Ref
1	g_{Na}	1200 nS	[53]	15	V_a	-30 mV	[49]
2	E_{Na}	55 mV	[37]	16	ΔV_a	32.9 mV	[49]
3	g_K	200 nS	[53]	17	τ_{a0}	4.44 ms	[49]
4	E_K	-90 mV	[37]	18	τ_{a1}	4.24 ms	[49]
5	g_L	3 nS	[53]	19	V_b	-62 mV	[49]
6	E_L	-80 mV	[37]	20	ΔV_b	-62.5 mV	[49]
7	g_H	2 nS	[53]	21	τ_{b0}	2.90 ms	[49]
8	E_H	-40 mV	[53]	22	τ_{b1}	7.57 ms	[49]
9	V_H	-60 mV	[53]	23	$[Ca]_{ext}$	2500 μM	[49]
10	ΔV_H for η	-10 mV	[49]	24	Ca_0	1.11 μM	[49]
11	ΔV_H for τ	-5.5 mV	[49]	25	ϕ	3.88 μM/(ms $\cdot$ pA)	[49]
12	τ_{H0}	214 ms	[49]	26	τ_{Ca}	0.143 ms	[49]
13	τ_{H1}	158 ms	[49]	27	C	10 pF	[53]
14	g_{CaT}	0.1 nS	[53]				

3.2.2 Synapses

The synaptic dynamics is built on the formalism of electrically delivered neurotransmitter pulses and opening rate of neurotransmitter acceptors, based on the data from Destexhe and Sejnowski (2001) and Destexhe et al. (1994) [55] [56]. For the releasing process of presynaptic neurotransmitters, assuming that all intervening reactions in the release process are fast and can be considered at steady state, the neurotransmitter concentration $[T]$ can be expressed as:

$$[T] = \frac{[T]_{max}}{1 + \exp\left[-\left(V_{pre} - V_p\right)/K_p\right]} \tag{3.13}$$

where $[T]_{\max}$ is the maximal concentration of neurotransmitter in the synaptic cleft. V_{pre} is the presynaptic voltage. K_{p} is the steepness and V_{p} sets the value of which the function is half activated. This is a simplified model of the neurotransmitter release process compared to a kinetic model involving calcium diffusion and gradients, which introduces a smoother transformation between presynaptic voltage and neurotransmitter concentration.

Postsynaptic neurotransmitter receptors have several different types, each with specific response to the same concentration of corresponding neurotransmitter. Previous studies have confirmed that the local axon collaterals of HVC_{RA} neurons release glutamate, and excite interneurons by activating ionotropic glutamate receptors of the α-amino-3-hydroxy-5-methyl-4-isoxazolepropionic acid (AMPA) subtype [46] [65]. For the inhibitory connections from interneurons to HVC_{RA} cells, this fast hyper-polarizing response is mediated by γ-aminobutyric acid (GABA) and GABA_{A} type receptors [46] [65]. Under the assumption that these two types of neurotransmitters both bind to the receptors at a constant rate, the postsynaptic kinetics can be described by the following set of equations:

$$\frac{dr}{dt} = \alpha_{\text{AMPA/GABA}}[T](1-r) - \beta_{\text{AMPA/GABA}} r \tag{3.14}$$

$$I_{ij} = g_{ij} r_j \left(V_j(t) - E_{\text{AMPA/GABA}}\right) \tag{3.15}$$

where r is the fraction of the postsynaptic receptors in the open state. Its dynamics depends on $\alpha_{\text{AMPA/GABA}}$, the gate opening rate, and $\beta_{\text{AMPA/GABA}}$, the gate closing rate. They take different values for AMPA and GABA_{A} type receptors. I_{ij} is the current seen by postsynaptic cell j as a result of input from presynaptic neuron i. g_{ij} is the maximal conductance and $E_{\text{AMPA/GABA}}$ is the synaptic reversal potential. $V_j(t)$ is the instantaneous membrane voltage for the postsynaptic cell. Parameter values for synaptic dynamics can be found in Table 3.3.

The value of maximal conductance g_{ij} between two neurons is obtained by two factors: the number of synapses connecting neuron i and neuron j, and the maximal conductance for a

Table 3.3. Parameter values for synaptic interactions. * means the value has been tuned. Values from reference [56] are obtained from the best fit of the synaptic kinetic equations to recorded AMPA/GABA currents.

Index	Parameter	Value	Ref	Index	Parameter	Value	Ref
1	$g_{\mathrm{A11,INT}}$	8 nS	[56] [74]	8	α_{GABA}	5 /(mM·ms)	[56]
2	$g_{\mathrm{INT,RA}}$	8 nS	[56] [74]	9	α_{AMPA}	1.1 /(mM·ms)	[56]
3	$g_{\mathrm{RA,INT}}$	7 nS	[56] [74]	10	β_{GABA}	0.18 /ms	[56]
4	$g_{\mathrm{RA,RA}}$	10 or 8.2 nS	*	11	β_{AMPA}	0.19 /ms	[56]
5	E_{GABA}	-80 mV	[56]	12	K_p	5 mV	[56]
6	E_{AMPA}	0 mV	[56]	13	V_{p}	2 mV	[56]
7	$[T]_{\mathrm{max}}$	2.84 mM	[55]				

single synapse. Previous morphological studies show that there are usually multiple synaptic connections between two connected neurons in different cortical circuits across the brain [74]. More specifically, the average number of synapses per connection is estimated to be around 10 in the barrel cortex [74]. For inhibitory interactions, estimation for the maximal conductance of a single GABAergic synapse with $\mathrm{GABA_A}$ type currents is in the range of 0.25 to 1.2 nS [70] [68]. Therefore, we take the median value of 0.8 nS, so the maximal conductance for inhibitory connections between two neurons is estimated to be around 8 nS. For excitatory synapses interactions, measurements of miniature synaptic currents and analysis estimate that the maximal conductance of AMPA-mediated is between 0.35–1.0 nS in the neocortical and hippocampus pyramidal cells [71] [72] [73]. Thus, $g_{\mathrm{RA,INT}}$, the maximal conductance from an excitatory $\mathrm{HVC_{RA}}$ neuron to the postsynaptic $\mathrm{HVC_I}$ neuron is set to 7 nS in our modelling. The only parameter we have to tweak is the maximal conductance from one $\mathrm{HVC_{RA}}$ neuron to another, i.e. $g_{\mathrm{RA,RA}}$. This synaptic connection strength for homotypic $\mathrm{HVC_{RA}}$ cell pairs is set to a larger value to ensure the excitatory input is large enough to awaken the postsynaptic $\mathrm{HVC_{RA}}$ neuron. There will be more discussion about this fine-tuned parameter value in the results section 3.3.

3.2.3 Trigger signal

When male zebra finches sing towards females for courtship, HVC activity is highly synchronized with song production. As the environmental stimulus occurs, a neural circuit receives and preprocesses the external information, then triggers the HVC neuron network to start the sequence of stereotyped syllables. A11 cells are the last stop that convey this trigger signal to HVC (see Section 3.1 for details) [54]. We sought to simulate the environmental change induced by A11 signals, and explore the behavior of HVC neurons when exposed to this environment.

During *in vivo* experiment, fiber photometry reveals that the GCaMP signal of A11 axons in HVC first rapidly increase during the introductory notes, reach the peak point at the motif onset and then decrease at an almost constant speed (Figure 3.5). By assuming that the neurotransmitter concentration in the synaptic cleft in the HVC region is proportional to the measured calcium signal, we can approximate the dynamics of neurotransmitter concentration from A11 axons with the following equations:

$$[T](t) = [T]_{\min} \, (t < 0) \tag{3.16}$$

$$[T](t) = [T]_{\min} e^{t/\tau_{\mathrm{r}}} \quad (0 < t < t_{\max}) \tag{3.17}$$

$$[T](t) = T_{\max} e^{-t/\tau_{\mathrm{f}}} + [T]_{\min} \quad (t > t_{\max}) \tag{3.18}$$

Again, $[T](t)$ is the neurotransmitter concentration as a function of time. $[T]_{\min}$ represents the baseline concentration, i.e. $[T]$ before the trigger signal arrives. τ_{r} and τ_{f} are the time constants which determine the rate of rise and fall for neurotransmitter respectively. $t_{\max}$ means the time point when the concentration transits from rise to fall. For $T_{\max}$, it is a constant chosen to ensure the continuity of neurotransmitter concentration at time $t_{\max}$. Therefore, the value of $T_{\max}$ is entirely determined by other parameters:

$$T_{\max} = [T]_{\min}\left(e^{t_{\max}/\tau_r} - 1\right) \times e^{t_{\max}/\tau_f} \tag{3.19}$$

Assuming that the maximum neurotransmitter concentration is $[T]_{\max}$, the value of the transition time can be derived from equations 3.16-3.19, shown by the following equation:

$$t_{\max} = log\left(\frac{[T]_{max}}{[T]_{\min}}\right) \times \tau_r \tag{3.20}$$

The values of all parameters related to the A11 neurotransmitter dynamics are listed in Table 3.4. The time course of the trigger signal neurotransmitter concentration is displayed in Figure 3.5. We chose $[T]_{\max}$ to be 2.84 mM, a value which corresponds to the observation of maximal transmitter concentration in Destexhe 1994 [55]. $[T]_{\min}$ was chosen to be positive so that the value of $[T](t)$ in Eq (3.17) was not constantly zero, and it was set to a small value so that the A11 stimulus did not affect HVC neuron network outside the motif onset period. Other than these two restrictions, the exact value of $[T]_{\min}$ does not make a big difference to the modelling result (see Section 3.3.5 for more details about this parameter). The rise and fall timescales for the recorded GCaMP signal are up to 1 second, but we do not use this to determine the values of τ_r or τ_f. The reason is that GCaMP recordings have a large time lag compared to real neuron activities, whose value could be up to a few seconds [66]. The fall time constant is set to 1.2 ms, same as the measured decay time course of free neurotransmitters in the cleft of cultured hippocampal synapses [67], and the rise time constant is chosen to match it so that the trajectory of neurotransmitter concentration is symmetric. Based on the above choices of parameter values, the combined time span of rise and fall is approximately 5 ms (see Figure 3.5).

Table 3.4. Parameter values for triggering. * means the value has been tuned. See text for details.

Index	Parameter	Value	Ref	Index	Parameter	Value	Ref
1	$[T]_{\min}$	0.001 mM	*	3	τ_r	1.2 ms	[67] [54]
2	$[T]_{\max}$	2.84 mM	[55]	4	τ_f	1.2 ms	[67]

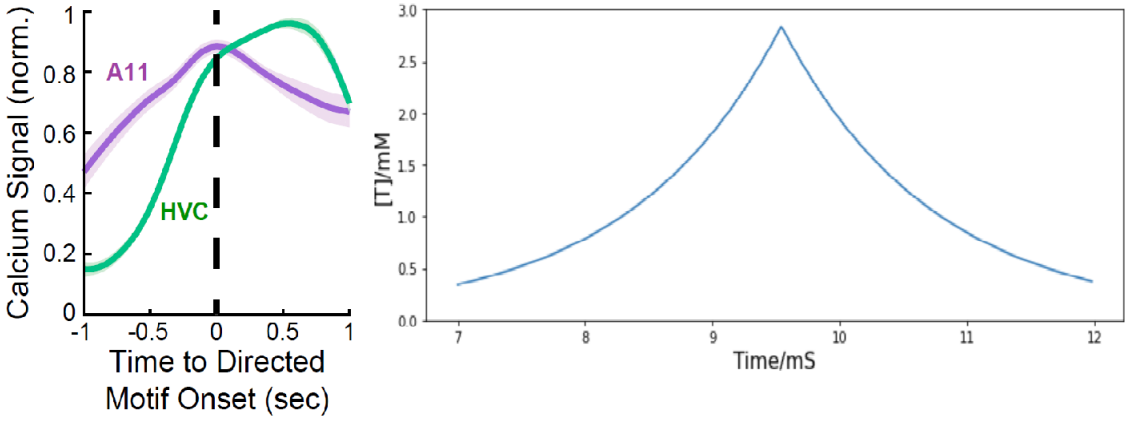

Figure 3.5. The time course of A11 axons activity in the HVC region. Left panel: Mean normalized calcium activity during female directed song motifs recorded from HVC. A black dashed line denotes the motif onset [54]. Right panel: Simulated trajectory of injected neurotransmitter concentration [T] from A11 axons to HVC. The shape of the simulated trajectory of [T] is similar to that from the GCaMP recordings, but the timescale is determined to match the measured time course of neurotransmitter in the synaptic cleft since GCaMP signal has a large time lag. The top panel is reproduced from [54]

3.3 Results

This results section illustrates, via the time course of cross-membrane voltages of two types of neurons, how they function dynamically, coordinate within the network, and respond to external stimulus. For all the voltage and current time series shown in this paper, the dynamical equations were written in Python 3, and the results were integrated with Python's adaptive fourth order Runge-Kutta "odeINT" using a step size of 0.02 ms. A smaller step size does not lead to different results.

3.3.1 Single neuron behavior

With the published set of parameters shown in Table 3.1 and 3.2, the two models reproduce qualitative features of HVC_{RA} and HVC_{I} neurons discovered during experiments. For the interneurons, the most conspicuous feature is the stereotyped firing they displayed during *in vitro* experiments [36] [49]. Figure 3.6 confirms this property by showing that the spikes of

our interneuron model under an injected current of 140 pA. For the excitatory neurons, although the zebra finches' singing behavior is synchronized with a sequence of bursts from multiple HVC_{RA} neurons, those projecting neurons will no longer fire once per song, but rather multiple times without inhibitory neurons [61]. Without inhibition input from any HVC_I neurons, HVC_{RA} cells can fire with a background stimulus above the threshold of about 100 pA. Our simulations reproduce this behavior with a threshold of about 140 pA. Figure 3.6 shows the membrane voltage of one HVC_{RA} neuron given an injected current of this threshold stimulus.

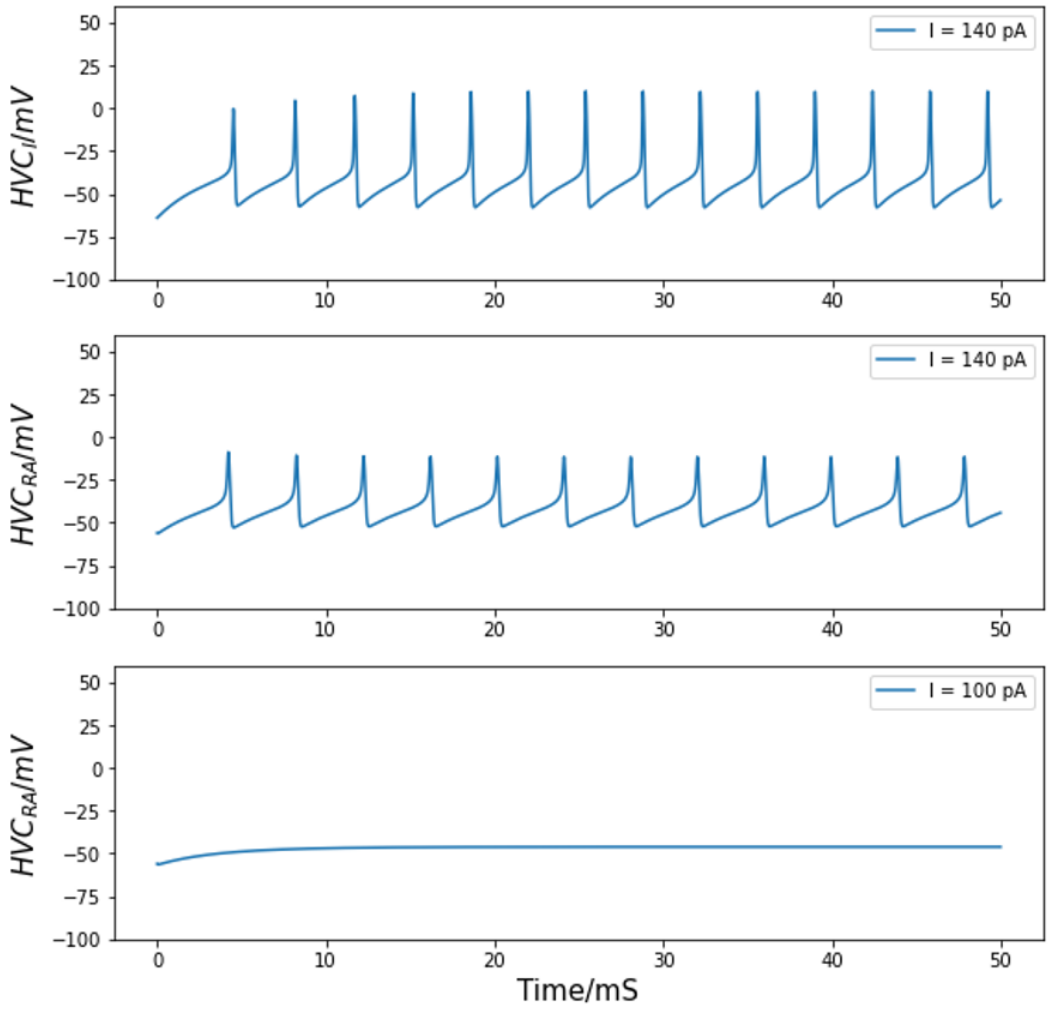

Figure 3.6. Voltage traces of HVC neurons. Top panel: voltage of an HVC interneuron neuron in response to a background current. Middle panel: an HVC_{RA} neuron exhibits action potentials given a threshold stimulus of about 140 pA. Bottom panel: the HVC_{RA} model stays silent under a lower background current of 100 pA.

3.3.2 Trigger signal into HVC

As described in Section 3.2.3, the A11 cell group transmits sexual information to HVC about female-directed calls and songs. The activity of A11 terminals in HVC starts to increase above the baseline before the first syllable as shown in Figure 3.5, which is considered to be the trigger signal about the generation of the song motif [54].

To simulate HVC neuron activities after the trigger signal arrives, we first expose an interneuron to the injection of neurotransmitters. We choose interneuron instead of HVC_{RA} neuron because those projecting neurons fail to fire at a particular temporal location during each motif without the presence of HVC_I cells. Therefore, there is a high probability that the interneurons receive the signal from A11 group and then coordinate the behavior of HVC_{RA} neurons.

Normal and uninterrupted singing consists of a constant number of syllables, which are separated by gaps formed by inhalations. Both the syllables and the gaps occur in a fixed chronological order, and they are precisely timed during repeated rendition of the same motif. During this process, a single HVC_I neuron's recording shows relatively continually spikes throughout the song with intermittent gaps. However, each HVC_{RA} neuron is observed to only fire once during a single motif (see Section 3.3.3 for details). Together with the fact that the A11 neurons synthesize and presumably release dopamine into HVC, we can take the input from A11 axons to interneurons to be inhibitory, which stop HVC_I neurons from continually firing. Following the post synaptic current equations, the inhibitory current corresponding to A11 neurotransmitter and the response of a single HVC_Ineuron are depicted in Figure 3.7. The trigger signal is not present until 10 ms so that the interneuron voltages before and after the motif onset are both revealed.

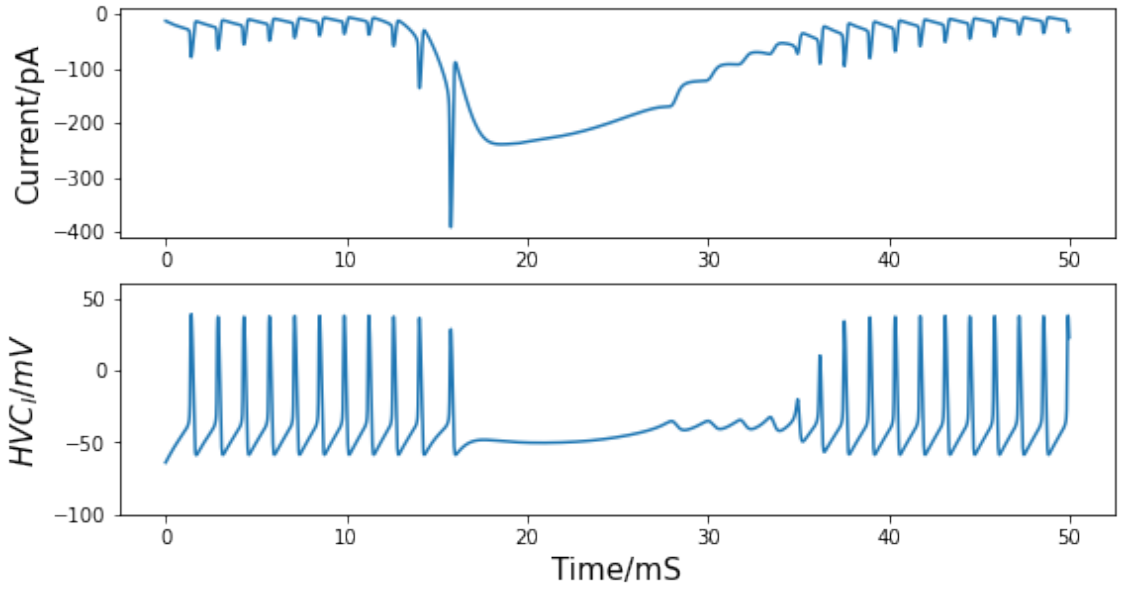

Figure 3.7. HVC_I neuron response to the trigger current. The trigger signal happens at 10 ms. Top panel: inhibitory current from A11 cell axons to interneuron corresponding to the neurotransmitter concentration path of Figure 3.5 and the post-synaptic current equation (3.15). Bottom panel: membrane voltage of the interneuron. The continuous firing of HVC_I neurons is interrupted by the inhibition input arising from 10 ms, corresponding to the intermittent silence throughout singing.

3.3.3 Interactions between HVC_I and HVC_{RA} neurons

By blind dual sharp microelectrode recordings from synaptical coupled pairs of an HVC_I and an HVC_{RA} neuron, HVC_{RA} axon collaterals often show short-latency, excitatory and strong synaptic contacts onto interneurons [46]. A single spike from the HVC_{RA} cells is often sufficient to evoke the HVC_I neuron to spike threshold, and spike doublets or triplets from the HVC_{RA} neuron could drive depolarizing responses which can evoke action potentials (EPSPs) in the interneuron [46]. Recordings in the same pairs also provide direct evidence that interneurons have synaptic contacts on HVC_{RA} neurons. At the population level, the HVC_{RA} - HVC_I coupling is robust and bidirectional, and synaptic transmission from the interneurons to HVC_{RA} neurons mostly evoke hyperpolarizing responses (IPSPs) in the latter ones (See Figure 3.9) [46]. Bidirectional connections between interneurons and projecting neurons can form bistable networks and generate low-frequency rhythms or no output according to the amount of

excitatory input applied to the network [52].

First, we permit one interneuron model to form inhibitory synapses directly to an HVC_{RA} neuron model. There is no evidence of reciprocal connections from HVC back to A11 cell group, so we only consider the inhibition from A11 axons to HVC_I cells. When the trigger input has not arrived and an awake zebra finch is not singing, the population of interneurons stays active continually while the HVC_{RA} neurons only stay silent [69]. With the synaptic model described in Section 3.2.2, the inhibitory current from HVC_I neuron is strong enough to overcome the background stimulus of 300 pA [53], and silence the HVC_{RA} neuron during the interneuron's active time (see Figure 3.8 first 10 ms).

In Figure 3.8, the simulated interneuron stops firing after the A11 inhibitory current emerges, which enable the HVC_{RA} neuron to generate a burst of spikes. Here, a burst refers to a series of action potentials which last a very brief time. However, recordings of the HVC_{RA} neuron voltages during singing reveal that a burst usually consists of around 4 spikes and lasts approximately 6 ms [57], while the modelled number of spikes and burst duration is almost doubled.

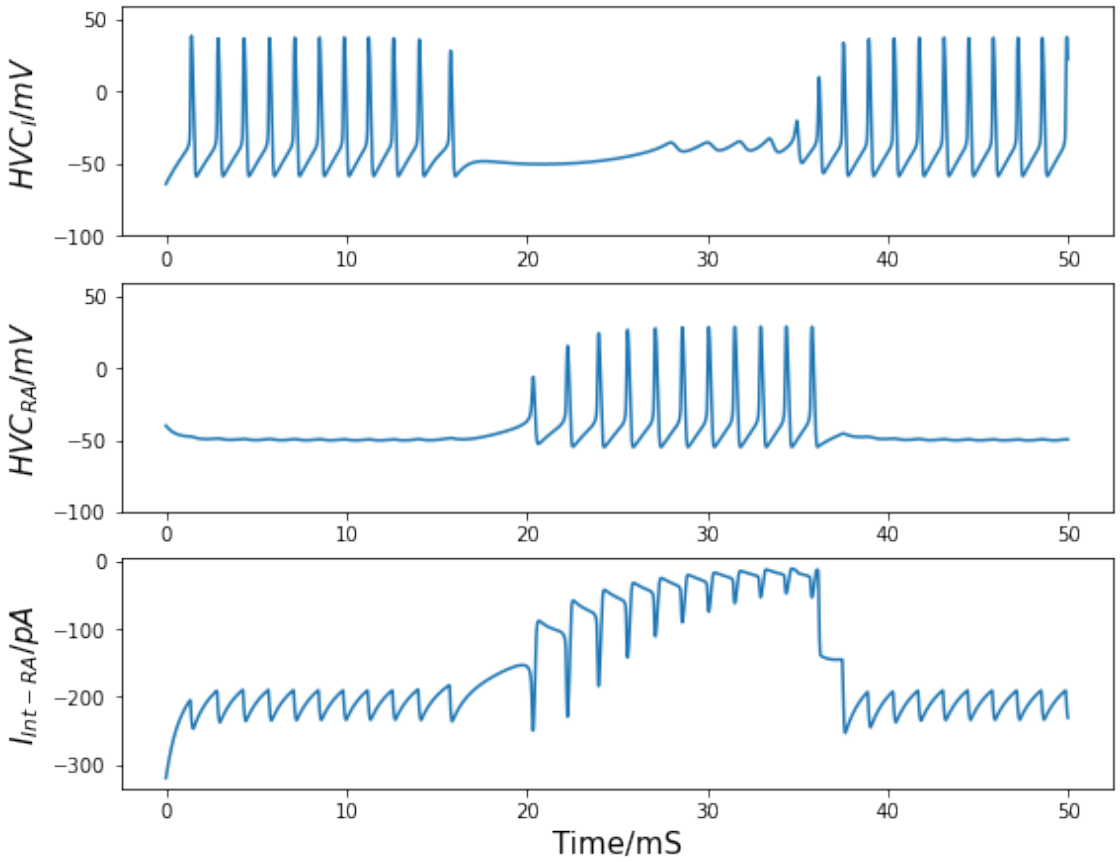

Figure 3.8. Inhibitory synaptic interactions from HVC_I to HVC_{RA} neuron and their voltage traces. Top: continuous firing of the interneuron and the quiet time induced by trigger current (presented in Figure 3.7). Center: membrane voltage of the HVC_{RA} neuron with a burst when the interneuron is not active. Bottom: inhibitory current from HVC_I to HVC_{RA} cell (Int represents the interneuron, and RA refers to the HVC_{RA} neuron.) See text for important details.

Second, if the reciprocal excitatory current from the HVC_{RA} neuron to the interneuron is added to the model, the simulated burst behavior better matches the recorded burst pattern of real HVC_{RA} neurons, as illustrated in Figure 3.9. After the trigger signal appears, the interneuron becomes silent and the inhibition from HVC_I to HVC_{RA} cell disappears, which in turn allows the HVC_{RA} neuron to start its burst. Then, the excitation current generated by the spikes from HVC_{RA} neuron successfully induces the silent interneuron to its action potential before the inhibition current from A11 axons vanishes completely. As the HVC_I generates continuous spikes again, the reciprocal synaptic interaction from the spikes of the interneuron prohibits the

HVC_{RA} cell from firing. Now the burst duration and the spike number of the HVC_{RA} neuron closely match the *in vivo* neuron observation. Therefore, the microcircuit model demonstrates that the synaptic interactions of both directions between the interneuron and the HVC_{RA} neuron is necessary for them to function as expected.

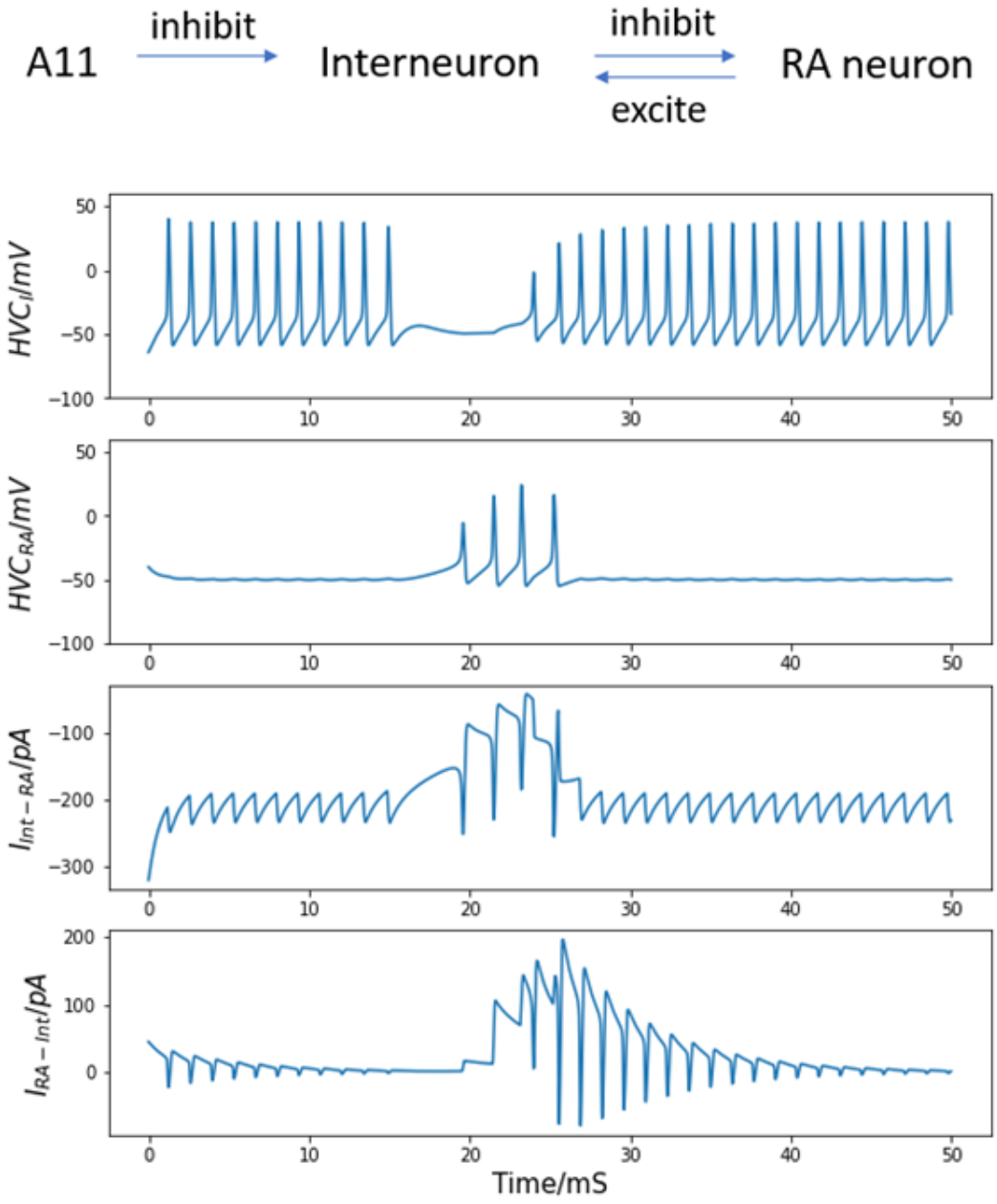

Figure 3.9. Bidirectional synaptic interactions between an HVC_I - HVC_{RA} neuron pair and their voltage traces. Top: synaptic connections among A11 cell group, interneuron and HVC_{RA} neuron. Top center: continuous firing of the interneuron and the quiet time induced by trigger current. Center: membrane voltage of the HVC_{RA} neuron with a single burst. Bottom center: inhibitory current from HVC_I to HVC_{RA} cell (Int represents the interneuron, and RA refers to the HVC_{RA} neuron.) Bottom: excitation connection from HVC_{RA} back to the interneuron. See text for important details.

3.3.4 Building syllables

We now demonstrate how to introduce multiple excitatory neurons to build a complete syllable. A first syllable from the highly stereotyped song motif from the zebra finch is used as an example, and the recorded qualitative behavior of projection neuron populations in HVC during the syllable is reproduced in this process.

A full motif contains a fixed number of syllables in its invariant pitches. Although repeated observation of zebra finches confirms that each HVC_{RA} neuron usually generates a single burst at a fixed location of one syllable during each song, multiple HVC_{RA} neurons are observed to fire successively. During normal singing, this firing order is fixed, and the time between bursts of two HVC_{RA} cells are also relatively stable. This phenomenon is presented in the experimental raster plot by Hahnloser et al. (2002) in Figure 3.10, which is compared to our modeling neural network in Figure 3.12.

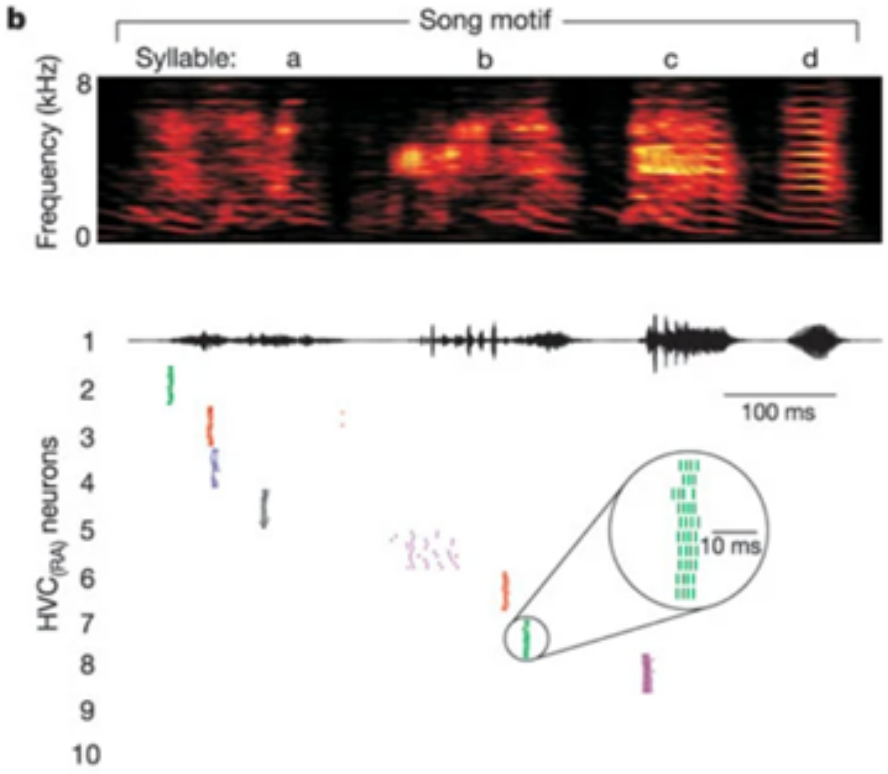

Figure 3.10. A raster plot of spike times of HVC_{RA} during repeated renditions of the zebra finch motif. Reproduced from [57]. Readers may find it of interest to compare these spiking times to the voltage plots in Figure 3.12

This chain-like propagation of spikes among various HVC_{RA} neurons can be explained by direct connections between pairs of excitatory neurons (Figure 3.11). Alternatively, a propagation of silent periods among a sequence of interneurons could occur first, and then the silent time in each interneuron may allow a corresponding HVC_{RA} neuron to burst. The prior mechanism is of higher probability since (1) it agrees with the observed high ratio (about 8:1) of HVC_{RA} to interneuron populations in the nucleus [53], (2) paired recordings show that most HVC_{RA} cell pairs exhibit unidirectional EPSPs, but few homotypic synaptic interactions are observed among interneurons [46].

In this network, the first excitatory neuron follows the same HVC_I - HVC_{RA} neuron interaction and the voltage trace in Figure 3.9, and passes that burst to the second HVC_{RA} neuron by homotypic excitation current, and so on (Figure 3.11). All the HVC_{RA} neurons except for

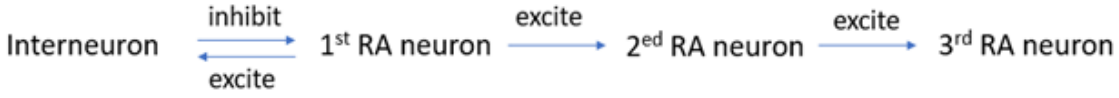

Figure 3.11. Network architecture enables production of syllables.

the very first one stay below their action potential most of the time considering the general inhibitory effect from the HVC_I and HVC_X projecting neuron populations. Simulating the potential inhibition current from each individual neuron is beyond the scope of this chapter, but we account for this phenomenon by lowering the background stimulation to 50 pA, which is known to allow those excitatory neurons to stay silent during *in vitro* experiments [36]. The average maximal conductance of excitatory synaptic currents between two neurons is estimated to be around 7 nS, as stated in Section 3.2.2. However, if the synaptic connection strength for homotypic HVC_{RA} cell pairs is set to 7 nS, the excitatory input would not be large enough to awake an HVC_{RA} neuron (see Section 3.3.5 for further discussions about tuning the parameter values). Therefore, the synaptic connection strength for homotypic HVC_{RA} cell pairs is set to 8.2 nS to ensure that the post-synaptic neuron will copy the burst pattern of the pre-synaptic neuron. The only exception happens at the first HVC_{RA} cell which is directly impacted by the trigger signal. The spikes in its one-time burst are relatively weak, so the value of $g_{RA,RA}$ for the first and second neuron is tuned to 10 nS so that the second HVC_{RA} neuron can generate the same number of spikes.

Figure 3.12 shows the simulated cross-membrane voltages of the sequentially connected excitatory neuron network given the neurotransmitter trigger signal depicted in Figure 3.5. The firing timing of neuron No.2, No.25, No.26, and No.50 matches the repeated electrode recordings of neuron 2-5 in the plot of Hahnloser et al. (2002) (Figure 3.10). During the first syllable, each HVC_{RA} cell generates a short burst consisting of four spikes. The time span of a single burst is on the order of 10 ms, and the short ($\sim$3 ms) or long ($\sim$50 ms) time intervals between spikes from different neurons are also reproduced in Figure 3.12.

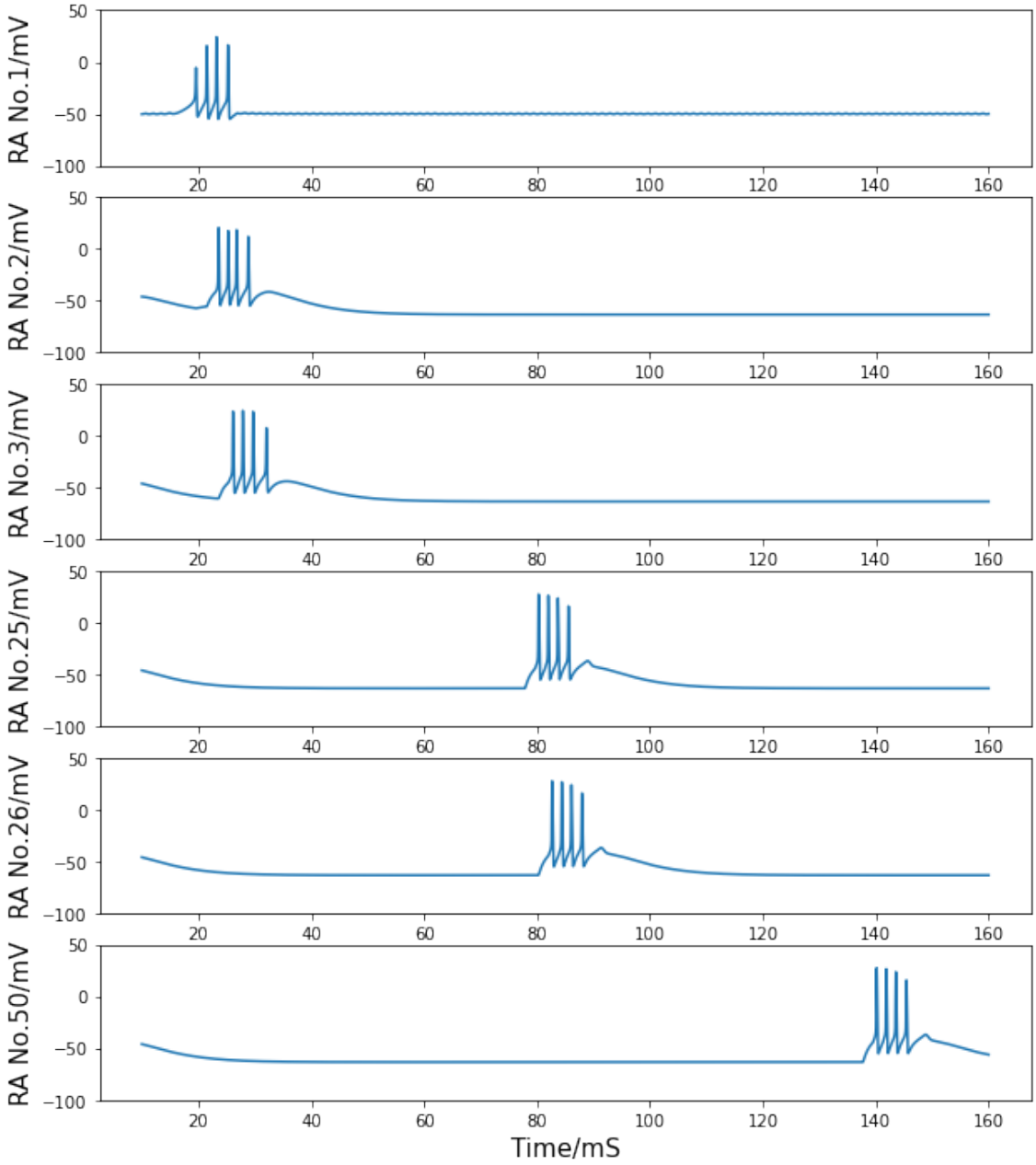

Figure 3.12. Simulated voltage plots of multiple HVC_{RA} neurons during singing. The first neuron follows the same activity as the HVC_{RA} cell in Figure 3.9, while this figure shows a time course of 10 – 160 ms. Given the trigger signal, HVC_{RA} neuron No.2, No.25, No.26, and No.50 reproduce the measured raster plots of neuron 2-5 from Figure 3.10.

3.3.5 Model robustness

In our numerical simulations, most parameter values are obtained from the published literature, with two exceptions: $[T]_{\text{min}}$ and $g_{\text{RA,RA}}$. There is no convincing analysis of the baseline

concentration of neurotransmitters before the onset of a trigger signal, so we choose the $[T]_{\min}$ value to be 0.001 mM, which is much smaller than the maximum neurotransmitter concentration $[T]_{\max}$. Fortunately, varying the value of the minimum neurotransmitter concentration does not change the simulation result as long as it stays positive and small compared to $[T]_{\max}$. In Figure 3.13, even if the value of $[T]_{\max}$ increases/decreased by ten times, the magnitude, duration and shape of neurotransmitter dynamics stays almost the same. The only difference that is introduced by the $[T]_{\min}$ value is the peak time of the neurotransmitter concentration from A11 axons, which has no impact on any simulation conclusions in Section 3.3 since this chapter does not focus on the exact onset time of the trigger current.

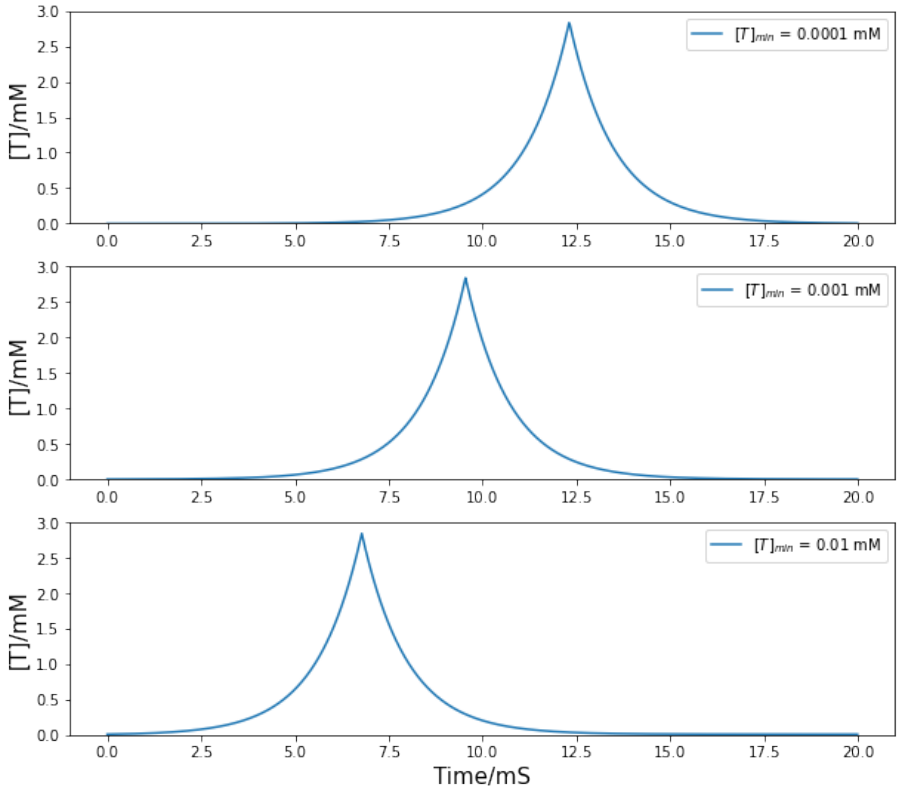

Figure 3.13. Simulated trajectory of neurotransmitter concentration in the cleft between A11 axons and HVC neurons under different choices of $[T]_{\min}$ value.

As stated in Section 3.3.4, the value of maximum conductance for connecting the chain of HVC_{RA} neurons is chosen to be 8.2 nS or 10 nS for the first pair of HVC_{RA} neurons, which

allows the post-synaptic cell to reproduce the burst duration and spike number of the pre-synaptic neuron. As discussed in Section 3.2.2, the maximal conductance of AMPA-mediated current for a single synaptic connection is measured between 0.35–1.0 nS, and there are approximately 10 synapses between a pair of connected neurons. Therefore, a reasonable value of maximum conductance should be in the range of 3.5-10 nS, which includes our proposed parameter value. Furthermore, the pre-synaptic HVC_{RA} neuron will still pass its firing pattern to the post-synaptic cell if this maximum conductance varies a small portion. When the first HVC_{RA} neuron is the pre-synaptic cell, $g_{RA,RA}$ is tuned to a larger value compared to other interactions since its first burst spike is weaker than full firing. As long as $g_{RA,RA}$ stays within the range of 9.9-10.3 nS, the second HVC_{RA} neuron will still generate four full spikes. Otherwise, the post-synaptic neuron burst will not reach four full firings if the maximum conductance is too small, or there will be a fifth miniature peak if the value is too large (See Figure 3.14). We select 10 nS as the modeling parameter value because it is within the reasonable value of measured maximum conductance between two neurons.

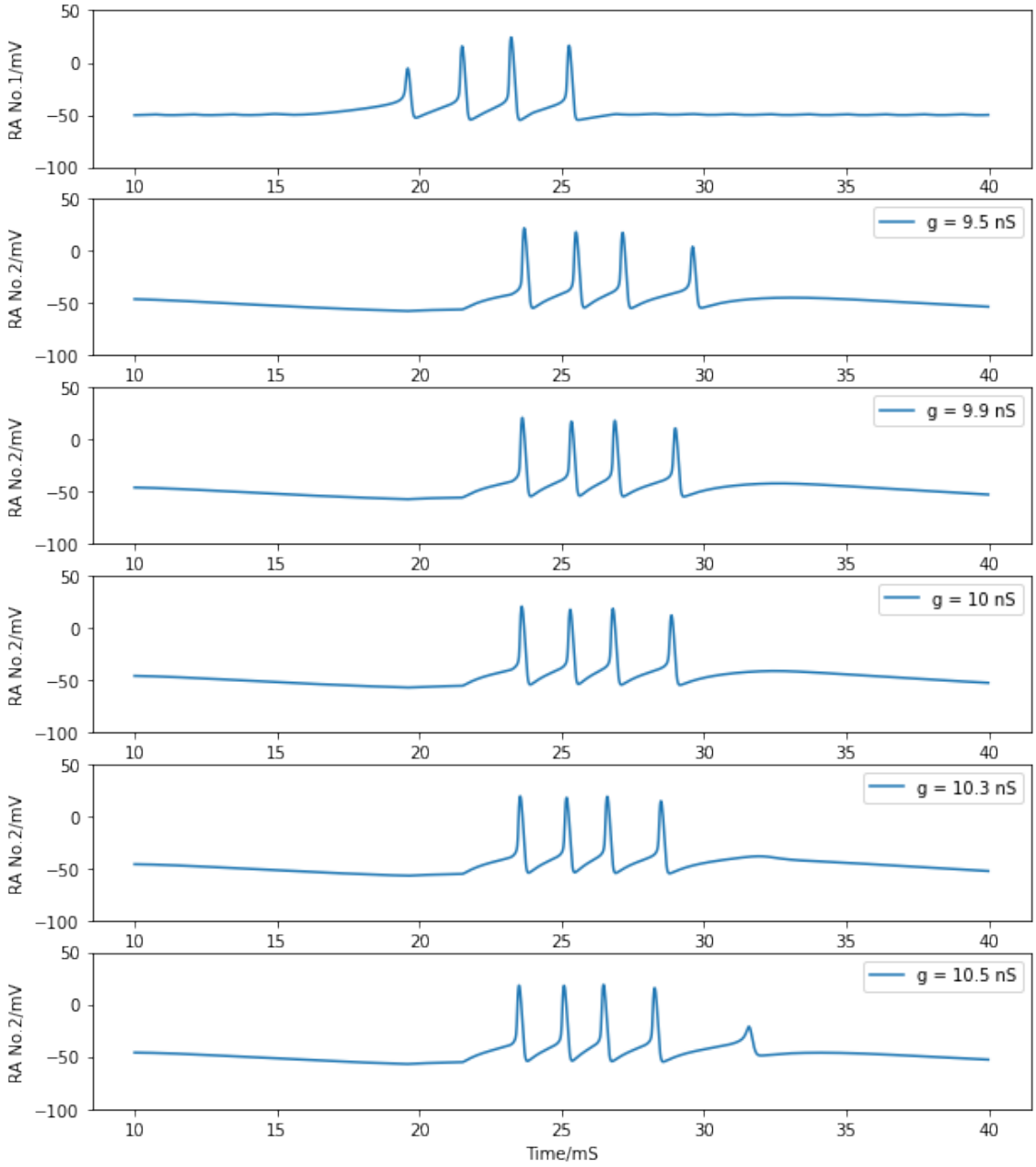

Figure 3.14. Simulated voltage plots the first HVC_{RA} neuron and the second HVC_{RA} neuron with different values of maximum conductance for the synaptic interaction between them.

In the chain of HVC_{RA} neurons after the first pair, the maximum conductance is set to 8.2 nS to ensure that the burst of four spikes can be spread by the unidirectional connections. If the value of $g_{RA,RA}$ is smaller than 8.18 nS, the burst will gradually disappear during this long transfer process (Figure 3.15); if it is larger than 8.27 nS, the burst spike number will increase as

more neurons are added to this sequence of HVC_{RA} neurons (Figure 3.16). The selected value of 8.2 nS for the maximum conductance in the sequence of HVC_{RA} neurons is reasonably close to the measured mean value of maximum conductance for excitatory currents, which is 7 nS.

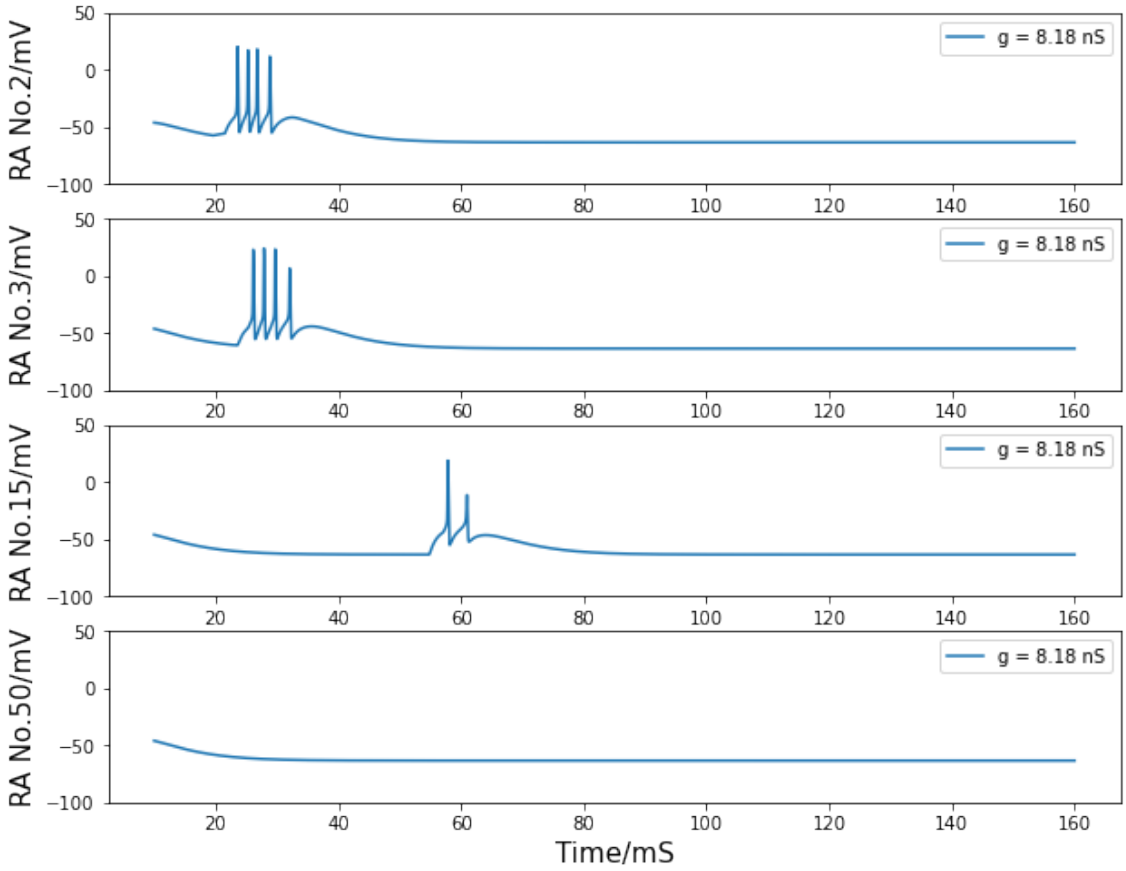

Figure 3.15. Simulated voltage plots of multiple HVC_{RA} neurons during singing with $g_{RA,RA} = 8.18nS$. For the first several neurons, the post-synaptic cell is able to copy the burst behavior of the pre-synaptic neuron, but this one-time burst gradually disappears as it is passed through more synaptic connections.

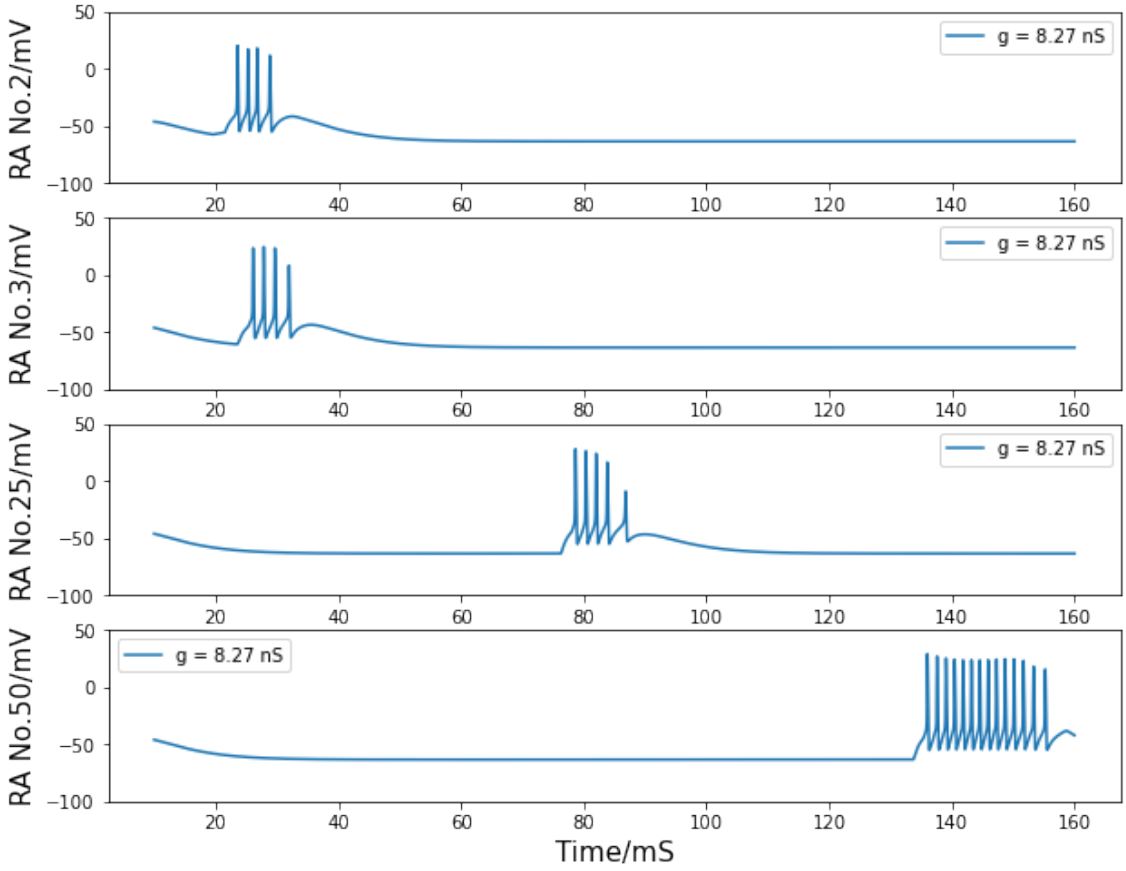

Figure 3.16. Simulated voltage plots of multiple HVC_{RA} neurons during singing with $g_{\text{RA,RA}} = 8.27nS$. For the first several neurons, the post-synaptic cell is able to copy the burst behavior of the pre-synaptic neuron, but more spikes are added to the burst because of the strong synaptic interaction strength.

However, if we only care about one pair of HVC_{RA} neurons, the voltage trace of the post-synaptic cell will still be very similar to the pre-synaptic one when $g_{\text{RA,RA}}$ stays in the range of 8.1-8.3 nS. Moreover, if the maximum conductance value of each HVC_{RA}-HVC_{RA} neuron pair is distributed uniformly between 8.1 nS and 8.3 nS, the neuron behavior and model conclusion from Section 3.3.4 will not be changed (see Figure 3.17).

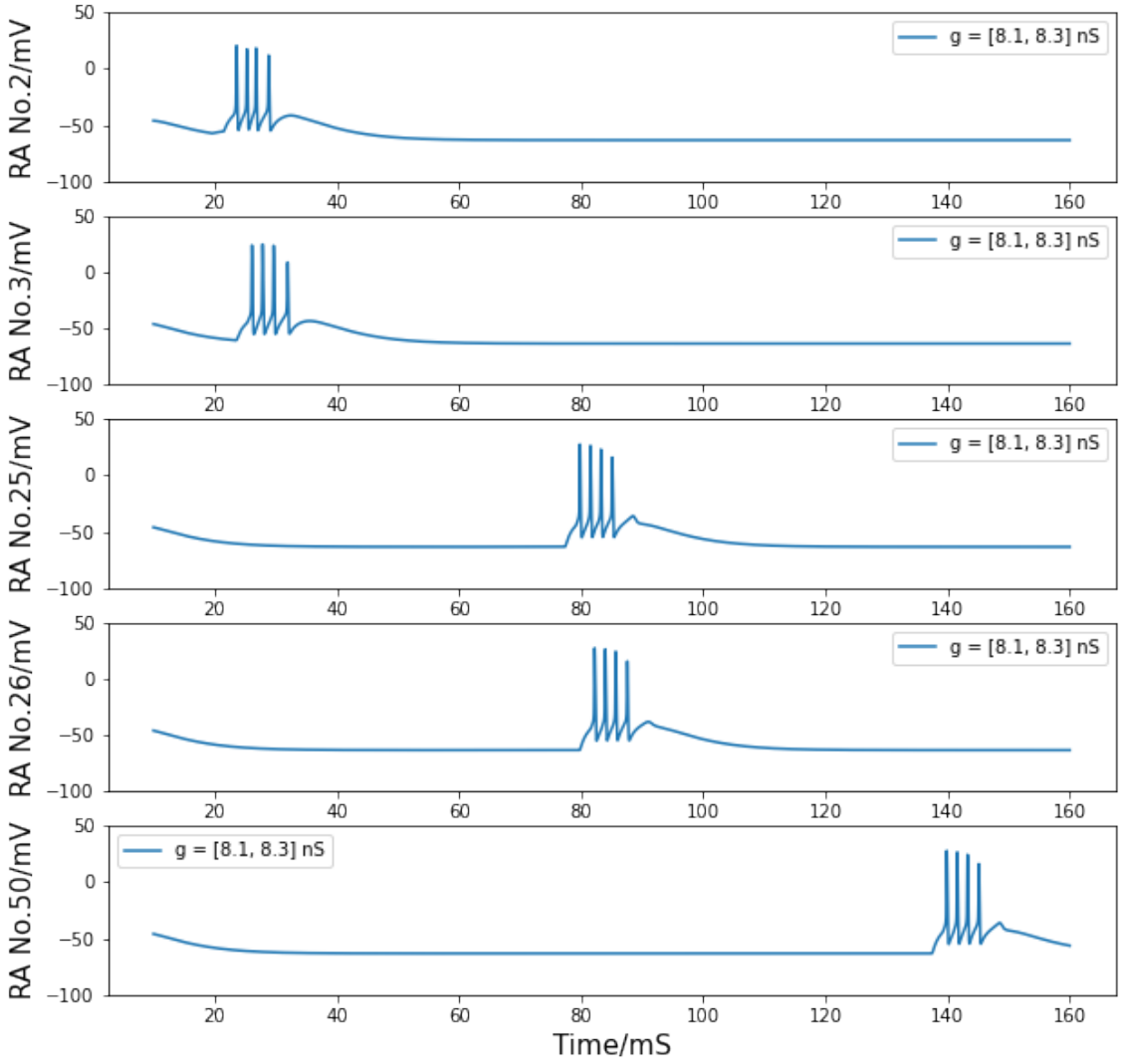

Figure 3.17. Simulated voltage plots of multiple HVC_{RA} neurons during singing as the value of $g_{RA,RA}$ for each synaptic interaction is evenly distributed in the range of 8.1-8.3 nS. The firing patterns of all neurons are similar to Figure 3.12 from Section 3.3.4.

3.4 Discussion

In this chapter on HVC microcircuits, we described single neuron models of HVC_I and HVC_{RA} neurons in the HVC nucleus, as well as synaptic current models and how to simulate the trigger signal for female-directed singing. All parts of the HVC microcircuit model are supported by experimental evidence. The modelled neuron network reproduces the main types of phenomena in this area: (1) intrinsic firing from independent HVC_I and HVC_{RA} neurons under

background current, (2) interneuron and HVC_{RA} neuron behavior during quiet time of zebra finches, (3) continuous firing from interneuron with intermittent silences during singing, (4). spike quantity and length of a burst generated by HVC_{RA} neuron induced by the trigger current, (5). time-locked sequential burst from multiple HVC_{RA} neurons during a syllable.

Our model focuses exclusively on the HVC_{RA} projecting neurons as well as interneurons which serve as an important coordination. This network does not include any HVC_X projecting neurons, a third major type of neurons in this region. HVC_X neurons projects onto area X, which in turn give rise to the anterior forebrain pathway [16]. The synaptic connections from HVC_X to HVC_{RA} neurons were detected but relatively less frequently than the coupling from HVC_I to HVC_{RA} neurons. Moreover, the chance that the spike-evoked responses from HVC_X to HVC_{RA} cells are hyperpolarizing or depolarizing are approximately the same [16]. Therefore, the role of HVC_X neurons in coordinating HVC_{RA} neuron behavior may be not as critical as interneurons, and we cannot address the detailed network structures involving all three major populations of neurons, resulting in the requirement for further observations and studies.

We expose the network to an injection of neurotransmitter induced by a male zebra finch's need to attract a female, and the injected neurotransmitters start the first syllable of a motif. Here we further examine the plausibility of generating a complete song following similar neuromodulator mechanisms. Each bird's whole song comprises a mean of 12 harmonic syllables of $\sim$80–200 ms each in duration [75] [76]. Within our framework, the full motif could be explained by a chain-like propagation linking HVC_{RA} to HVC_{RA} neurons, similar to how to construct the first syllable. Since HVC is responsible for temporal order rather than sound of syllables [77] [78], we do not worry about how to generate acoustic features for different syllables.

An alternative scenario would be that the active series of syllables is achieved by sequentially arrived neuromodulator from A11 axons. Even though the excitatory synaptic connections between HVC_{RA} neurons simulate the distributed bursts inside one syllable, it is possible that each syllable represents a relatively independent structure in the nucleus. During experiments

of singing interruption, individual syllables are more robust than the full song: direct electrical interference is necessary to interrupt a syllable, but noninvasive techniques are enough for song interruption (Eve 2016). This evidence suggests that the connectivity among syllables may follow a different mechanism from the direct synaptic interactions. We speculate that a neural feedback loop involving other nucleus may activate a succession release of neurotransmitter, which triggers multiple syllables to play a whole motif.

Another alternative to achieve a full song would be that the neurotransmitter diffuses and arrives at different parts of HVC sequentially. In this case, the microcircuits of neurons responsible for their own syllables are located at different locations throughout the nucleus. The triggering neurotransmitter is released from the A11 axons all at once and then diffuses within HVC, activating spatial organized microcircuits to sing each syllable sequentially.

3.5 Acknowledgements

We appreciate Dr. Arij Daou and Prof. Richard Mooney for enlightening explanations and perspectives in terms of biology and experiments. Thanks also to Prof. Nigel Goldenfeld and Prof. Elena Koslover for valuable guidance on model improvement, presentation, and writing.

Chapter 3, in full, is currently being prepared for submission for publication of the material by P. Xia and H. D. I. Abarbanel. The dissertation author is the primary author of this paper.

Chapter 4

Conclusion

This dissertation describes approaches to understand and model neurons in the HVC, a nucleus which enables zebra finches to sing. The neural circuits of the song system have always been an interesting topic in neuroscience since it is a stepping stone to further study of human speech and vocal learning. Songbirds are a highly diverse group, and the song learning and production process has only been studied in a small fraction of them, including zebra finches [16]. The song system of zebra finches is an appealing and relatively simple model since the male adults sing highly precise and invariant songs as directed towards females [28]. In the song system, HVC plays a key role of coding for syllable order and controlling the overall temporal structure of the song [36] [79]. To characterize the comprehensive dynamics of HVC neurons, we first employed a data assimilation method to parameterize and calibrate models for single HVC neuron in Chapter 2, and then coupled neurons together into a HVC microcircuit model to explain salient features and activities of this nucleus. In this chapter, we will briefly review the key points and conclusions in Chapter 2 and 3.

Chapter 2 used a data assimilation method to transfer information from the cross-membrane voltage to a dynamic model that described single neuron behavior in HVC from zebra finches. For the HVC neuron, we proposed several conductance-based neuron models from the simplest Hodgkin-Huxley model to a more complex one including the calcium current and the NaP current. The neuron model involved unmeasurable state variables (i.e. gating

variables) and unknown parameter values governing dynamics of the state variables, and we aimed to estimate all of them and then predict the future evolution of this dynamic system. To achieve this goal, we introduced the PAHMC method to locate the area around the path (i.e. the collection of all the state variables along with the time-independent parameters) of the highest probability. This method used HMC to sample in the path space with higher efficiency than the traditional Monte Carlo sampling, and used PA to enable a more precise search for the area near the global minimum [6]. Then, PAHMC was first applied to the basic NaKL neuron model in twin experiments, with a chaotic current as a driven force to this system and simulated voltage as the measured variable. As a result, we usually recovered the time evolutions of unknown state variables and values of time-independent parameters, and predicted future voltages outside the training window with those estimations. Next, the neuron model was expanded with CaT current and NaP current with more complex dynamics, and the twin experiments' estimations of gating variables, parameters and future voltages were quite close to their actual values, showing that PAHMC was capable of handling the transfer of information between HVC neuron voltages and models. Unfortunately, this data assimilation method did not discover a model describing the neuron dynamics correctly when it was applied to experimental recordings of HVC neurons' voltage. Possible causes for the failure could be incompleteness or incorrectness of proposed ion currents model or difficulty to locate global minimum across long distances in the path space.

Multiple neurons must coordinate together to make the HVC region function properly, so a comprehensive model describing neuron activities in the HVC should involve both single neuron dynamics and their interactions. In Chapter 3, we proposed a model of HVC neuron network in light of the physiological properties of individual neurons as well as their synaptical interactions established by electrical recordings. We began with single neuron models describing fundamental ion channels in the HVC_{RA} and HVC_{I} neurons, and showed that the HVC_{RA} neuron fired continuously under a background current above its experimental threshold. After introducing an inhibitory connection from the interneuron to the HVC_{RA} neuron, this HVC_{RA} neuron became silent, which was its expected behavior during quiet time of zebra finches. Then,

the trigger current from the A11 neuron group was introduced to the HVC microcircuit, and the interneuron model reproduced the continuous firing with intermittent silences behavior of real HVC_I neurons during song production. Now, the HVC_{RA} neuron was able to generate a burst, but the burst duration and spike quantity did not match experimental observations. This mismatch was resolved after the excitatory interaction from the HVC_{RA} neuron back to the interneuron was added to the circuit, which proved that the bidirectional connections in the HVC_{RA}-HVC_I neuron pair observed *in vitro* was necessary to maintain the firing pattern of neurons in this nucleus. Finally, we added more HVC_{RA} neurons in a chain and reproduced the time-locked sequential burst from multiple HVC_{RA} neurons during a syllable. All but one of the parameters in the single neuron models and synaptical current models were backed by other simulation or experimental papers. The only parameter that was fine-tuned was the maximal conductance of synaptic current between two HVC_{RA} neurons. In the end of this chapter, we discussed the possible range for the parameter and showed that the fine-tuned value sits within the measured range for maximal conductances for excitatory synaptical currents.

We have offered a biophysically based model of HVC neuron network and a pipeline to transfer intracellular recordings into a complete neuron model. The model could be further applied to describing the functions and dynamics of HVC neurons in other songbirds such as Bengalese Finch or canary. The fine-tuned parameters in the synaptic current model may also provide a reference for synaptic coupling strength in the avian brain. Our work in this dissertation offers tools to understand the dynamics of HVC and its functions in the song system, providing a basis for study of human neuron system for vocalization and speech.

Bibliography

[1] Thomas Trappenberg. Fundamentals of Computational Neuroscience. OUP Oxford, 2010.

[2] Dayan P.; Abbott, L. F. (2001). Theoretical neuroscience: computational and mathematical modeling of neural systems. Cambridge, Mass: MIT Press.

[3] Wulfram Gerstner et al. Theory and Simulation in Neuroscience. Science 338,60-65 (2012).

[4] L.F. Abbott. Theoretical Neuroscience Rising. Neuron, Volume 60, Issue 3, 2008.

[5] Nicola S. Clayton, Nathan J. Emery. Avian Models for Human Cognitive Neuroscience: A Proposal, Neuron, Volume 86, Issue 6. 2015

[6] Fang, Z. (2021). Methods for Inference and Prediction in Nonlinear Dynamical Systems. UC San Diego. Retrieved from https://escholarship.org/uc/item/8qw5w0bh

[7] Jingxin Ye (2016). Systematic Annealing Approach for Statistical Data Assimilation. UC San Diego.

[8] Henry D. I. Abarbanel. Predicting the future: completing models of observed complex systems. Understanding Complex Systems. Springer-Verlag New York, 2013.

[9] Zheng Fang, Adrian S. Wong, Kangbo Hao, Alexander J. A. Ty, and Henry D. I. Abarbanel. Precision annealing Monte Carlo methods for statistical data assimilation and machine learning. Phys. Rev. Research 2, 013050 – Published 15 January 2020.

[10] S. Duane, A. D. Kennedy, B. J. Pendleton, and D. Roweth, Hybrid Monte Carlo, Phys. Lett. B 195, 216 (1987).

[11] M. Betancourt, A conceptual introduction to Hamiltonian Monte Carlo, arXiv:1701.02434.

[12] Toth, Bryan Andrew. Computational Methods for Parameter Estimation in Nonlinear Models. 2011.

[13] G. Bard Ermentrout, David H. Terman. Mathematical Foundations of Neuroscience. July 2010

[14] Mooney, Richard Daniel (1991) The Development of Connectivity and the Nature of Synaptic Transmission between Avian Song Control Nuclei (Dissertation (Ph.D)), California Institute of Technology.

[15] Mooney R. Different subthreshold mechanisms underlie song selectivity in identified HVc neurons of the zebra finch. J Neurosci, 2000.

[16] Mooney R. Neural mechanisms for learned birdsong. Learn Mem. 2009 Oct 22;16(11):655-69.

[17] Richard Mooney. Birdsong. Current Biology 32, R1042–R1172, October 24, 2022.

[18] Nottebohm F, Stokes TM, Leonard CM. 1976. Central control of song in the canary, Serinus canarius.. J Comp Neurol.

[19] Nottebohm F, Kelley DB, Paton JA. 1982. Connections of vocal control nuclei in the canary telencephalon. J Comp Neurol.

[20] HODGKIN AL, HUXLEY AF. A quantitative description of membrane current and its application to conduction and excitation in nerve. J Physiol. 1952 Aug.

[21] Johnston Daniel and Samuel Miao-sin Wu. 1995. Foundations of Cellular Neurophysiology. Cambridge Mass: MIT Press.

[22] Owen P. Hamill, A. Marty, E. Neher, B. Sakmann, and Frederick J. Sigworth. Improved patch-clamp techniques for high-resolution current recording from cells and cell-free membrane patches. Pflugers Archiv, 1981.

[23] Wu N, Enomoto A, Tanaka S, Hsiao CF, Nykamp DQ, Izhikevich E, Chandler SH. Persistent sodium currents in mesencephalic v neurons participate in burst generation and control of membrane excitability. J Neurophysiol. 2005 May.

[24] S. Kirkpatrick et al. Optimization by Simulated Annealing.Science220, 671-680 (1983).

[25] Lorenz, Edward N., 1963: Deterministic Nonperiodic Flow. Journal of the Atmospheric Sciences, 20, 130-141.

[26] Barry Saltzman. Finite amplitude free convection as an initial value problem I. Journal of the Atmospheric Sciences, 1962.

[27] Henry D. I. Abarbanel. Analysis of observed chaotic data. Institute for Nonlinear Science. Springer-Verlag New York, 1996.

[28] Daou, A., Margoliash, D. Intrinsic neuronal properties represent song and error in zebra finch vocal learning. Nat Commun 11, 952 (2020).

[41] Bolhuis JJ, Okanoya K, Scharff C. Twitter evolution: converging mechanisms in birdsong and human speech. Nat Rev Neurosci 11: 747–759, 2010.

[29] Clayton, N. S. and Prove, E. (1989). Song discrimination in female zebra finches and Bengalese finches. Animal Behaviour, 38(2), 352–354.

[30] Sakata, J. T. and Brainard, M. S. Real-time contributions of auditory feedback to avian vocal motor control. J. Neurosci. 26, 9619–9628 (2006).

[31] Dezhe Z. Jin, Fethi M. Ramazanoğlu, H. Sebastian Seung. Intrinsic bursting enhances the robustness of a neural network model of sequence generation by avian brain area HVC. J Comput Neurosci (2007).

[32] Li M, Greenside H. Stable propagation of a burst through a one-dimensional homogeneous excitatory chain model of songbird nucleus HVC. Phys Rev E Stat Nonlin Soft Matter Phys 74: 011918, 2006.

[33] Fee MS, Goldberg JH. A hypothesis for basal ganglia-dependent reinforcement learning in the songbird. Neuroscience 198: 152–170, 2011.

[34] Nottebohm, Fernando, Arnold, Arthur P. Sexual Dimorphism in Vocal Control Areas of the Songbird Brain. 1976 Science.

[35] Nicolas Fourcaud-Trocmé, David Hansel, Carl van Vreeswijk, Nicolas Brunel. How Spike Generation Mechanisms Determine the Neuronal Response to Fluctuating Inputs. Journal of Neuroscience 17 December 2003, 23 (37) 11628-11640

[36] Daou A, Ross MT, Johnson F, Hyson RL, Bertram R. Electrophysiological characterization and computational models of HVC neurons in the zebra finch. J Neurophysiol. 2013.

[37] Kadakia N, Armstrong E, Breen D, Morone U, Daou A, Margoliash D, Abarbanel HD. Nonlinear statistical data assimilation for HVC-RA neurons in the avian song system. Biol Cybern. 2016 Dec.

[38] Meliza, C.D., Kostuk, M., Huang, H. et al. Estimating parameters and predicting membrane voltages with conductance-based neuron models. Biol Cybern 108, 495–516 (2014).

[39] D Margoliash. Acoustic parameters underlying the responses of song-specific neurons in the white-crowned sparrow. Journal of Neuroscience 1 May 1983, 3 (5) 1039-1057.

[40] Margoliash D, Fortune ES. Temporal and harmonic combination-sensitive neurons in the zebra finch's HVC. J Neurosci 12:4309–4326 (1992).

[41] Bolhuis JJ, Okanoya K, Scharff C. Twitter evolution: converging mechanisms in birdsong and human speech. Nat Rev Neurosci 11: 747–759, 2010.

[42] Coleman MJ, Mooney R. Synaptic transformations underlying highly selective auditory representations of learned birdsong. J Neurosci 24:9251–9265 (2004).

[43] Fortune ES, Margoliash D. Parallel pathways and convergence onto HVC and adjacent neostriatum of adult zebra finches (Taeniopygia guttata). J Comp Neurol 360:413– 441 (1995).

[44] Nixdorf BE. Ultrastructural analysis of the development and maturation of synapses and subsynaptic structures in the ectostriatum of the zebra finch. J Comp Neurol 290:472– 486 (1989).

[45] Perkel DH, Gerstein GL, Moore GP. Neuronal spike trains and stochastic point processes. I. The single spike train. Biophys J 7:391– 418 (1967).

[46] Richard Mooney, Jonathan F. Prather. The HVC Microcircuit: The Synaptic Basis for Interactions between Song Motor and Vocal Plasticity Pathways. Journal of Neuroscience 23 February 2005, 25 (8) 1952-1964.

[47] Margoliash D. Sleep, learning, birdsong. ILAR J 51: 378–386, 2010.

[48] Kornfeld J, Benezra SE, Narayanan RT, Svara F, Egger R, Oberlaender M, Denk W, Long MA. EM connectomics reveals axonal target variation in a sequence-generating network. Elife. 2017 Mar 27.

[49] Daniel Breen, Sasha Shirman, Eve Armstrong, Nirag Kadakia, Henry Abarbanel. HVC-I Neuron Properties from Statistical Data Assimilation. arXiv:1608.04433 [q-bio.NC]

[50] Long MA, Jin DZ, Fee MS. Support for a synaptic chain model of neuronal sequence generation. Nature 468: 394–399, 2010.

[51] Gibb L, Gentner TQ, Abarbanel HD. Brain stem feedback in a computational model of birdsong sequencing. J Neurophysiol 102: 1763–1778, 2009.

[52] Börgers C, Kopell N. Effects of noisy drive on rhythms in networks of excitatory and inhibitory neurons. Neural Comput. 2005 Mar;17(3):557-608.

[53] Armstrong E, Abarbanel HD. Model of the songbird nucleus HVC as a network of central pattern generators. J Neurophysiol. 2016 Nov 1;116(5):2405-2419.

[54] Mor Ben-Tov, Fabiola Duarte, Richard Mooney. A neural hub for holistic courtship displays. Current Biology. 2023.

[55] Destexhe, A., Mainen, Z.F., Sejnowski, T.J. Synthesis of models for excitable membranes, synaptic transmission and neuromodulation using a common kinetic formalism. J Comput Neurosci 1, 195–230 (1994).

[56] Destexhe A, Sejnowski TJ. Thalamocortical Assemblies: How Ion Channels, Single Neurons and Large-Scale Networks Organize Sleep Oscillations. Oxford, UK: Oxford Univ. Press, 2001.

[57] Hahnloser, R., Kozhevnikov, A. and Fee, M. An ultra-sparse code underlies the generation of neural sequences in a songbird. Nature 419, 65–70. 2002.

[58] Mohebi, A., Pettibone, J.R., Hamid, A.A., Wong, J.-M.T., Vinson, L.T., Patriarchi, T., Tian, L., Kennedy, R.T., and Berke, J.D. Dissociable dopamine dynamics for learning and motivation. Nature 570, 65–70 (2019).

[59] da Silva, J.A., Tecuapetla, F., Paixa˜ o, V., and Costa, R.M. Dopamine neuron activity before action initiation gates and invigorates future movements. Nature 554, 244–248 (2018).

[60] Riters, L.V., and Alger, S.J. Neuroanatomical evidence for indirect connections between the medial preoptic nucleus and the song control system: possible neural substrates for sexually motivated song. Cell Tissue Res. 316, 35–44 (2004).

[61] Kosche G, Vallentin D, Long MA. Interplay of inhibition and excitation shapes a premotor neural sequence. J Neurosci 35: 1217–1227, 2015.

[62] Sterratt D, Graham B, Gillies A, Willshaw D. (2011) Principles of computational modeling in neuroscience. Cambridge University Press, Cambridge.

[63] Daniel Johnston , Samuel Miao-Sin Wu. Foundations of Cellular Neurophysiology. 1996. The MIT Press.

[64] Toth, B.A., Kostuk, M., Meliza, C.D. et al. Dynamical estimation of neuron and network properties I: variational methods. Biol Cybern 105, 217–237 (2011).

[65] Bradley M. Colquitt and Devin P. Merullo and Genevieve Konopka and Todd F. Roberts and Michael S. Brainard. Cellular transcriptomics reveals evolutionary identities of songbird vocal circuits. Science, 2021.

[66] Storace, D., Braubach, O., Jin, L. et al. Monitoring Brain Activity with Protein Voltage and Calcium Sensors. Sci Rep 5, 10212 (2015).

[67] John D. Clements et al., The Time Course of Glutamate in the Synaptic Cleft.Science258,1498-1501 (1992).

[68] De Koninck Y, Mody I. Noise analysis of miniature IPSCs in adult rat brain slices: properties and modulation of synaptic GABAA receptor channels. J Neurophysiol. 1994 Apr;71(4):1318-35.

[69] Kozhevnikov AA, Fee MS. Singing-related activity of identified HVC neurons in the zebra finch. J Neurophysiol 97: 4271–4283, 2007.

[70] Ropert N, Miles R, Korn H. Characteristics of miniature inhibitory postsynaptic currents in CA1 pyramidal neurones of rat hippocampus. J Physiol. 1990 Sep;428:707-22.

[71] Stricker, C, Field, A C, Redman, S J, (1996), Statistical analysis of amplitude fluctuations in EPSCs evoked in rat CA1 pyramidal neurones in vitro. The Journal of Physiology, 490

[72] E. C. Burgard and J. J. Hablitz. NMDA receptor-mediated components of miniature excitatory synaptic currents in developing rat neocortex. Journal of Neurophysiology 1993.

[73] C. McBain and R. Dingledine. Dual-component miniature excitatory synaptic currents in rat hippocampal CA3 pyramidal neurons. Journal of Neurophysiology 1992.

[74] Naoki Hiratani and Tomoki Fukai. Redundancy in synaptic connections enables neurons to learn optimally. Proceedings of the National Academy of Sciences 2018.

[75] Woolley, S.M., Hauber, M.E. and Theunissen, F.E. Developmental experience alters information coding in auditory midbrain and forebrain neurons. Dev. Neurobiol. 70, 235–252 (2010).

[76] Christopher M. Glaze, Todd W. Troyer. Temporal Structure in Zebra Finch Song: Implications for Motor Coding. Journal of Neuroscience 18 January 2006.

[77] Alexay A. Kozhevnikov. Michale S. Fee. Singing-Related Activity of Identified HVC Neurons in the Zebra Finch. Journal of Neurophysiology. 2007.

[78] Simpson HB, Vicario DS. Brain pathways for learned and unlearned vocalizations differ in zebra finches. J Neurosci. 1990 May.

[79] Leonardo, A. and Konishi, M. Decrystallization of adult birdsong by perturbation of auditory feedback. Nature 399, 466–470 (1999).